A step towards molecular electronics:
the ferrocene molecule
on a metal-semiconductor system

Von der Fakultät für Mathematik und Physik

der Gottfried Wilhelm Leibniz Universität Hannover

zur Erlangung des Grades

DOKTOR DER NATURWISSENSCHAFTEN

Dr. rer. nat.

genehmigte Dissertation

von

Dipl.-Phys. Jędrzej Piotr Schmeidel

geboren am 17.08.1981 in Poznań, Polen

2012

Referent: Prof. Dr. H. Pfnür
Korreferent: Prof. Dr. W. Daum
Tag der Promotion: 14.05.2012

A step towards molecular electronics: the ferrocene molecule on a metal-semiconductor system

Gottfried Wilhelm Leibniz University of Hannover

Faculty of Mathematics and Physics

Solid State Physics department

Atomic and Molecular Structures division

thesis by

Dipl.-Phys. Jędrzej Piotr Schmeidel

2012

Abstract

In the first part, the domain walls on Ag $\sqrt{3} \times \sqrt{3}$ are investigated and structural and electronic model are introduced and discussed. Furthermore, the temperature dependence is investigated, showing the Peierls-type transition along the domain wall chain.

In the second part, the high resolution STM data of the local adsorption geometry of FDT on Ag $\sqrt{3} \times \sqrt{3}$ are presented. The comparison of theoretical results obtained for the molecule, on Ag(111) and Ag $\sqrt{3} \times \sqrt{3}$ surfaces, with STM measurement at RT, support the chemisorption with thiolate bonds to the Ag trimers on the HCT surface. The molecule is aligned with the Cp–Fe-Cp axis parallel to the surface, while the rotational freedom of the molecule is limited due to chemisorption. The presented adsorption model is supported by experiment and simulation.

In the third part, the perfect Ag $\sqrt{3} \times \sqrt{3}$ is prepared and investigated by means of STM, focusing on structural and electronic characteristics. The different reconstructions and amounts of Ag on Si are investigated; the submonolayer amounts, Ag $\sqrt{3} \times \sqrt{3}$ wetting layers, perfect epitaxial layers and multilayer systems. The influence of wetting layer on electronic character of deposited Ag nanostructures is studied. The occurrence of effective single and double barriers in tunnelling microscopy and spectroscopy for the Ag $\sqrt{3} \times \sqrt{3}$ system is investigated in the monolayer regime by varying the measurement and preparation conditions. The Coulomb Blockade oscillations are found for granular multilayer Ag films, whereas similar structures with existence of Ag $\sqrt{3} \times \sqrt{3}$ show only a single barrier characteristic. The vertical transport properties in this metal/semiconductor system depend on the structure and bonding on the atomic scale and on the lateral two-dimensional properties of the interface.

Keywords:

scanning tunneling microscope (STM), metal-semiconductor systems, molecular electronics

Zusammenfassung

Im ersten Teil, werden die Domänen-Wände auf Ag $\sqrt{3} \times \sqrt{3}$ untersucht und ein strukturelles und elektronisches Modell vorgestellt und diskutiert. Darüber hinaus wird die Temperaturabhängigkeit untersucht und es weist der Peierls-Typ-Übergang von den Domänen-Wand-Ketten auf.

Im zweiten Teil, werden die hochauflösenden STM-Daten der lokalen Adsorptionsgeometrie von FDT auf Ag $\sqrt{3} \times \sqrt{3}$ vorgestellt. Die theoretische Ergebnisse des Moleküls auf Ag(111) und Ag $\sqrt{3} \times \sqrt{3}$ Oberflächen werden mit STM-Messung bei RT vergliechen und unterstützen das Thiolat-Bindung-Chemisorption zu den Ag-Trimere auf der HCT Oberfläche. Das Molekül ist mit der Cp-Fe-Cp-Achse parallel zur Oberfläche ausgerichtet und die Rotationsfreiheit des Moleküls ist durch Chemisorption begrenzt. Das vorgestellte Adsorptions-Modell wird durch das Experiment und Simulation unterstützt.

Im dritten Teil, die perfekte Ag $\sqrt{3} \times \sqrt{3}$ ist vorbereitet und mittels STM mit Schwerpunkt auf strukturellen und elektronischen Eigenschaften untersucht. Die verschiedenen Rekonstruktionen und Mengen von Ag auf Si werden untersucht: Submonolagen-Schichten, Ag $\sqrt{3} \times \sqrt{3}$ Benetzung-Schichten, perfekte Epitaxieschichten und Multilayer-Systemen. Der Einfluss der Benetzung-Schicht wird auf elektronischen Charakter der abgeschiedenen Ag-Nanostrukturen untersucht. Die Einzel- und Doppel-Barrieren in Tunnel-Mikroskopie und -Spektroskopie werden durch der Variation der Mess- und Herstellungsbedingungen untersucht. Die körnige Multilayer Ag-Filme weisen die Coulomb-Blockade-Oszillationen auf, während das System mit der Ag $\sqrt{3} \times \sqrt{3}$ Benetzung-Schicht zeigt nur eine Einzel-Barriere. In diesem Metall/Halbleiter-System hängen die vertikale Transport Eigenschaften von der Struktur und Bindung auf atomarer Skala und von den Grenzschicht-Charakteristiken ab.

Schlagworte:

RasterTunnelMikroskop (RTM), Metall-Halbleiter Systeme, Molekulare Elektronik

Contents

Acronyms

STM Scanning Tunneling Microscope

STS Scanning Tunnelling Spectroscopy

CITS Current Imaging Tunnelling Spectroscopy

SPM Scanning Probe Microscope

AFM Atomic Force Microscope

LEED Low Energy Electron Diffraction

ARPES Angle Resolved Photo Emission Spectroscopy

UPS Ultraviolet Photoelectron Spectroscopy

IPES Inverse Photoelectron Spectroscopy

EELS Electron Energy Loss Spectroscopy

DOS Density of states

LDOS Local Density of states

HCT honeycomb-chained trimer,honeycomb-chained triangle

IET inequivalent triangle

DAS Dimer-Adatom-Stacking fault

FDT Ferrocene-1,1'-dithiol,FerroceneDiThiol

RT room temperature,ambient temperature

LT low temperature

ML monolayer

CB Coulomb Blockade

QWS Quantum Well State

SB Schottky Barrier

LN2 liquid nitrogen

LHe liquid helium

fcc face-centered cubic,cubic close packed

hcp hexagonal close-packed

UHV Ultra High Vacuum

RGA Residual Gas Analyser,Quadrupole mass spectrometer

MCBJ Mechanically Controllable Break Junction

HOMO Highest Occupied Molecular Orbital

LUMO Lowest Unoccupied Molecular Orbital

FFT Fast Fourier Transform

CHAPTER 1

Introduction

In today's world the information is one of the most valuable goods. It's economic, political and cultural significance cannot be negated, the humanity entered a new phase defined as "information society". Information is ought to be fast, cheap, easy to obtain and to create by anyone. The cost of 1 MB of digital data storage changed from 200$ in 80', through 5$ in 90', 0.02$ in 2000, down to 0.00005$ in 2010. A similar trend is visible for Internet accessibility. The 1 MBit connection per month costed 250€ in 2000, whereas in 2010 it was around 5€. Although the most important aims have already been achieved, the revolution brought by IT-Technology in the last few decades could not have been foreseen and despite many predictions the future may bring much more.

It is important to mention, that for the state of knowledge the limitations of currently used technology are already known, as an example, the superparamagnetic limit for the data storage. Therefore, as will be explained later, the molecular electronics is the ultimate realisation of miniaturisation in electronic applications.

This all was only possible by the numerous inventions created in last century. Computers and other electronic devices have become a basic tool for the "information society". Tools for working with the various information undergo constant simplification and become smarter, thus helping with data processing (databases), decision making (assisted decision systems), etc. At the base of all progress in area of software, great technological developments are made, as the demand for faster hardware grows.

Advances in miniaturisation led to great increase of computing power, for example today usual middle-line computer achieve 10-20 GFLOPS (Giga Floating point Operations per Second) which is comparable with supercomputers in 1990. Taking into account the expectations from the technological achievements, next to the computing

power, comes mobility, so that the limiting of power consumption is the second main aim. Modern mobile phone, achieves 25 MFLOPS, just the same as standard computer in 1995 or a supercomputer in 1970, whereas it is important and easy to notice that the "performance per watt" index is significantly different.

The first commercial computer, UNIVAC, performed ∼2000 operations per second consuming ∼125 kW power, while nowadays supercomputers achieve more than 1 GFLOPS consuming only one watt [Gre10] [GLa]. Significance of "green computing" is not only visible in area of scientific applications, as the need for mobility forces the market available battery powered devices to be energy efficient.

Apart from the significant impact of new technologies on the society, behind each market available application there are significant scientific inventions. Together with first applications, people start to predict and to plan the development pathway of micro-technology.

1.1 Micro/Nano-electronics

In 1965 Gordon E. Moore, the co-founder of Intel company, published an overview article in "Electronics" Magazine [Moo65]. Main concern of this article is the future of microelectronics. It points out existing and expected problems and possible solutions, thus it may be taken as the first "roadmap" for investigations in this area. This paper gave a base for the so called "Moore's law", which is a statement that the number of transistors will double around every 2 years. According to the microelectronic achievements at that time, Moore expected this rule to last for at least 10 years, but still, after small correction of the doubling time from 24 to 18 months, the rule remains valid since today. The last International Technology Roadmap for Semiconductors (2009) discusses widely lithographic problems concerning lithographic process of creating 22 nm gate length [ITR09].

The use of light in relatively simple photo-lithography processes allows to go from wide connection paths in printed circuit boards down to 32 nanometer process size in market available devices (2011). Miniaturisation of microelectronics was successful by simple means since three decades, but the standard methods of optical lithography, which depend on light wavelength, reach their limits. Unfortunately already for some time, the simple approach to down-size the masks is not working and special problems are to be solved, but even though the end of photo-lithography era was
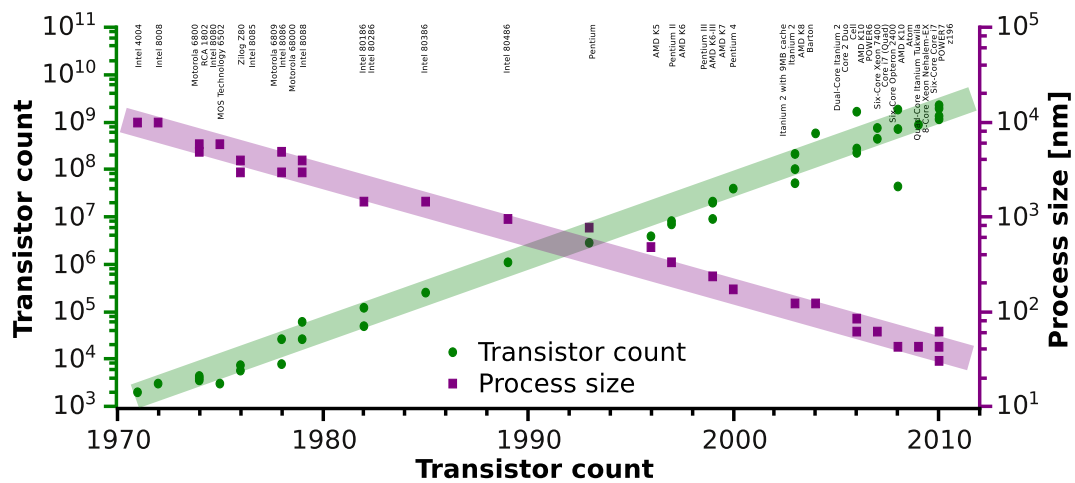
Figure 1.1: Graph represents the increase of transistors count in processors and the process size (Gate length) [Wik11].

already predicted a few times, slight corrections and minor inventions allowed to use the same idea and create smaller structures.

Frequency of light used for lithography shifts to higher frequencies in order to move the light wavelength limit and achieve better resolution. Today, wavelengths used in industry go from 193 nm down to 157 nm (Deep-Ultra-Violet). The way towards higher light frequencies (for example XDUV - eXtreme Deep Ultra Violet light) seems to have an end at X-Rays. Not only the creation of appropriate short wavelength light source for lithography [KWTT07], but also stable and reliable optics for high energetic radiation is a complex scientific challenge [LDE+11].

1.2 From Top-Down to Bottom-Up

Depending on the dimension of the structure, characteristic changes in electronic structure and density of states DOS are expected as shown in Figure 1.2. As mentioned above, the top down approach is limited to fabricate structures of a few nanometer. Therefore, quantum size effects, which occur only if the Fermi wavelength λ_f becomes comparable with the dimension of the structure itself, can be implemented lithographically only on the basis of low doped semiconductors. For metals with subnanometer Fermi wavelength, such effects are not accessible using lithographic processes.

Investigation of these effects and deep understanding of quantum physics allows on one hand aimed suppressing of unwanted effects in some areas, but on the
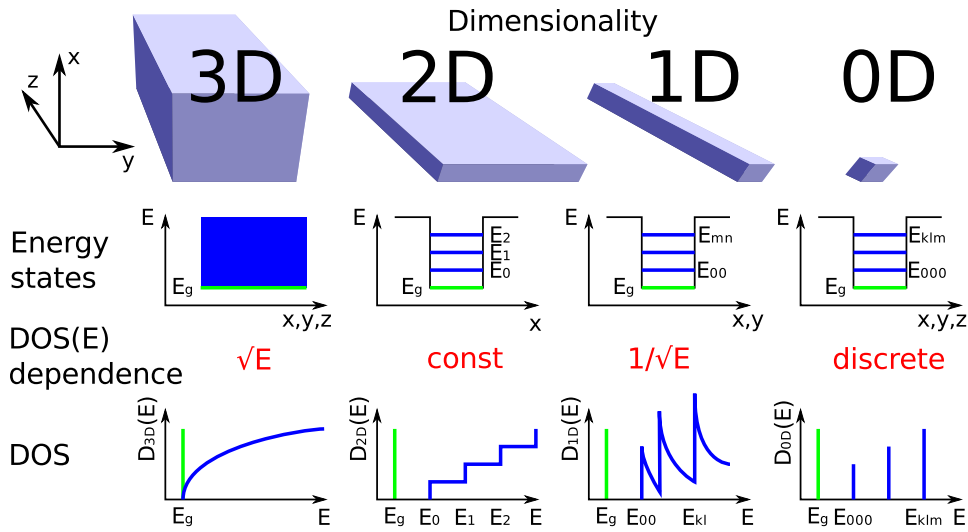
Figure 1.2: The picture shows comparison of 3D, 2D, 1D and 0D systems, where the characteristics of each system are presented in separate columns. From left to right, the 3D system is not restricted, 2D is restricted in x, 1D is restricted in x,y and 0D is restricted in all directions. The quantum confinement apply, when the size of system is smaller than the Fermi wavelength λ_f. The allowed energy states undergo quantisation, due to dimensional restriction by a potential well of width smaller than Fermi wavelength λ_f.

other hand, gives the possibility to explicitly exploit quantum character. This led to invention of new strategy, so called "bottom-up" approach, which is gaining importance since middle 90's. As mentioned before, the top-down approach tries to follow the known path, while the bottom-up approach, on the contrary, tries to investigate the system thoroughly on the microscopic scale and use this basic-research knowledge to build larger systems with defined form and characteristics by nano- and quantum-engineering. Therefore, the focus is placed on the smallest possible building blocks, that are, atoms, and directly following - molecules. Particularly molecules can be engineered, i.e. functionalised, to behave in a special manner, both electronically and chemically. Using the chemically and electronically functionalised molecules for electronics is called moltronics (molecular electronics) and will be explained in details further. In the opposite to the previously described miniaturisation approach, the assumption of existence the quantum nature lies at the base of moltronics. Therefore for moltronics, the quantum physics is not an improvement, but is a requirement.

1.3 Molecular electronics

The investigations in the area of molecular electronics gained a lot interest since 80', whereas for a long time stayed mostly as scientific inventions and first at the beginning of 2000 first market applications started to appear. Even though a direct substitution of top-down approach with bottom-up ones nowadays is limited, scientific achievements are promising and first applications are found in other areas. One of the fist examples of molecular electronics are molecular films, which can be used for instance as display material revealing the potential of low energy consumption. Therefore, first the use of organic molecular films will be introduced. Thereafter, the essential concept of molecular electronics using single molecules will be explained.

Power consumption, price, scalability and robustness of organic light emitting diodes OLED seems to have changed the way of looking on this new approach to miniaturisation. The lithographically prepared light emitting diode is substituted by a specially synthesised molecules. An electroluminescent is a thin film of organic molecules which emit light due to current flow. OLED applications still have significant improvement potential, therefore are expected to surpass the LCD screens in means of image quality, power consumption and price in the next few years.

Electroluminescence in organic materials was investigated since 50' [Ber55]. In first experiments concerning emission of light from molecules, among others, acridine orange, tetracene and anthracene were used. However, first significant advances towards application were made around 1990 [TV87] [BBB+90], where 100 nm thick films of polyphenylene vinylene (PPV) were used. The simplified comparison of construction schema and electronic energy diagram of LED and OLED device can be seen in Figure 1.3.

Generally, the success of molecular based devices in displays raises the question, if the application of such devices is limited just to this area. Apart from investigations of light emission, the first step towards molecular based electronics was made by Aviram and Ratner in 1974. In their paper, they proposed a model (see Figure 1.4) of molecule working as a molecular rectifier [AR74], which could substitute the rectifying diodes at the nano-scale. Here, the designed model molecule, with its defined electronic characteristics and having a precisely assigned function, is perfect example of the bottom-up approach. Every part of the molecule is engineered for a special purpose.

The molecule, which electronic structure is visible in Figure 1.4, consists of a donor
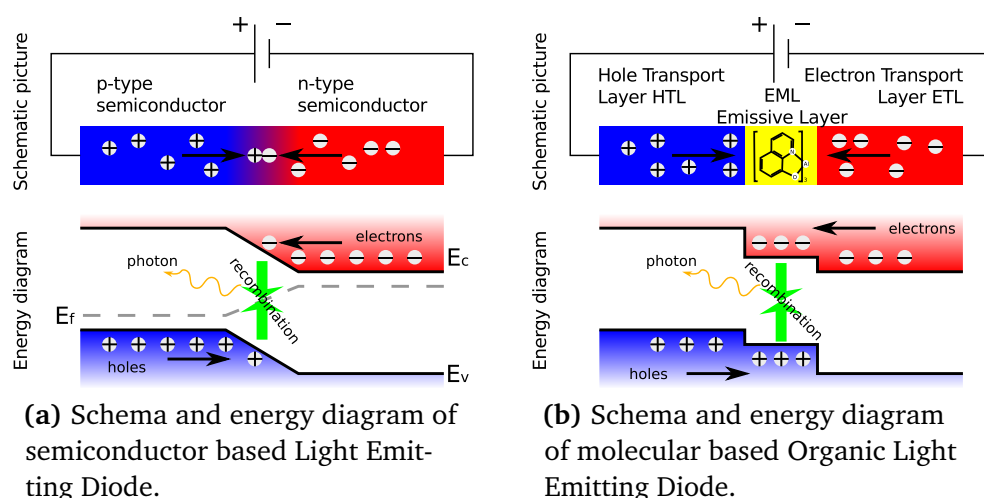
(a) Schema and energy diagram of semiconductor based Light Emitting Diode.

(b) Schema and energy diagram of molecular based Organic Light Emitting Diode.

Figure 1.3: Comparison of schematic construction and electronic energy diagram of LED and OLED device. These two passive elements are very similar. The semiconductor based diode consists of two differently doped semiconductors and, spontaneously formed between them, junction. The molecular based diode consists of two molecular layers, so called Hole Transport Layer (HTL) and Electron Transport Layer (ETL) and an Emissive Layer (EML) between them. The HTL and ETL act as p-doped and n-doped semiconductor, respectively. In OLEDs the emissive layer is not created spontaneously but it is an additional molecular layer.
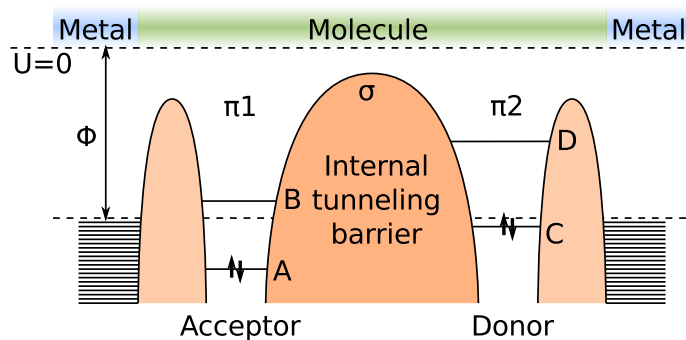

Figure 1.4: Electronic landscape model of functionalised molecule working as a molecular rectifier by Aviram and Ratner [AR74]. For explanation, see text.

π-system and an acceptor π-system, separated by a σ-bond tunnelling barrier. Thus, such a donor-acceptor system is similar to a p-n rectifying diode. The pi-bonds, have its well defined molecular orbital states, while the sigma-bond is a required for separation of orbitals. **A** is the highest occupied level of acceptor (HOMO),**C** of the donor (HOMO), whereas **B** is the affinity level of the acceptor (LUMO) and **D** of the donor (LUMO).

Charge transfer through tunnel barrier can occur via resonant tunnelling (onto equal energetic states) or inelastic processes.

In Figure 1.5a the applied positive (forward) bias ΔU_p leads to an energetic adjustment of the empty orbital **B** with the Fermi level of the left metallic contact and an adjustment of the occupied orbital **C** with the Fermi level of the right metallic contact. In this configuration resonant tunnelling from left contact to **B** and from **C** to right contact is possible. The charge from now occupied orbital **B** can tunnel inelastically to now empty orbital **C** and he current flow is limited only by the internal tunnelling in the molecule.
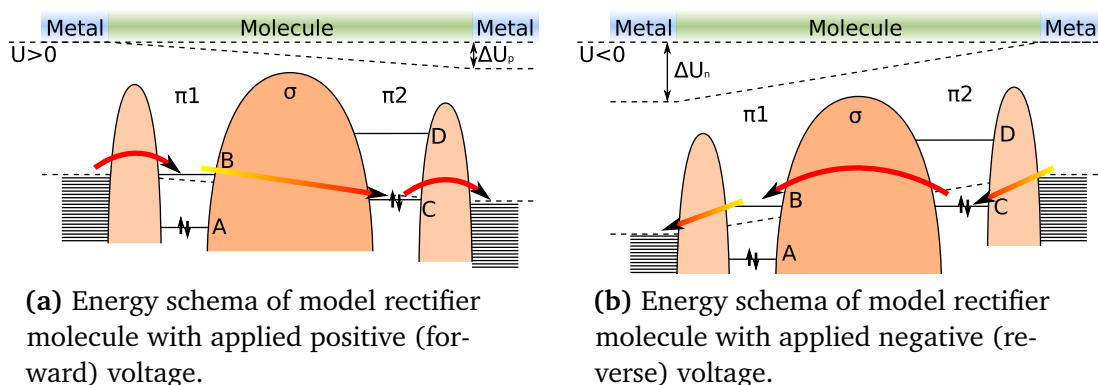

(a) Energy schema of model rectifier molecule with applied positive (forward) voltage.

(b) Energy schema of model rectifier molecule with applied negative (reverse) voltage.

Figure 1.5: Energy schema shows the model rectifier molecule with applied positive and negative bias voltage, accordingly. For explanation, see text.

The Figure 1.5a shows the opposite situation, where the negative (reverse) bias ΔU_n is applied to the molecule. Even though the orbital **B** is empty and orbital **C** is occupied, the charge transfer is firstly possible, when the **B** and **C** orbitals are adjusted and a tunnelling occurs. Hence, the internal tunnelling is a main limiting factor. Therefore, due to asymmetric donor-acceptor system, the applied voltage in reverse direction needs to be higher ($|\Delta U_n| > |\Delta U_p|$) in order for the current to flow.

As seen this model molecule has due its asymmetric electronic structure an rectifying behaviour with a diode-like I/V characteristics, as presented in Figure 1.6. Following this path, Aviram and Ratner proposed an example molecule [AR74], which consists of two π-systems separated by σ-system, which is presented in the Figure 1.7a. As required, one π-system is the acceptor Tetracyanoquinodimethane (TCNQ) molecule, whereas the other is the Tetrathiafulvalene (TTF) donor molecule. The triple Methylene bridge acts as the σ-bonded separator of π-systems.
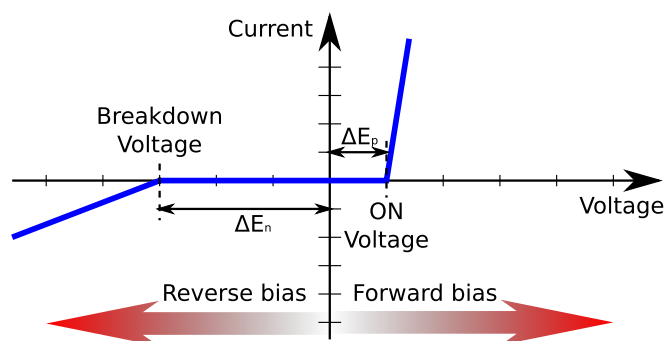
Figure 1.6: Schematic I/V characteristics of a model rectifier molecule.

(a) Chemical structure of the rectifier molecule. Acceptor pi-system is TCNQ molecule, donor pi-system is TTF molecule and triple Methylene bridge acts as sigma-bonded separator.

(b) Calculated I/V characteristics of rectifier molecule. Direct electrode to electrode tunnelling. Electron affinity of acceptor $= 5.0$ eV, ionisation potential of donor $= 5.3$ eV and $\phi = 5.1$ eV.
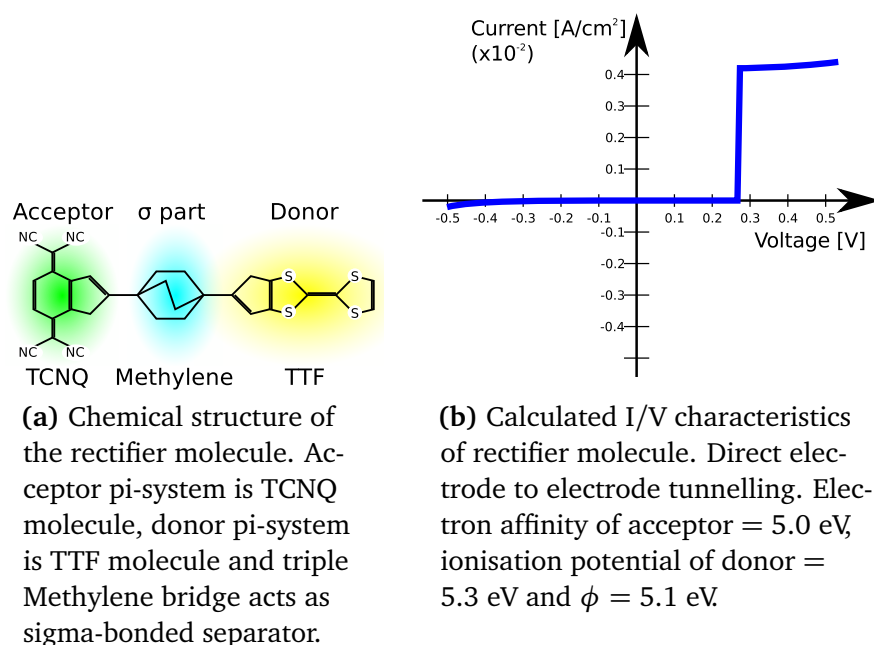
Figure 1.7: Real example of rectifier molecule presented by Aviram and Ratner [AR74].

After Aviram and Ratner, the Figure 1.7b shows the calculated I/V characteristics of presented in Figure 1.7a example molecule. This simplified calculation reveals indeed rectifying behaviour of this molecule (for detailed description of calculation, read [AR74]). The characteristics are similar to the known rectifying semiconductor diodes, that is, current flow in one direction (forward) is highly preferred over the other (reverse). Furthermore, in this example, the so called, breakdown voltage, is expected to occur around 0.55 V of applied reverse bias. However, an experimental realisation

took another 30 years [EOK+05]. By using mechanically controlled break junctions, Heiko Weber and coworker succeeded to measure the proposed diode characteristics.

It is important to mention, that for sake of simplicity, Aviram and Ratner neglected any influence due to chemical bonds. The idea in the form presented above is a purely modular concept. The attractiveness of this approach is that the later device can be synthesised chemically. However, also with respect to technically applicable structures, chemisorption of the molecule at (low dimensional) metallic structures is a decisive parameter.

In order to measure directly the molecular characteristics, that is, the transport through a single molecule, first STM was used [WR96] [MVR+96] [DTH+97]. This relatively complex measurement method gave first experimental results. Shortly after first investigations with STM, the new measurement system, so called MCBJ (mechanically controlled break junction) was introduced. Here a thin wire was pulled in order to break it in a controlled manner, leading to creation of a gap in nanometer range [RAP+96]. This method allowed to contact and measure different molecules with the same measurement system (among others, Reed et al. measured benzene-1,4-dithiol [RZM+97] and Reichert et al. measured oligo-phenylene-ethinylene [ROB+02]). A further method to fabricate nano-spaced contacts is electromigration. Here, through the lithographically created wire a current is passed. Due to extremely high local current densities ($10^7 - 10^8 A/cm^2$), the current induced material transport occurs. In order not to let the wire burn, the experiment is conducted in vacuum at low temperatures. This controlled experiment allows to create planar nano-gaps [PLA+99] [EF05] [GSP+06] [Sch06]. On the one hand the MCBJ allows to perform large number of measurements revealing good statistics, but on the other hand gives no possibility for a direct observation of the molecule in the gap. In contrary, the electromigration created contacts allow the access with STM due to its planar design, but a flexible adjustment of the gap is difficult to realise.

Summarising, clear advantages of molecular electronic, such as modular concept and exploiting of quantum nature of molecules further support this idea. Modularity gives not only the possibility of an ex-situ synthesis of modules in large amounts, but also characteristics of each module can be engineered by use of certain functional groups. Unfortunately, as first experiments show, this simple picture can be only used for weakly interacting systems, that is, for physisorbed molecules, which require a low temperatures environment. In order to apply this invention in the sense of Moore's law, chemisorption is required. Hence, the simple idea of modularity gains complexity, as

in this situation the strongly interacting system, the molecule and substrate, create an entity and both parts, i.e. molecule and contact, influence the character of the device. This finding is the main motivation of this work, which consists of investigation of the adsorption of molecules on metal substrate and influence of defects.

1.4 This work

After a brief theoretical introduction of the STM method the metal-semiconductor systems, which were used in this work, will be introduced. A detailed description and preparation procedure of each system will be shown.

The molecule will be presented in details in subsection 2.3.1. In this work ferrocenes were investigated and it was found that due its iron core it has higher conductivity than other carbon-based molecules [GEW+05]. Also the double π-system, separated by the iron atom, reveal a rotational flexibility in order to promote s stressless adsorption in between metallic contacts. As substrate the wetting layer structure of Ag on Si(111) is mainly used. This system is the prototype of an 2d nearly free electron gas and allows to study systematically the influence of the defects with in the layer and its electronic properties (acting as a contact) towards the adsorption of molecules.

The existence of perfect surfaces and perfect bonds is impossible in reality, therefore the most probable adsorption positions of molecules will be defects. In the first experimental part, therefore, investigations of surface defects will be presented. As mentioned section 3.1 I will focus mainly on the structural investigation of domain walls. The adsorption of ferrocenedithiol is presented in section 3.2.

The last experimental part presents an extended investigation of the electronic structure of microscopic nano-sized systems, such as thin layers, clusters and islands in section 3.3. By means of local spectroscopy the electronic properties of the wetting layer itself but also of the small clusters are probed.

CHAPTER 2

Basics

In this chapter the basics will be introduced. References from whole work will lead to this chapter, because the methods used are similar for all experiments.

2.1 Experimental devices

In this part used experimental devices will be described and explained. Furthermore, its theoretical background will be also introduced.

2.1.1 STM - Scanning Tunnelling Microscopy

The mostly used method in this work is the STM. It belongs together with, among others, the Atomic Force Microscope (AFM) to the Scanning Probe Microscopes (SPM). Generally, the scanning microscope technique is a measurement method, that does not generate the image in a single recording, but measure each point separately. This process is referred to as scanning, as each measurement point is recorded and assembled computationally into an image.

In an STM, the sharp metallic tip is kept in small distance above a conductive sample surface. The perfect tip should be made of single atom, however, in reality often several atoms contribute to the tunnelling current. When a voltage is applied between tip and sample, which are separated by small distance, a current flows, which depends exponentially on the distance. This current is called tunnelling current and the probe-sample separation in STM is usually in the range of ~ 1 nm. The achievable spatial resolution depends on the size of the tip probe.

The STM was developed in 1982 by Binnig and Rohrer. This development allowed for the first time to examine the sample surface down to atomic scale and thus to make atoms and molecules directly visible [BRGW82b], [BRGW82a]. A similar device was invented already in 1971 by Young and was called Topografiner [You71], [YWS72], however it did not achieved atomic resolution. In 1986 Binnig and Rohrer received the Nobel Prize in physics for their invention.

Schematically, the setup of a STMs is presented in Figure 2.1.
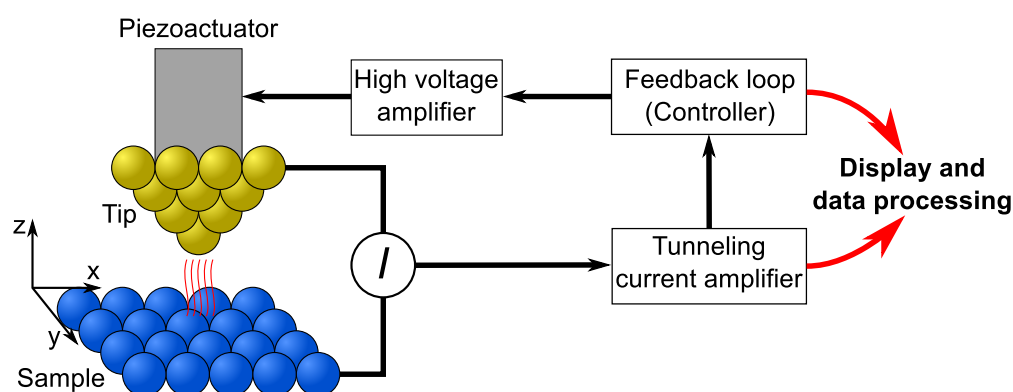
Figure 2.1: Schematic representation of the basic components of an STM.

The bias voltage is applied and the sample and probe are brought together to a very short separation distance of around 1 nm. If the voltage is applied at the small distances, the electrons can tunnel through the gap and an electric current can be measured. This current is called tunnelling current, which will be explained in detail later. Assuming an homogeneous sample material, the current is directly proportional to the tip-sample separation, thus allowing to control this distance. While moving the tip over the sample during the scanning, the differences in height will be detected as change in tunnelling current. As explained in the next section, the STM can be operated in two different scanning modes.

Summarising the introductional remarks, the functioning of STM depends on the flow of the tunnelling current. Both the tip and the sample must conduct current, i.e., need to be conductors or semiconductors. Disadvantage following from this requirement is that a large part of materials may be investigated only under vacuum conditions to avoid contamination, whereas insulators cannot be directly investigated at all.

In this work an Variable Temperature Scanning Tunnelling Microscope UHV 300

manufactured by RHK company in combination with RHK SPM 1000 control electronics was used. The sample was cooled by cold finger using either liquid helium (LHe) or liquid nitrogen (LN2). Possible measurement temperatures are RT (room temperature, no cooling), 120 K (liquid nitrogen LN2 cooling) and 40 K (liquid helium LHe cooling). Concerning technical aspects, such as Curie temperature of piezo actuators or thermal drift, high temperature applications issue the experimental challenge. The most commonly used materials for probes is tungsten or platinum-iridium. In this work only tungsten tips were used.

2.1.1.1 Measurement modes

The STM can be operated in two modes. The first and most widely used is the *constant-current mode*. The current during the measurement is kept constant with the help of a control feedback loop mechanism. In STM usually a proportional–integral (PI) controller is used in the feedback loop. Since the tunnel current depends exponentially on the distance between the tip and the sample (under assumption of a fixed bias and uniform surface), the height adjustment is recorded as shown in the Figure 2.2a. The correction is done by an application of appropriate voltage on piezoelectric actuator. In this mode, the distance between tip and sample is defined and represented by the current value, the so called setpoint. Furthermore, no absolute distance between tip and sample is considered, just the height variation between separate measurement points.
This method can be used in a reliable manner even on rough or inclined surfaces. However, this method is relatively slow due to use of the controller, compared to the constant-height mode (see 2.2).

In the second method, called *constant-height mode*, the feedback loop is switched off, so the height is kept constant and the current changes are recorded, as depicted in the Figure 2.2b. There is no need for controller in this mode, so the measurement can be performed much faster, however rough or tilted surfaces are very difficult to investigate, as the measurement range is limited by the setpoint distance of up to 2 nm.

All STM pictures in this work were obtained in the constant-current mode. In case of spectroscopic measurements, a detailed measurement explanation will be given.
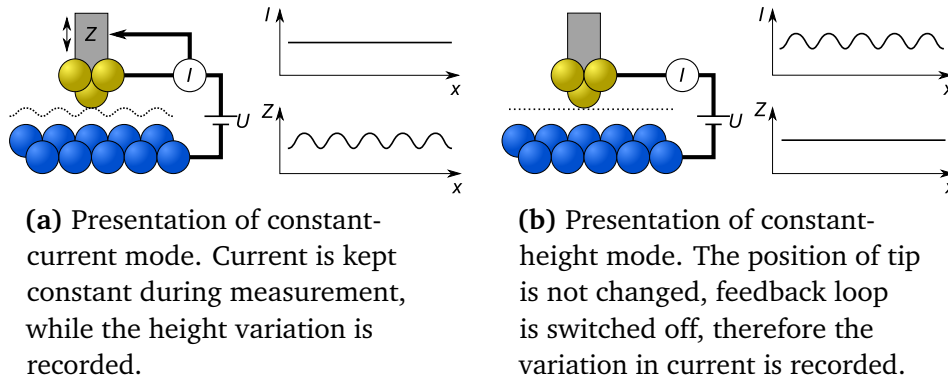
(a) Presentation of constant-current mode. Current is kept constant during measurement, while the height variation is recorded.

(b) Presentation of constant-height mode. The position of tip is not changed, feedback loop is switched off, therefore the variation in current is recorded.

Figure 2.2: Presentation of measurement modes used in STM. The mostly used mode is constant-current mode.

2.1.1.2 Tunnelling theory

Tunnelling is the phenomenon where a particle can go through a barrier, situation that can not be described by classical physics. Applying this quantum mechanical picture to STM, there is a nonzero probability that an electron can overcome the potential barrier without meeting the classical requirement for energy.
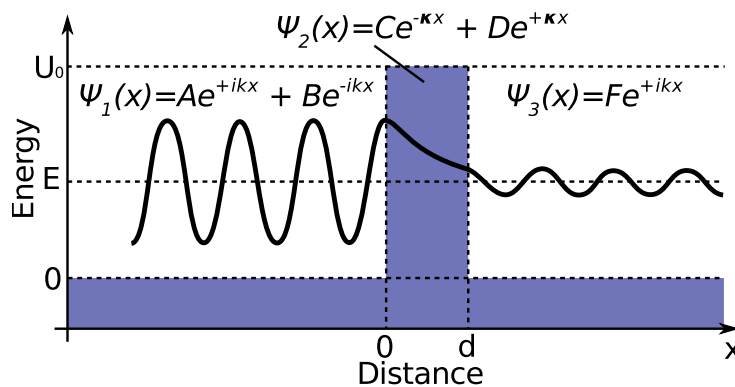
Figure 2.3: Tunnelling through a one-dimensional potential barrier of height U_0 and width d.

A graphical representation of this effect, called quantum tunnelling, is shown in Figure 2.3. The solutions of the Schrödinger equation for an incident electron approaching a rectangular barrier of height U_0 and width d, are following wave

functions:

$$\Psi_1(x) = Ae^{+ikx} + Be^{-ikx} \quad \text{for} \quad x < 0,$$

$$\Psi_2(x) = Ce^{-\kappa x} + De^{+\kappa x} \quad \text{for} \quad 0 < x < d,$$

$$\Psi_3(x) = Fe^{+ikx} \quad \text{for} \quad d < x.$$

The wave numbers k and κ are defined as follows:

$$k = \frac{\sqrt{2m_e E}}{\hbar}, \quad \kappa = \frac{\sqrt{2m_e(U_0 - E)}}{\hbar}.$$

For explanation of the amplitudes A-F, see Figure 2.3. The transmission probability for an electron with energy E, approaching from the left and appearing on the right side of the barrier, is given by:

$$T(E,d) \equiv \frac{|F|^2}{|A|^2} = |M|^2.$$

Applying this theory to the experimental setup, firstly, an external bias needs to be applied, secondly a multi-particle picture needs to be considered. STM measures the local density of states integrated over energy scale from E_f to the applied bias. The Figure 2.4 shows a potential diagram of the tunnelling effect through a single potential barrier, between two metals.
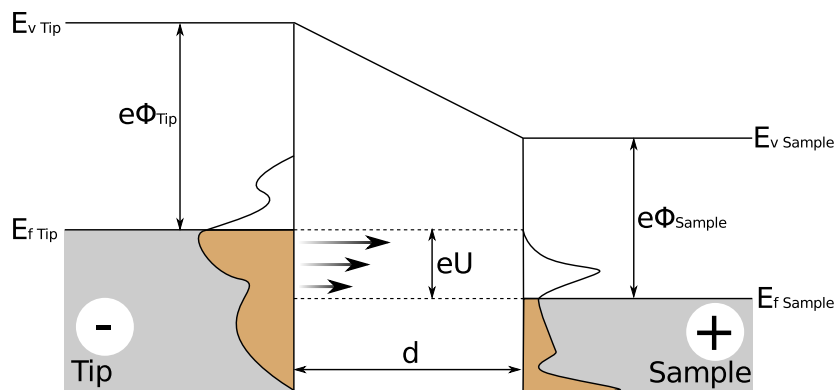

Figure 2.4: Potential diagram for tunnelling between tip and sample with an STM

Exemplarily, the tip is at a higher potential compared to the sample and electrons can tunnel from occupied of the tip into unoccupied states of the sample. Such setting

allows to measure the density of the conduction band states over the surface of the sample and to create corresponding empty-states image. The application of a negative voltage to the tip causes a shift of the electronic structure downwards, so that a flow of electrons from occupied states of the sample into unoccupied states of the tip occurs. The resulting image is called a filled-state image and is based on the density of states of the valence band. For simplicity it is assumed that the tip has high density of states, thus constant over whole energy range, when compared with the DOS of the sample.

2.1.1.3 STM theory

The simple tunnelling theory provides a good explanation and base for the qualitative understanding of STM. Bardeen investigated the tunnelling effect in 1961 and came to the conclusion that the setup can be treated as a weakly coupled system (eg. tip and sample) [Bar61].

The solution of this problem gives the wave functions, whereas the square of the overlap function, corresponds to the probability of electron transfer through the barrier. The basic tunnelling theory of Bardeen was further optimised by Tersoff and Hamann for STM. This approximation for small values of $k_B T$ ($T = 0$) led to the formula:

$$I = \frac{4\pi e}{\hbar} \int\limits_0^{-eU} \rho_{Sample} \left(E_{f,Sample} + eU + \epsilon \right) \rho_{Tip} \left(E_{f,Tip} + \epsilon \right) |M|^2 d\epsilon$$

Hence, the current is given by the convolution of the density of states of the tip ρ_{Tip} and the sample ρ_{Sample} and weighed by the tunnelling matrix element M, which represents the transmission for the electron with an fixed energy. In this case, the $\hbar$ is the Planck constant and eU the applied bias voltage. The eU denotes the applied bias voltage and $E_{f,Sample}$ and $E_{f,Tip}$ are the Fermi energies of sample and tip, respectively (see Figure 2.4).

Important for the development of the STM tunnel theory is the Tersoff-Hamann approximation [TH85]. This approach assumes the tip to be mono-atomic and point-shaped. With this assumption, the wave function ψ_ν of the tip can be approximated by a spherical potential and the transmission can be expressed by the following formula:

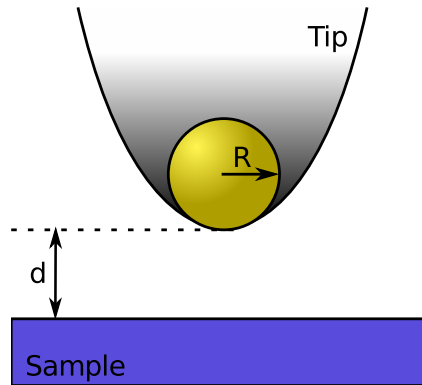$$T = \left| \psi_\nu \left(\vec{r}_0 \right) \right|^2 \propto e^{-2\kappa(R+d)}$$

Figure 2.5: Figure depicting the Tersoff-Hamann approximation. S-wave-tip model assumes, that the tip is mono-atomic, point-shaped. *R* is the radius of tip and *d* is distance from tip to sample.

The basic model is illustrated in Figure 2.5.

2.1.2 STS - Scanning Tunnelling Spectroscopy

Following the tunnelling theory, it is possible to extend the standard STM measurement technique, to obtain full local electronic information, such as the Local Density of States (LDOS), band gap, local capacitance, vibrational states, etc. The averaging spectroscopy methods (such as Ultraviolet photoelectron spectroscopy UPS, Inverse photoelectron spectroscopy IPES and Electron energy loss spectroscopy EELS) give the averaged electronic information over macroscopic areas, whereas with the STS one can obtain local information on the atomic scale.

As mentioned before, STM measures current which is the outcome of integration of DOS from 0 V to the applied voltage. As the form of the DOS and its underlying band structure is not simple, it is not possible to calculate back the DOS from single measurement.

As mentioned before, in the principle of the STM measurement method works by applying the voltage and probing the current. Furthermore, by variation of the voltage the *I/U* characteristics can be obtained. This can be shown by the formula for the current in dependence of DOS of the sample, which for low temperature can be written in the form [TH85] [GW06]:
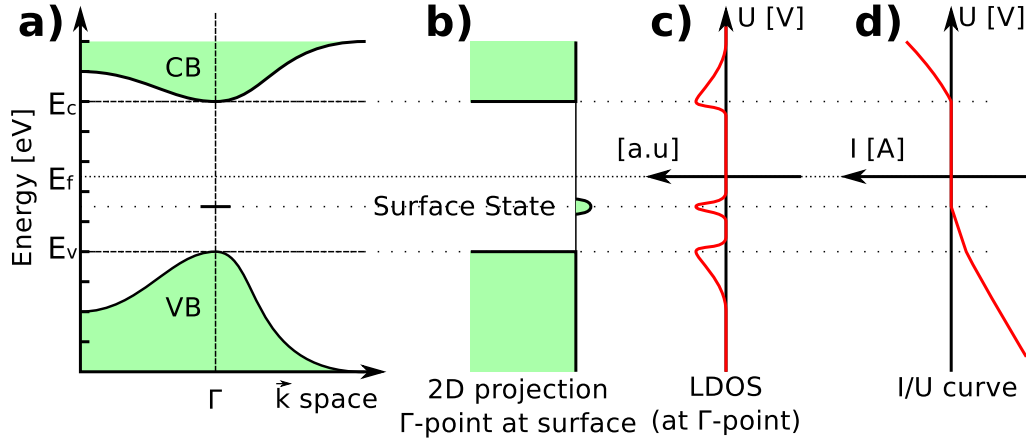
Figure 2.6: Simplified graphical explanation of the relationship between band structure and obtained by STM Current-Voltage (I/U) curve. By means of STM it is possible to measure the Current-Voltage curve and the LDOS. In the figure the example of a direct semiconductor is presented. See text for details.

$$I \propto \int_{0}^{-eU} \rho_{sample}(\epsilon)d\epsilon \quad \text{where} \quad \rho_{tip} = const \quad \text{and} \quad |M|^2 = const.$$

The assumption is that the STM tip has a constant DOS at the Fermi energy, since it is metallic. In order to obtain the DOS from the sample, the Current-Voltage characteristic is differentiated so that dI/dU relationship is obtained in the form:

$$dI/dU \propto \rho_{sample}(eU).$$

Furthermore, to exclude the voltage dependence, the curve is normalised and the final formula:

$$\frac{dI/dU}{I/U} \propto \text{DOS}(eU)$$

is the normalised DOS.

This relationship is shown graphically in Figure 2.6. In Figure a) an example of the band diagram of a direct semiconductor is presented. The valence band edge E_v, Fermi level E_f and the conduction band edge E_c are shown. In the band gap, a

surface state is visible. The Figure b) is a projection of the 3D band diagram onto 2D surface band diagram picture. According to the system geometry, the tunnelling current flows always directly between tip and the sample, perpendicular to the surface, therefore only small part of k-space around Γ is probed. Following this simplified path, in the Figure c) an LDOS characteristics of the surface around Γ point is shown, which by integration, gives the Current-Voltage curve, presented in Figure d). This simple explanation does not take into consideration more complex effects such as local capacitance, vibrational states, etc.

The simplest method of obtaining the LDOS is the measurement of the Current-Voltage (I/U, called also often I/V) curve, followed by a digital differentiation. In Figure 2.6 a simplistic picture shows the relationship between band structure, LDOS and Current-Voltage curve. Hence, it is important to notice, that by means of the STM measurement of the full band structure is not possible, but only the Projected Density of States and Current-Voltage curve can be obtained.

An extended spectroscopy method with the imaging abilities of STM is called Current Imaging Tunneling Spectroscopy (CITS). By obtaining a STS curve on each point of a measured area, an image with full spectroscopic information is obtained. Such information is useful while investigating the influence of structure on surrounding area. A large drawback of this method is measurement time, which for usual experiments can take few hours and for special applications even days.

The theoretically simple idea of STS, sets an experimental challenge. In the commonly used measurement method it is needed to disable the feedback loop. Therefore the tip stability (lack of drift and creep) is critical. In some cases disabled feedback loop can even lead to tip-crash, whereas without stabilised drift, the distance change during measurement may lead to erroneous data. Keeping this in mind, data repeatability in this situation is of much higher importance than in simple STM imaging, where the feedback loop always sets the tip distance appropriately. The second important part which is being discussed since invention of STM is the influence of the tip properties on the measurement. It is clear, that the assumption of a structurally perfect single point probe cannot be experimentally guaranteed and the preparation method of sharp tips is being optimised all the time. Therefore, the influence of finite-size tips has to be considered [KS86] [Ter90] [Kel91]. Nevertheless, also the electronic properties of the tip can have also large influence on the measurement. The simple Tersoff-Hamann approximation for the s-orbital shaped tip is also a subject of active discussion. For example, the molecular functionalisation of the tip can enhance reso-

lution and contrast of the STM picture [RMS+05] [SNMB11] [CDG+11], as well as aimed exploiting of different atomic orbitals [CNS+10]. Assumption of constant DOS of the probe may lose its validity in case of perfect crystalline tip, due to appearing of sharp resonances and electronic states [PHM+98] [KJ10] [PBGRS05]. Summarising, these electronic issues may play an important role in case of investigation of metallic surfaces, whereas in case of semiconductor samples used in this work, it is assumed that electron population differ significantly and in comparison with Si the W tip have an constant DOS. Furthermore, numerous calculations build on previously presented assumptions show good correlation between simulation and experiment.

2.2 Substrate systems and preparation

In this section the substrates and surfaces used in this work will be described. The Si will be introduced at the beginning and different surface reconstructions or structures on surface will follow. Along with the characterisation of these structures, details of the preparation are given.

2.2.1 Si bulk crystal and Si(111) 7x7

The Si crystal has diamond lattice structure; the face-centred cubic (FCC), with Si atoms filling half the interstitial sites in tetrahedron. The atomic mass of Si is 28.085 u and in periodic table its group is 14, carbon group is IV, period is 3 and block is p. Melting point of Si is 1414 °C and lattice constant is 5.43 Å. It is an semiconductor with a indirect band gap of 1.1 eV at RT for the undoped crystal and the work function for (111) face is ∼4.6 eV. It has been investigated with numerous experimental methods [LSZ94]. It is also the most often used material in electronic industry.

Not only the possibility to create high purity (1 impurity atom per 10^{10} Si atoms) single crystals is an advantage, but also controllable doping (with both doping types - p and n). The most often used methods for production of silicon are the Czochralski [Czo18] and the Float-Zone techniques. The first one is mostly used for chip industry, whereas the latter is used for special applications, which demands extremely high quality and purity crystals.

Different angle of cutting the crystal gives different crystallographic planes of the wafer surface. The most common used surface plane is (100), because it is used
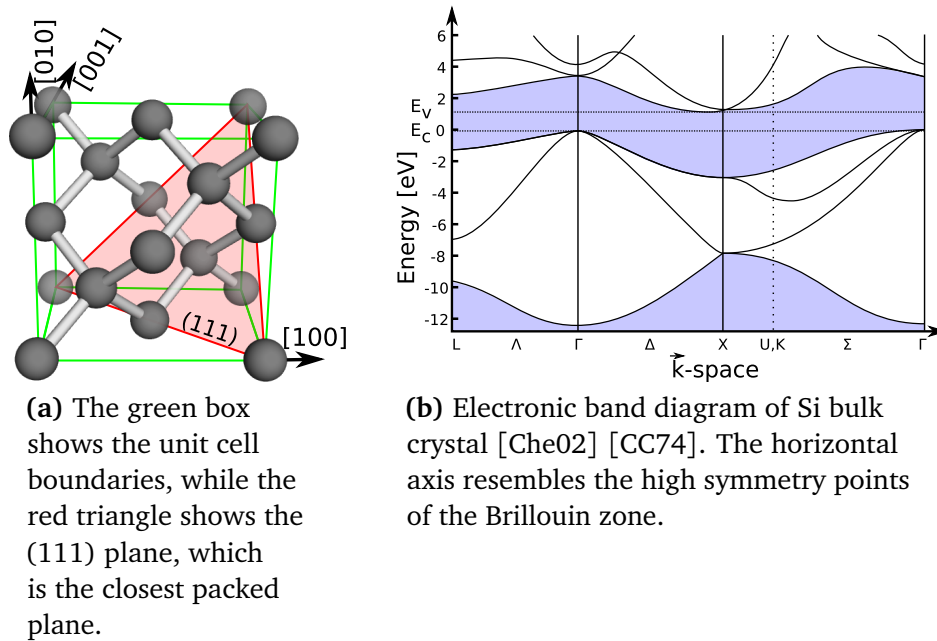
(a) The green box shows the unit cell boundaries, while the red triangle shows the (111) plane, which is the closest packed plane.

(b) Electronic band diagram of Si bulk crystal [Che02] [CC74]. The horizontal axis resembles the high symmetry points of the Brillouin zone.

Figure 2.7: The electronic and structural form of Si bulk crystal.

in many microelectronical applications. The second mostly used surface is (111), followed by uncommon surfaces like (110), (557) and other high index planes.

Wafers with slightly different cutting angle, doping or type have been used. When it is not explicitly mentioned, then a Si(111) with polishing angle of 0° to 1° relative to the (111) plane is used. Usual thickness of the wafers used in experiments in this work was 350 μm. The most commonly used Si dopants are acceptors from group III or donors from group V. Boron is a group III element used as a p-type dopant, whereas phosphorus and arsenic are group V elements used as n-type dopants. Usually used wafers are n-doped with specific electrical resistivity ρ lower than 0.1 Ωcm, with dopant concentration of $n > 10^{17} cm^{-3}$. Such high doping concentrations are convenient for preparation of Si in UHV.

In this work (111) oriented Si-wafers have been used (the (111) plane is sketched in Figure 2.7), which has a characteristic stable surface reconstruction called 7x7. In order to lower the energy, the Si(111) surface undergoes a characteristic reconstruction, which changes the structure of five topmost layers. This structure was widely investigated by spectroscopic means, LEED [McR83a] [McR83b], ion channeling [BFK+83] and it was one of the first surfaces observed with STM by Binnig and Rohrer

[BRGW83]. The accepted model for Si(111) 7x7 surface reconstruction, presented in Figure 2.8, is called "Dimer-Adatom-Stacking fault" (DAS) model and was proposed by Takayanagi in 1985 [TTTT85b] [TTTT85a]. The significant reconstruction of the surface, leads to a change of the electronic band structure, visible by the appearance of Si surface states [Nor86] [HTD86] [LHK+94] [CH80] [Ven94]. The S_1 surface state at -0.35 eV originates from the adatoms and the S_2 surface state at -0.8 eV from the rest atom positions and the corner-hole atoms. At energy $+0.7$ eV relative to the Fermi level, a S_1' surface state can be found which is assigned to dangling-bond states located at the adatoms near the corner holes. These values correspond with the measurement in section 3.3.

Considering Figure 2.8, in each unit cell of this structure there are 12 adatoms (red spheres), nine dimers (blue spheres) and corner hole in each corner - hallmark of Si 7x7 in STM. One of the triangular halves of the unit cell has a stacking fault. According to the model, there are 19 dangling bonds left in each unit cell, compared to 49 of the unreconstructed surface. The Si bulk atomic distance is 0.235 nm and the reconstructed Si(111) 7x7 surface unit cell is 2.6882 nm. The single Si atomic step is 0,314 nm high.

A real image of the surface is shown in Figure 2.9. The image on the left side is the STM image and on the right side a corresponding LEED pattern.
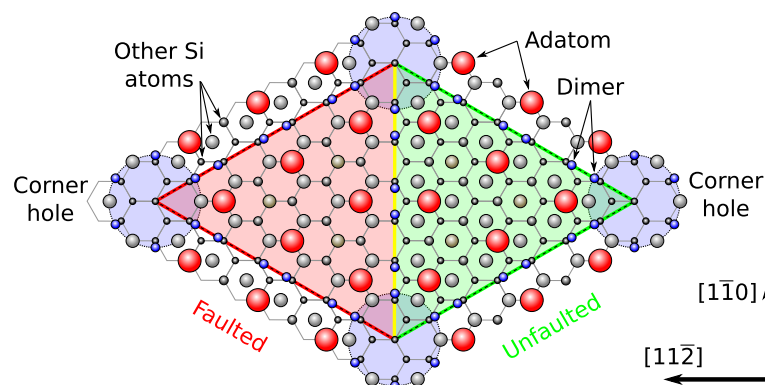
Figure 2.8: Si(111) 7x7 reconstruction; the Dimer-Adatom-Stacking fault (DAS) model [TTTT85b] [TTTT85a]. In each unit cell of this structure there are 12 adatoms (red spheres), nine dimers (blue spheres) and corner hole in each corner - hallmark of Si 7x7 in STM. One of the triangular halves of unit cell has a stacking fault. According to the model there are 19 dangling bonds left in each unit cell, reduced from 49 of the unreconstructed surface.

2.2.1.1 Preparation

Wafers were cut at appropriate angles to obtain given crystallographic surface, polished and cleaned by the manufacturer as follows: Chemical cleaning and the oxygen plasma etching. As the Si element is reactive, the polished and cleaned surface oxidises in air and leaves the wafer with thin SiO_2 layer. This oxide is enough to prevent surface contamination of Si sample.

The preparation for Si(111) 7x7 surfaces was as follows: After chemical cleaning (with acetone, isopropanol and petroleum), the sample was mounted in the vacuum chamber and degassed for around 12 hours at a temperature of 600°C. The sample was heated with direct current and the temperature was measured with an infrared pyrometer. This step removes most of the residues, such as water, solvents etc., but keeps the protective oxide layer intact. In the following preparation step, the sample is heated slowly to ~1000°C to remove the oxide and then the temperature is increased abruptly to ~1200°C for a few seconds. This, the so called flash, was repeated a few times. During these temperature steps it is critical to keep the pressure at least below 10^{-9} mbar to avoid building of silicon carbide, therefore heating needs to be slow
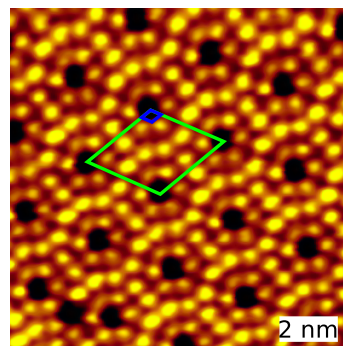
(a) STM empty-states picture of the clean Si(111) surface (+2V 0.25nA). The 7x7 unit cell is shown by green polygon, while 1x1 sub-structure is depicted by the small blue polygon.
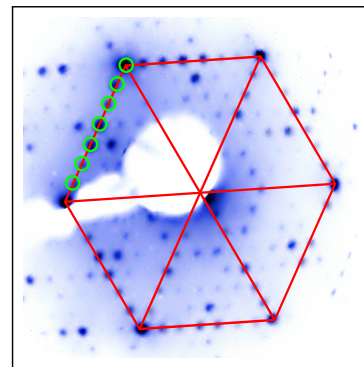
(b) Optical LEED picture of the clean Si(111) surface (60 eV). Red polygon shows the first Brillouin zone spanned over the 1x1 spots and green circles emphasise the 7x7 spots.

Figure 2.9: Figures present STM and LEED measurements of the same Si(111) sample with the 7x7 surface reconstruction.

enough in order to stay in the safe pressure range. In the vacuum chamber used in this work, the starting pressure for preparation step was in 10^{-11} mbar range. After the last flash, temperature is decreased from ~1000°C to 750°C and the sample was kept at this temperature for up to 30 minutes. This last step is called healing and ensures large terraces with an excellently ordered 7x7 reconstruction.

After preparation, the surface quality was checked with STM and/or LEED before taking further experimental steps. The spots of the LEED image should be sharp, consist of well defined 7x7 surface reconstruction (as visible in Figure 2.9b). In the STM surface is flat, atomic resolution of Si 7x7 structure is easily obtainable with low amount of defects. If the quality of the Si(111) 7x7 surface was not optimal, the high temperature steps of preparation were repeated.

2.2.2 Si(111) / Ag $\sqrt{3} \times \sqrt{3}$ R30°

(a) STM empty-states picture of the clean Si/Ag surface (+2V 0.1nA). The green polygon shows the Ag $\sqrt{3} \times \sqrt{3}$ unit cell.

(b) LEED picture of the clean Si/Ag surface (60 eV). Red polygon shows the first Brillouin zone spanned over the 1x1 spots and green circles emphasise the Ag $\sqrt{3} \times \sqrt{3}$ spots.
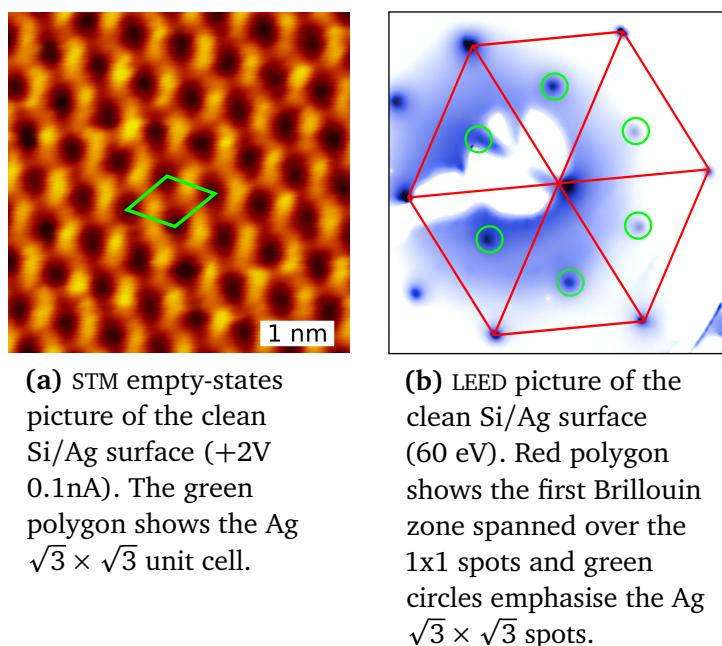
Figure 2.10: Figures present STM and LEED measurements of the same Si(111)/Ag sample with $\sqrt{3}x\sqrt{3}$ surface reconstruction.

When ~1 ML Ag layer on Si(111) is annealed at ~500°C, the Ag $\sqrt{3} \times \sqrt{3}$ reconstruction is formed (see Figure 2.10). The first real space image of the surface was obtained in 1987 by Wilson et al. [WC87]. The metal on semiconductor system is interesting

not only for electronic studies, but also as a complex structural system undergoing a full surface reconstruction. The electronic properties of Ag $\sqrt{3} \times \sqrt{3}$ differ significantly from the Si(111) 7x7 and the reconstructed surface does not show characteristic Si surface state any longer (see Figure 2.11). The Ag $\sqrt{3} \times \sqrt{3}$ structure is rotated by 30° according to the underlying Si 7x7 [BHY+90]. The unit cell of this reconstruction is 0.665 nm large and the height of the first Ag layer over perfect Si surface is 0.29 nm [TNO+88]. This model was confirmed by the ab-initio calculations conducted by Ding et al. [DCH91].
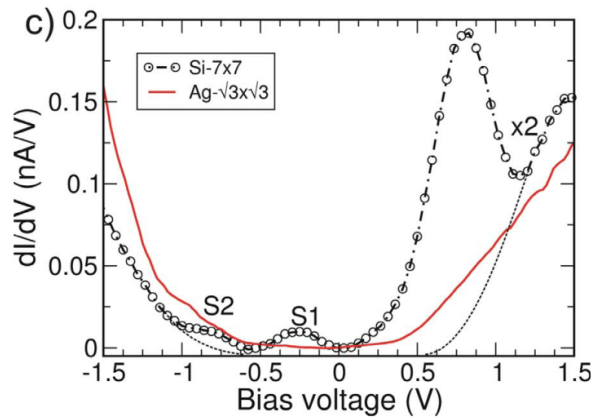
Figure 2.11: Comparison of experimentally obtained LDOS from clean Si(111) 7x7 surface and Ag $\sqrt{3} \times \sqrt{3}$ reconstruction [SPT09]. Complete structural and electronic reconstruction is supported by disappearing of the Si characteristic peaks.

The conductance of the Si(111) Ag $\sqrt{3} \times \sqrt{3}$ surface is increased in comparison to the Si(111) 7x7, but there is a low DOS around Fermi level. The perfect Ag $\sqrt{3} \times \sqrt{3}$ show no band-gap, but is found to be half-metallic, that is, the occupied states touch the Fermi surface [CGM+05]. The influence of dopant of the Ag $\sqrt{3} \times \sqrt{3}$ have been studied, leading to the conclusion that already excess of Ag on the surface lead to significant change in electronic characteristic. In this system a two-dimensional electron gas (2DEG) can be created due to excess of Ag. Thus, the half-metallic Si/Ag surface reconstruction can degenerate into metal, as shown by Crain et al. [CGM+05] [THI97]. This system and its electronic characteristics will be investigated and discussed in section 3.3.

2.2.2.1 Preparation

Depending on the coverage and temperature a variety of different Ag reconstructions
have been found on the Si(111) surface, as shown in Figure 2.12. The phase diagram
by Wan [WLN93] gives an overview over different structures obtained by different
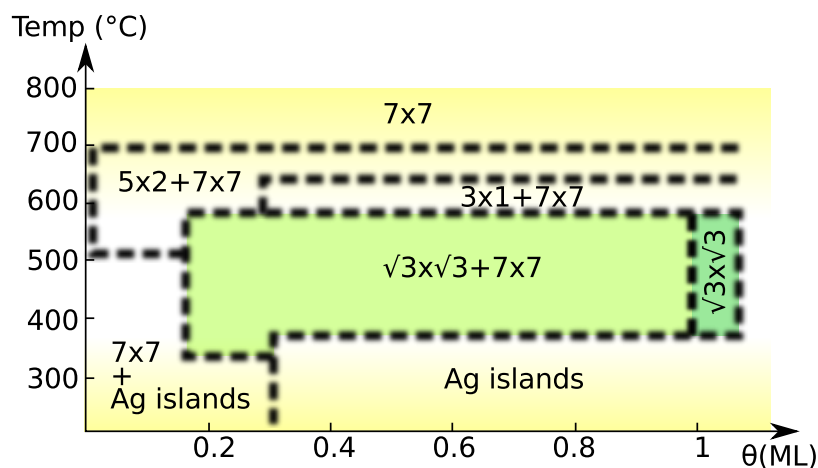amount of deposited material and different annealing temperatures.

Figure 2.12: Phase diagram of Ag $\sqrt{3} \times \sqrt{3}$ surface after Wan et al. [WLN93].

By evaporation of 1 ML of Ag on reconstructed Si(111) 7x7 one obtains an homoge-
neously distributed layer of atoms [TN88]. Ag was evaporated out of molybdenum
crucible with use of electron bombardment. Further annealing to $\sim 500°$C, allows the
full surface reconstruction [WLN93], the Si(111) 7x7 characteristic peaks disappear in
LEED and the LDOS surface state is suppressed in spectroscopic picture. The Ag creates
flat, much more chemically inert surface reconstruction, with smaller unit cell than
the previous Si(111) 7x7.

During the evaporation process the material is deposited randomly over the area of
the sample, so that many nucleation points are created, which together with limited
mobility, lead to equally distributed island growth [WLN93]. Diffusion tends to create
larger islands, thus single atoms, or small mobile islands can attach to larger island.
Along with the growth of islands, the diffusion of material on the surface slows down
and at some point the size of island reach critical size in which make them immobile.

The complex thermodynamics of growth of this system can be seen in Figure 2.12.
On the perfect flat Si(111)surface, the created Ag $\sqrt{3} \times \sqrt{3}$ reconstruction is not flat.
Depending on temperature and annealing time, different sizes of Ag $\sqrt{3} \times \sqrt{3}$ islands

are formed. The longer the annealing step, the more perfect the surface. As the Ag $\sqrt{3} \times \sqrt{3}$ unit cell consists of 3 Ag atoms, each bonded to a Si counterpart, extra Si is released from the first layer. This "etching process" upon forming the Ag $\sqrt{3} \times \sqrt{3}$ reconstruction leads to formation of additional Ag $\sqrt{3} \times \sqrt{3}$ adislands on top.

2.2.2.2 Honeycomb-Chained Trimer HCT model

The Honeycomb-Chained Trimer HCT model, shown in the Figure 2.13 is the accepted model of Ag $\sqrt{3} \times \sqrt{3}$ surface. Its appearance in STM is similar to a honeycomb structure, therefore its name. First the Ag $\sqrt{3} \times \sqrt{3}$ reconstruction on Si was observed by K.Spiegel in 1967 [Spi67], whereas first STM measurement of this structure was conducted by R.J.Wilson et al. [WC87]. Detailed studies of preparation of this reconstruction were carried out by E.Bauer and by H.Poppa [BP72]. By now this model is supported by various measurements, among others by: surface X-ray diffraction [TNO+88] [VGV+89], LEED [YTKT82] [FIHT89], STM [WC87] [LDTH87] [RDV92] and is also supported by calculations [DCH91].

(a) HCT model with trimerised Si atoms on top of T_4 site.

(b) HCT model with trimerised Si atoms on top of H_3 site.
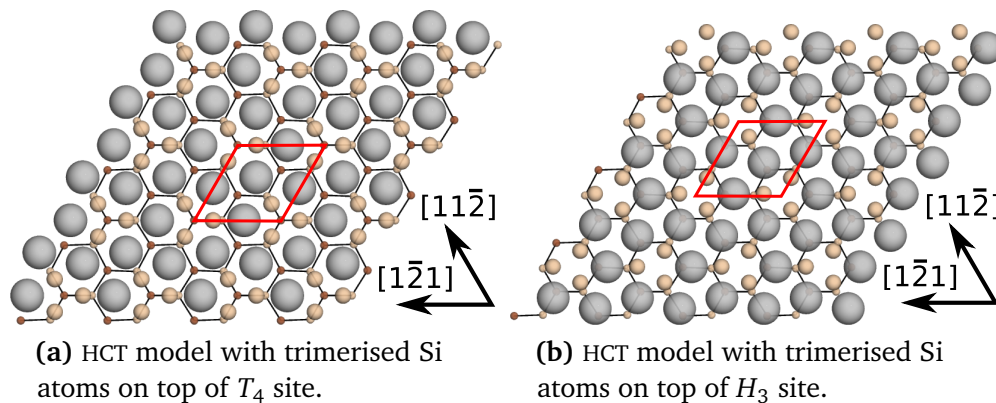
Figure 2.13: Two conformations of the HCT Ag $\sqrt{3} \times \sqrt{3}$ structure [WLN93]. The black hexagonal matrix with small dark brown atoms depicts the bulk Si layer. Large gray balls are Ag atoms. Light brown balls depict the 1st and 2nd Si layer. In both cases, three 1st Si layer atoms and three 2nd layer atoms surround the Ag unit cell corner (corner hole). The difference is visible at the 3rd (bulk) Si layer atoms, which in one case are visible in the middle of corner hole, while in the other case, they surround the corner hole. **Model by courtesy of Wei Chen.**

2.2.2.3 InEquivalent Triangle IET Model

It should be noted that recent investigations have shown that the Ag $\sqrt{3} \times \sqrt{3}$ at low temperatures undergoes a structural transition from the HCT to the IET model [ATSH99] [SNH99]. The IET model is an asymmetrical variation of HCT and is shown to be stable at low temperatures.

As mentioned before, the HCT model unit cell consists of two mirror symmetric triangles, indistinguishable from each other (see Figure 2.14a). The transition to the IET structure shifts middle Ag atom in the Ag $\sqrt{3} \times \sqrt{3}$ unit cell towards one of the triangles. The new unit cell of IET has equal size as HCT, but consists of two in-equivalent triangles called IET+ and IET- (see Figure 2.14b). Similarly to Jahn-Teller distortion in molecules or Peierls distortion in 1D, 2D systems, the disorganisation of the HCT symmetry at low temperatures results in energy lowering.

(a) HCT model with mirror symmetric triangles.

(b) IET model with in-equivalent triangles.
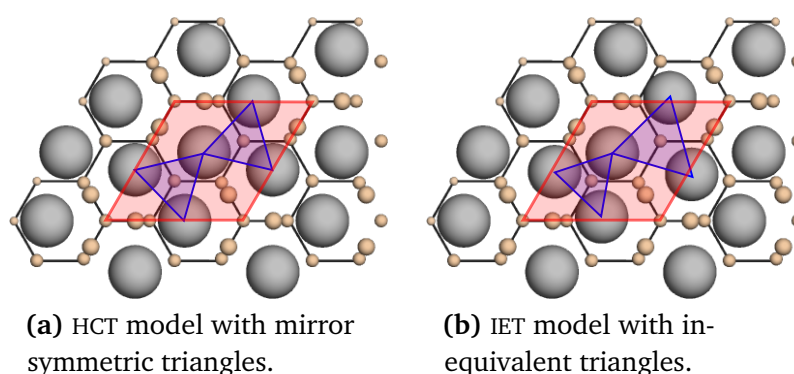
Figure 2.14: Comparison of the standard HCT model and the new proposed IET model. The Ag atom in the middle of the unit cell (marked in red) is shifted and the mirror symmetry of two triangles (marked in blue).

Even though Ag $\sqrt{3} \times \sqrt{3}$ has been thoroughly investigated by numerous experimental methods since '80s, the finding of the IET phase and appearance of this new structure at RT which has been observed recently [SNH99] [ZGJ06], thus making the Ag $\sqrt{3} \times \sqrt{3}$ surface a subject of active discussion. It has been noted, that the appearance of this new structure may be due to "tip-effect" or an "tip-induced-phase" in STM as well. On the other hand, recent X-Ray diffraction [TSN+03] and Photoelectron diffraction [SSM+06] measurements, show that IET appearing in very low temperatures is a meta-stable phase.

Summarising, the coexistence of the two new structures leads to creation of another

type of domain walls which lowers the strain between different IET phases. In this work, the Ag $\sqrt{3} \times \sqrt{3}$ does not reveal the IET structure and the domain walls are visible also at RT. The study presented here rely on the HCT model and not on the still actively discussed IET model.

2.2.3 Ag on Si cluster matrix

In section 3.3 mesoscopic transport effects such as Coulomb blockade will be investigated in detail using Ag atomic matrix deposited on Si(111) surface. In order to prepare such Ag matrix structure on Si, $\sim$0.5 ML of Ag were deposited at 50 K. The deposition leads to randomly spread atom arrangement on the surface. Usually, in order to obtain a closed layer, elevated temperatures are needed, whereas here the sample was kept at LT, thus diffusion was strongly suppressed. This lead to an Ag atoms matrix on Si surface, which, among other structures, is investigated in section 3.3.

Deposition of Ag on Si in LT does not influence underlying Si(111) 7x7 structure, as well as electronic properties remain intact [SPT09].

2.2.4 Ag islands and multilayers

Thick Ag layers on Si will be investigated in section 3.3. Silver deposited in amounts larger than 1 ML grows in islands with well defined heights, so called, magic heights [MH08]. Ag growth on Si at RT follows basically the Stranski-Krastanov mode [GI83].

Under elevated temperature conditions, needed for the preparation of Ag $\sqrt{3} \times \sqrt{3}$ reconstruction, the Ag growth on Si shows the Frank-van der Merwe mode [MWP79] [VDJ80] [LITV84] [OKMS03] [OGA89] [NMY96]. As mentioned before, single Ag layer annealed to $\sim$500°C leads to the Ag $\sqrt{3} \times \sqrt{3}$ reconstruction, while further Ag deposition creates flat crystalline Ag surface.

In this work both approaches were used, the growth of islands and layers on reconstructed Ag $\sqrt{3} \times \sqrt{3}$ and directly on Si(111) 7x7 surface.

2.3 Molecules

An extended motivation for molecular electronics was given in the introduction part. A large set of different molecules, with different expected characteristics, were

investigated throughout last two decades. In this work, the adsorption of Ferrocene-1,1'-dithiol on Si(111) Ag $\sqrt{3} \times \sqrt{3}$ has been studied in detail. A brief description of the molecule is given in the following.

2.3.1 Ferrocene-1,1'-dithiol FDT

The use of organometallic molecules in surface science is are relatively new, but becomes more and more interesting, because its significantly higher conductivity compared to fully carbon-based molecules [GEW+05]. Organometallic molecules contain carbon-metal bonds, therefore are in area between inorganic chemistry and organic chemistry. Ferrocene belongs to the group of organometallic molecules and is a, so called, metallocene. Two cyclopentane (cyclopentadiene, Cp) rings create sandwich compound with an metal atom in the centre, presented in Figure 2.15a. This molecule was first prepared in 1951 by Pauson and Kealy [KP51], but Ernst Otto Fischer and Geoffrey Wilkinson received the Nobel Prize in Chemistry in 1973 for their investigation of molecular "sandwich compounds" [Pri73].

The chemical formula of Ferrocene is $Fe(C_5H_5)_2$, with molecular mass of 186 g/mol. Ferrocene dithiol is a molecule with chemical formula $Fe(C_5H_4SH)_2$ and significantly higher molecular mass of 250 g/mol (see Figure 2.15b). The additional thiol groups attached to Cp rings give the molecule the ability to create a strong bond, e.g., to a Ag surface. Details about the bonding strength, adsorption geometry and dissociation can be found in [MBTP06] [Mey06]. The Cp rings can rotate in respect to each other, changing the distance between thiol groups, thus giving the molecule the ability to adjust its size within some range, appropriately to the gap size. Hence, this allows the stressless adsorption of molecule on the surface or structure.

2.3.1.1 Deposition

Deposition of FDT was done using a Knudsen Cell, which was made from ceramics and cleaned appropriately. The Knudsen Cell hosts also a thermocouple to control reliably the sublimation temperature. The purification process was done at temperatures around 120°C, This allows to remove residual water and chemical impurities from the FDT molecule powder. The whole process is controlled by a RGA (Pfeiffer PrismaPlus™ QMG 220 - Quadrupole mass spectrometer). The RGA in our setup allows the measurement of atomic masses up to 200, therefore a direct proof of the existence of intact
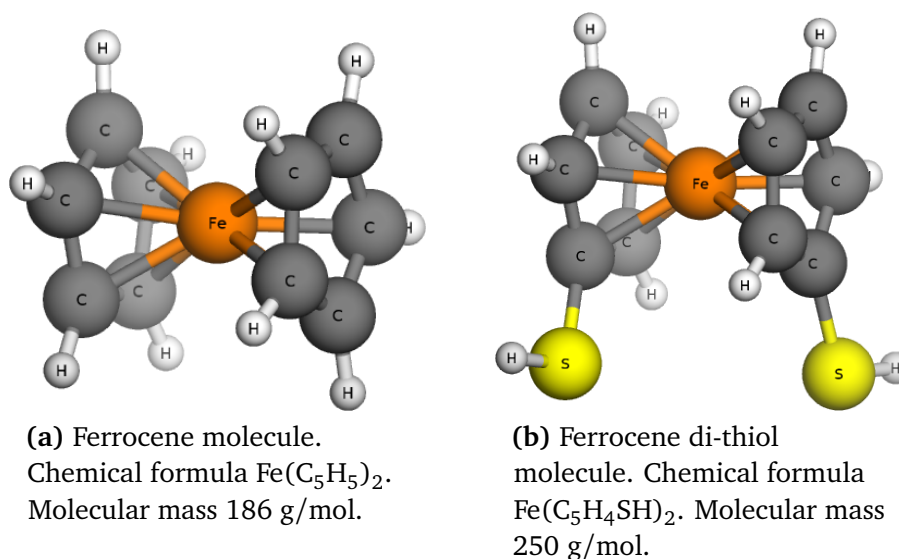
(a) Ferrocene molecule. Chemical formula $Fe(C_5H_5)_2$. Molecular mass 186 g/mol.

(b) Ferrocene di-thiol molecule. Chemical formula $Fe(C_5H_4SH)_2$. Molecular mass 250 g/mol.

Figure 2.15: Model of FDT molecule and its basic molecule, Ferrocene.

FDT molecules was not possible. The indirect proof is the existence of peaks in RGA at 186 and 184 (see Figure 2.16). The first one is a stable Ferrocene molecule, while the latter peak with atomic mass 184 is a ionised Ferrocene molecule. Nevertheless, a intact adsorption was finally proven by imaging the molecule with STM.
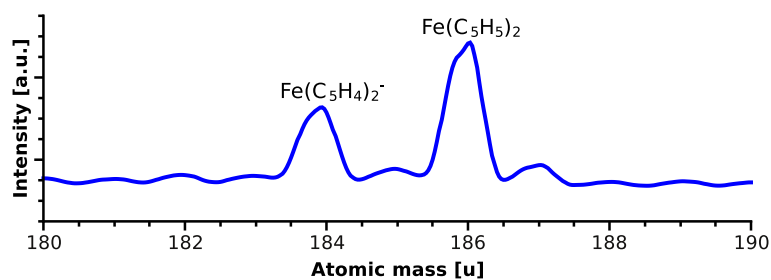
Figure 2.16: RGA measurement during deposition of FDT molecules. With molecular mass 186 u the standard Ferrocene molecule is visible, whereas the mass 184 u shows the ionised FDT molecule without thiol groups.

The Ferrocene-1,1'-dithiol molecules, were prepared by the Prof. Butenschön group at the Leibniz University of Hannover [MVM+08] [BB10].

2.4 Domain walls - 2D dislocations

Investigations of defects in crystals goes back to the beginning of the crystallography and solid state physics. The first investigation in area of grain boundaries in crystals (3D dislocation defects) were done in early 50' [RS50]. Eventually, due to lack of local surface investigation methods, domain walls (2D surface dislocation defects) became a topic of interest much later [HF82].

Crystallographic defects in crystals occur generally due to impurities or influence of the crystallisation process. Defects in crystals are divided in point defect, line defects and planar defects.

Dislocations can be found at surfaces (limited to two dimensions) and in crystal bulk (the three dimensional crystal defects). In this work the two dimensional defects on the surface are of interest. Simplified models of domain walls are presented in Figure 2.17 on the basis of a Kossel crystal surface. In each figure, the red and blue line shows the orientation and position of the left and right domain, accordingly. The green mesh shows the underlying crystalline structure, whereas each crossing green line represents a valid position for the grey atoms. Figure a) depicts crystalline surface without defect, therefore separation between atoms in each direction is equidistant. Figure b) shows a light domain wall, that is, the average atoms density is lowered due to domain wall existence. Figure c) shows a heavy domain wall, that is, the average atoms density is higher due to domain wall existence. Figure d) presents a situation in which the right domain wall is shifted by 1/3 of the atomic distance upwards (equivalently 2/3 of atomic distance downwards). The last example in Figure e) shows a rotation of the right domain. In each example, the grey atoms are placed along the underlying crystalline structure (green mesh).

(a) No dislocation. Perfect crystal.

(b) Light domain wall. Atoms density lowered.

(c) Heavy domain wall. Atoms density increased.

(d) Different shift vector. Domain shifted along the domain wall.

(e) Rotation defect. Domain rotated.
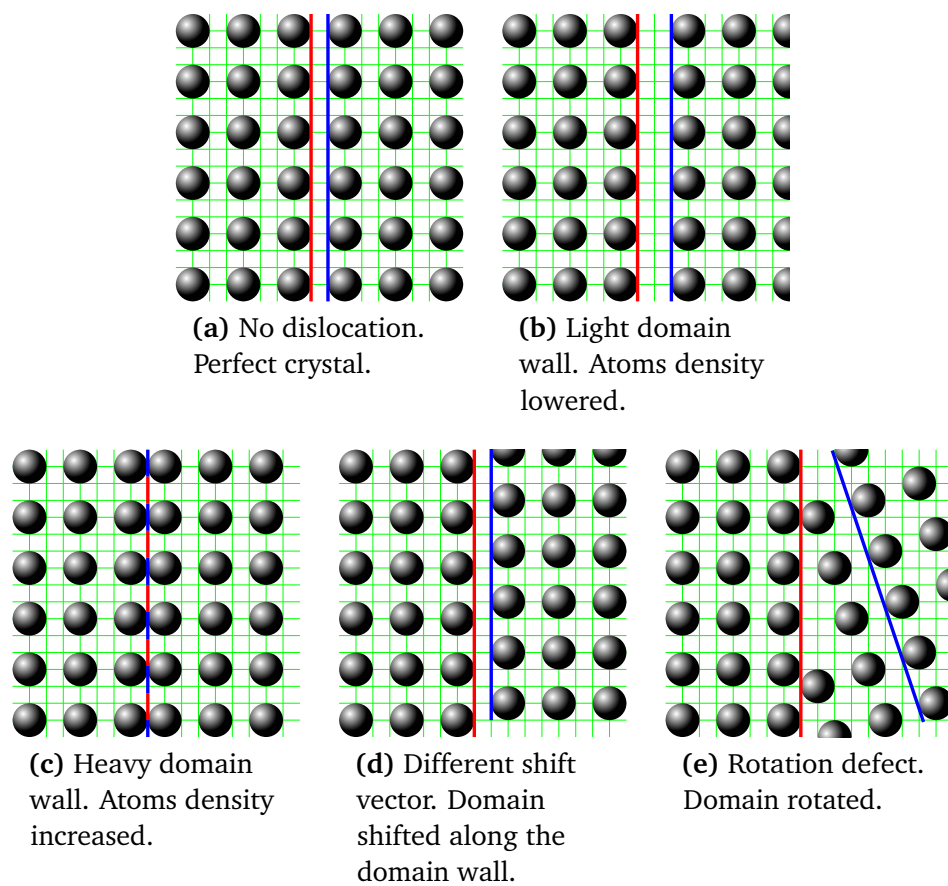
Figure 2.17: Crystallographic defects on surface between two crystallographic domains, so called domain walls.

2.5 Simulation

The calculations presented in this work were performed by courtesy of Wei Chen. The Vienna Ab-initio Simulation Package (VASP) calculations [KH93] were done within the framework of the Density Functional Theory (DFT) [KS+65] in the Generalised Gradient Approximation (PBE-GGA) [PBE96]. A plane-wave basis set and the Projector Augmented Wave (PAW) pseudo-potentials [Blö94] were employed. For the Brillouin zone sampling, an 2x2x1 Monkhorst-Pack k-point mesh [MP76] was used. The energy cutoff for the kinetic energy was 400 eV.

2.6 Mesoscopic physics

2.6.1 Schottky barrier (SB)

In section 3.3 will be shown that depending on the preparation procedure of the Ag structures on Si, a metal-semiconductor junction can be realised. In the case when metal and semiconductor are placed in contact, an inner potential barrier is created. Such system is called a metal-semiconductor junction and the barrier is called a Schottky barrier (SB). Since its invention in late 30' by Walter Schottky, it has been discussed both experimentally and theoretically [Sch39] [Sch42] [Bar47] [CS65]. Two possible realisations of this system are possible; *n-m* (n-doped semiconductor and metal) and *p-m* (p-doped semiconductor and metal) junctions.

(a) Band diagram of separated metal and semiconductor (n-type).

(b) Metal-semiconductor (n-type) junction in equilibrium.
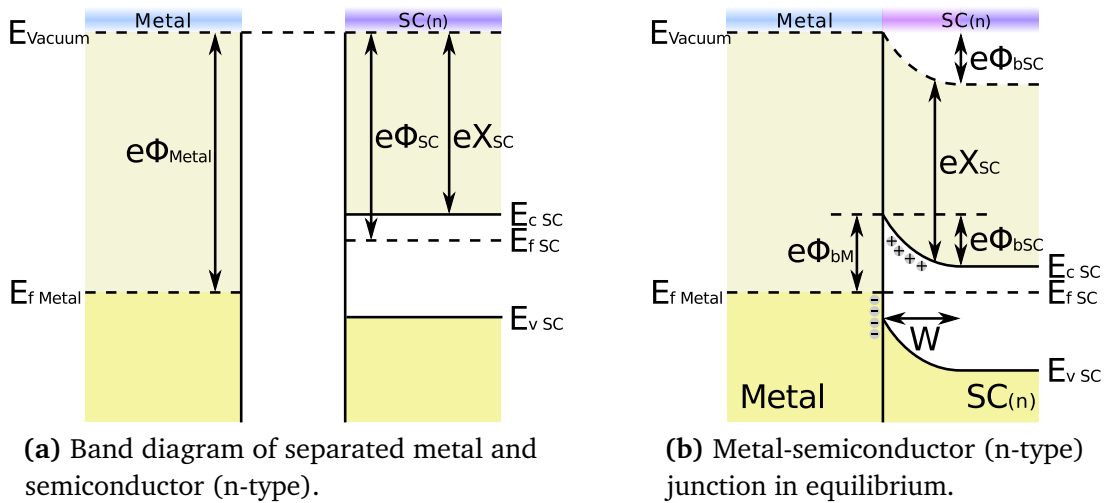
Figure 2.18: Band diagram of metal and semiconductor (n-type) separately and in contact ($\phi_{Metal} > \phi_{SC}$). The E_{Vacuum} is the vacuum level for both systems. $E_{f_{Metal}}$ denotes the Fermi level of the metal and $E_{f_{SC}}$ the Fermi level of the semiconductor. $E_{v_{SV}}$ and $E_{c_{SV}}$ are the valence band and conductance band edges of the semiconductor, respectively. ϕ_{Metal} and ϕ_{SC} are the work functions of metal and semiconductor, whereas X_{SC} is the electron affinity of the semiconductor. After creation of a junction the ϕ_{bM} and ϕ_{bSC} are the barrier heights relative to the metal and semiconductor side, respectively. W denotes the depletion region.

In this study, n-type silicon has been used, hence briefly a *n-m* junction is explained in the following (Figure 2.18). In contact, the chemical potentials in both subsystems will equilibrate. Due to difference in work function (ϕ_{Metal} is larger than ϕ_{SC} in our

case), electrons will flow from semiconductor to metal. By this, the metal surface layer will be charged negatively and accordingly the semiconductor surface layer will be charged positively, due to lack of electrons. Thus, the electric field and therefore a potential gradient - the Schottky barrier, will appear.

(a) Band diagram of separated metal and semiconductor (p-type).

(b) Metal-semiconductor (p-type) junction in equilibrium.
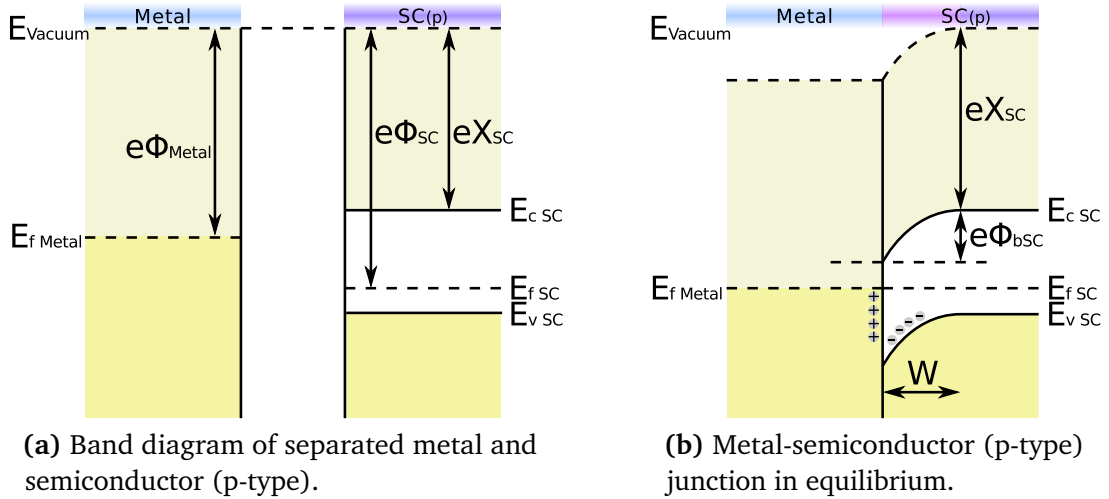
Figure 2.19: Band diagram of metal and semiconductor (p-type) separately and in contact ($\phi_{Metal} < \phi_{SC}$). The E_{Vacuum} is the vacuum level for both systems. $E_{f_{Metal}}$ denotes the Fermi level of metal and $E_{f_{SC}}$ the Fermi level of the semiconductor. $E_{v_{SV}}$ and $E_{c_{SV}}$ are the valence band and conductance band edges of the semiconductor, respectively. ϕ_{Metal} and ϕ_{SC} are the work functions of metal and semiconductor, whereas X_{SC} is the electron affinity of the semiconductor. After creation of a junction the ϕ_{bM} and ϕ_{bSC} are the barrier heights relative to the metal and semiconductor side, respectively. W denotes the depletion region.

In Figure 2.18 the opposite situation is presented. The ϕ_{Metal} is smaller than ϕ_{SC}, therefore after Fermi level alignment the band bending occurs in the opposite direction.

The potential barrier leads to band bending and creates an electric field depletes the interface surface of electrons. The region with excess of positive charge, thus the lack of electrons, is called *depletion region*, and is shown as W in Figure 2.18 and Figure 2.19. The formula for W is as follows:

$$W = \sqrt{\frac{2\epsilon\phi_{bM}}{eN_d}},$$

where ϕ_{bM} is the height of the barrier and N_d (N_a) is the donor (acceptor) concentra-

tion of the semiconductor [CS65].

A reversed biasing enlarges the potential barrier and increases the depletion zone. In case if the positive potential is applied to the semiconductor, the junction is forward biased, thus the potential barrier is lowered and the current starts to flow.

2.6.2 Peierls transition

As it will be presented in section 3.1, the domain wall structure of the Si(111) Ag $\sqrt{3} \times \sqrt{3}$ phase undergoes a temperature driven reconstruction. It will be shown that the phase transition in this 1D defect structure can be reasonably explained by a Peierls distortion [Pei55].

According to the model of a Peierls instability, a 1D atomic chain can undergo a structural transition and lower its energy by doubling its period, as depicted in Figure 2.20.

(a) 1D atomic chain, with a lattice constant a.

(b) Chain after Peierls transition with atoms moved along the chain.

(c) Chain after Peierls transition with atoms moved out of chain axis (buckling).
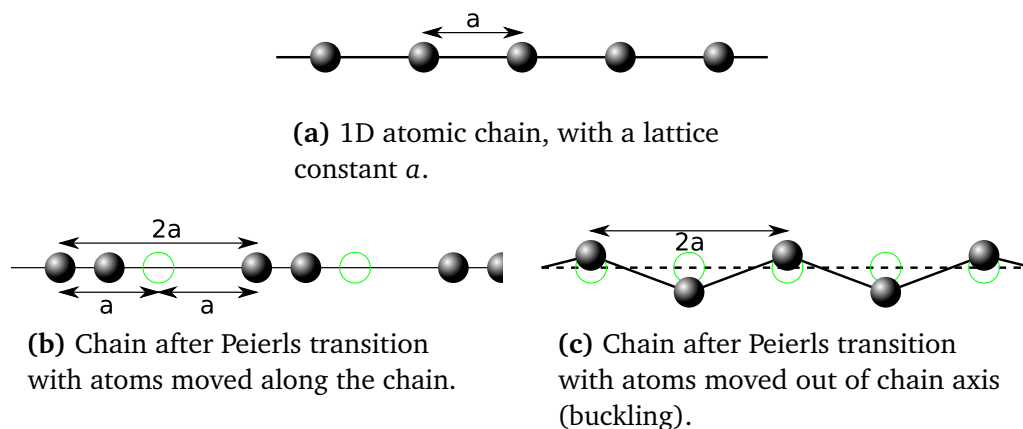
Figure 2.20: The Peierls transition shown on the 1D chain model. The a periodicity in picture a) is changed to $2a$ periodicity after the Peierls transition. The green circles in b) and c) represent the original atom positions.

The 1D atomic chain in Figure a) can undergo a Peierls transition to the structure shown in Figure b) or c). In Figure b) pairs of atoms get closer, leading to increasing distance between these pairs. In Figure c) the change in periodicity is due to atoms buckling. In each case the distortion changes the periodicity from a to $2a$, resulting in a chain of dimers.

Although the distortion costs strain energy, the Peierls state is energetically favoured as it is accompanied by a gap opening in the electronic structure (see Figure 2.21). In
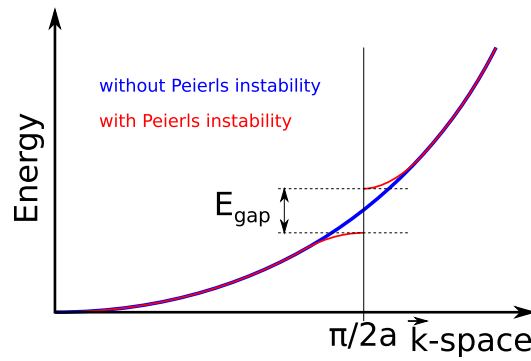
Figure 2.21: Change in the electronic band structure due to Peierls transition. Doubling of the periodicity leads to gap opening, of energy E_{gap}. Blue line is the band structure of perfect 1D chain with a periodicity. Red line is the band structure of chain of dimers.

its simplest form, assuming a half-filling of the bands, the periodic doubling causes a gap opening at the $k = \frac{\pi}{2a}$.

CHAPTER 3

Experiment

The present chapter deals with the experiments. Although most of the introductory and theoretical information was omitted and can be found in chapter 2; some citations and details will be repeated for convenience.

Grain boundaries are found in 3D crystals and were investigated by standard crystallography methods. The existence of domain walls (2D grain boundaries) on surfaces at nano-scale was expected, but the direct investigations waited for appropriate investigation tool [HF82] [ZKDC88].

3.1 Ag $\sqrt{3} \times \sqrt{3}$ substrate and domain walls

This chapter concentrates on the local details of the domain walls of the Ag $\sqrt{3} \times \sqrt{3}$ reconstruction on Si(111) single crystal surface. For the full picture it is important to mention that the grain boundaries, which have been subject of intensive investigation in the past, are the 3D analogon of the domain walls. The grain boundaries are known to have significant influence on the electronic and structural characteristics on meso- and macro-scale [VAB+00]. Furthermore this defect structure can lead to directed electron or mass transport and, as a grain separator plays, among others, an important role in small-scale magnetic applications [SUB+91]. Thus, such microscopic structures are often the trigger for large scale effects.

Domain walls on a microscopic scale are not "visible" using averaging surface science techniques, thus first the introduction of atomic resolution imaging methods gave the appropriate investigating tool. The periodic potential of a single crystal surface allows growth of commensurate and incommensurate structures, hence in the

creation of domain walls, both, substrate potentials and adsorbate, play a role (see section 2.4).

In other words, domain walls, similarly to grain boundaries, occur where two different crystalline structures, islands or grains respectively, meet. The island growth is due to mobility of deposited material, whereas the temperature influences the speed of this process. When the whole surface is overgrown with islands of different orientations, further growth is possible only by material flow from smaller islands to larger ones. When the mass flow stops, the domain walls appear due to existence of structural misfit between islands [SNH99], as no island can undergo a structural reconfiguration to cancel out the misfit. Clearly, on the other hand, two commensurate randomly distributed islands can grow together, creating one larger indistinguishable island. By elevating the temperature, the activation energy for transport can be exceeded, thus increasing the material mobility. As the diffusion is temperature- and time-dependent, the quality of surface can be improved by long healing step.

In contrast to point defects, domain walls may create long chains and preserve the 1D periodic structure through whole length. It is well known that point defects show high chemical activity, due to unsaturated bonds, thus similar behaviour should be found in the domain walls. It is expected that together with the 1D atomic structure, the electronic states will show 1D properties, while being separated from the 2D band structure of the Ag $\sqrt{3} \times \sqrt{3}$ surface. Similar chain structures showing 1D character have been presented and investigated in the past [HKC+01] [HAB+01] [CPT09]. Furthermore, as mentioned in introductory chapters, the perfect Ag $\sqrt{3} \times \sqrt{3}$ is semiconducting, whereas introduction of small amount of adatoms increases the conductance, turning the system into a nearly free electron gas. Here, the band filling of the surface bands is expected to play an important role, as the filling factor is important for stabilising 1D structures, as shown by Crain et al. [CMZ+04] [CP05].

During the process of Si(111) 7x7 surface reconstruction into Ag $\sqrt{3} \times \sqrt{3}$ structure, the characteristic patched landscape appear [WLN93] [GKT+99], visible in Figure 3.1. The height difference of this patches is smaller than the single Si step and the single Ag step. Concerning the HCT structural model of Ag $\sqrt{3} \times \sqrt{3}$, the Ag adatoms are located in the threefold coordination and the trimers in the underlying Si are formed. The formation of Si trimers requires removal of Si atoms from the first Si bilayer and therefore leads to formation of hole-island pairs [ST93] [BÜL+10], making the Ag $\sqrt{3} \times \sqrt{3}$ atomic reconstruction visible on all levels (see Figure 3.2). Furthermore, the valence band is completely filled, as each Ag atom bonds to single Si site. Thus, as

mentioned before, the perfect Ag $\sqrt{3} \times \sqrt{3}$ is semi-metallic. This is one of the main concerns while proposing the domain wall model, because the modified 1D particle density has a direct influence on the electronic properties, therefore, for example, heavy and light domain walls should exhibit different electronic character.

In the paper by J.Schmeidel, H.Pfnür and C.Tegenkamp [SPT11], the Peierls-like phase transitions in domain walls are discussed. The following sections are widely based on this paper, entitled "Peierls-like phase transitions in domain walls".

3.1.1 Preparation

The Ag $\sqrt{3} \times \sqrt{3}$ surface was prepared according to the procedure presented in chapter 2 and investigated by means of STM. The overall quality of the Si(111) 7x7 substrate and the Ag $\sqrt{3} \times \sqrt{3}$ surface was preexamined by means of LEED.

In each measurement set, the same area is presented while varying the bias voltage. Between the sets (new preparation), the set point current is changed, whereas the investigated object was chosen to be similar with the other sets.

The deposited Ag islands are spread randomly on large terraces. Therefore, the domain walls are also similarly randomly spread and oriented. By the use of slightly stepped surface, the grow of islands can be forced to occur near to the step, as a predefined nucleation point. Such processing, makes domain walls grow in a highly predictable way, hence, simplifying the measurement and comparison.

3.1.2 Domain walls

In this part, the domain wall model will be introduced and discussed. The outcome of this discussion will allow the investigation of domain walls in the following sections. Images in Figure 3.1 show overview STM measurements of the Si/Ag $\sqrt{3} \times \sqrt{3}$ structure.

After preparation, on a previously flat surface, the different height levels appear. Silicon atomic steps, emphasised by green arrows, and characteristic patched surface of Ag $\sqrt{3} \times \sqrt{3}$ are visible in the image. As mentioned in the previous chapters, the HCT structure consists of two conformations, depending on the trimerisation site (T_4 or H_3 trimerisation site) of Si atoms relative to underlying Si bulk crystal (see Figure 2.13).

Furthermore, in the figure the bright straight lines are visible, marked by blue boxes. These structures occur on the planes of the same height and are different from the Si steps or Ag patches which mark the borders between plateaus of different

height. Clearly, the former lines originate from stacking faults within the structure and represent the domain walls between different Ag $\sqrt{3} \times \sqrt{3}$ islands.

3.1.2.1 Orientation of domain walls

(a) Ag $\sqrt{3} \times \sqrt{3}$ on stepped Si surface

(b) Ag $\sqrt{3} \times \sqrt{3}$ on stepped Si surface
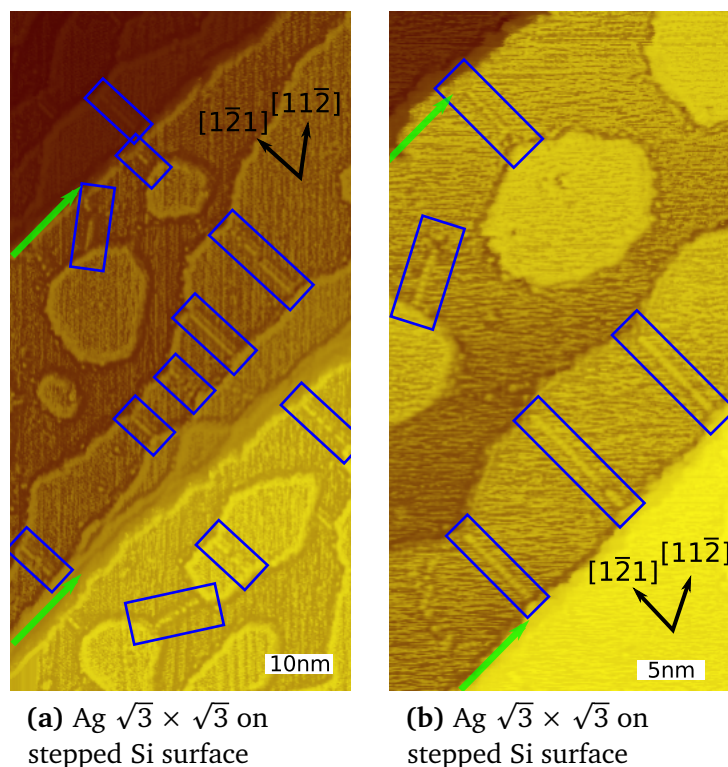
Figure 3.1: The STM images of the domain walls with different directions. Images show that the domain walls grow in any of the <112> directions. Introduction of stepped surface suppresses the random spread and forces the orientation to be perpendicular to the Si step. The blue boxes emphasise the domain walls, whereas the green arrows show the Si steps.

Considering Figure 3.1 and Figure 3.2c, three orientations of domain walls are observed. On the stepped surface, the Si(111) 7x7 terrace edges are aligned along the corner holes of Si, i.e., in the <011> direction. Furthermore, from the fact that the Ag $\sqrt{3} \times \sqrt{3}$ reconstruction is rotated by 30° from the main direction of the underlying Si and that the characteristic Ag domain walls occur often perpendicular to the Si step, follows the chains orientation to be along the <112> directions. The <112> are also the main directions of Ag $\sqrt{3} \times \sqrt{3}$ structure, oriented along the corner holes, thus it

is also the direction of a higher atom density within the domain wall chain.

There are no chains found along the <011> directions or any of the higher index directions. The density of Ag atoms in chains along <011> direction would be lower, compared to both, normal Ag $\sqrt{3} \times \sqrt{3}$ surface and <112> domain wall.

On the basis of Figure 3.1 and Figure 3.2, it can be further concluded that, on larger Ag $\sqrt{3} \times \sqrt{3}$ areas, domain walls occur randomly in one of the <112> directions. Hence as expected, using slightly off-plane polished Si surface the stepped surface is created, thus the domain walls grow in only one direction, perpendicular to the Si steps and parallel to each other.

3.1.2.2 Domain wall structure

In order to construct the model, the detailed investigation of misfit was conducted. In the centre of the Figure 3.2, a domain wall chain is visible. Investigating the surface with atomic resolution, the previously stated <112> orientation of the domain wall is clearly visible.

In the Figure 3.2 a) and b) the Ag $\sqrt{3} \times \sqrt{3}$ unit cells are shown as blue and red boxes. Red boxes depict the overlapping misaligned unit cells. In figure c) an overview image is shown with the domain walls emphasised by the boxes and the white lines showing the main Ag $\sqrt{3} \times \sqrt{3}$ axes.

According to the HCT model, the unit cell contains 3 Ag atoms at non-equivalent sites with respect to the Si substrate. Contrary to simplest domain wall models, where the domain wall would be formed on equivalent sub-lattices of the lattice gas, the shift $\Delta \vec{a}$, by 1/3 of $\sqrt{3}a$ ($a = 3.84$ Å) along the <112> direction does not correspond to a change between equivalent sub-lattices of the Ag $\sqrt{3} \times \sqrt{3}$ structure at the domain wall. It is visible that the misfit vector is 1/3 along the domain wall chain direction (in Figure 3.2 a) and b) the $[1\bar{2}1]$ direction) and the unit cells are periodic parallel to the domain wall.

For threefold coordinated sites, it corresponds to the change from an fcc to an hcp site, or to a rotation by 60°, which is not allowed by a C_3 symmetry operation. For the topmost Si trimers, e.g., this means that they are trimerised around T_4 on one side of the domain wall and on H_3 positions on the other side. For instance, the difference of the triangular structure visible in both domains in Figure 3.2a indicates broken symmetry. However, this effect is small since all other bonding configurations within the topmost layer remain very similar after the shift. A model of the domain wall

along the <112> direction is shown Figure 3.3, with the Ag $\sqrt{3} \times \sqrt{3}$ source unit cells are shifted by $\Delta\vec{a}$ along $[1\bar{2}1]$ direction with respect to each other.

(a) High resolution image, with applied FFT filter.

(b) High resolution image, without filtering.

(c) Area overview with different directions of domain walls.
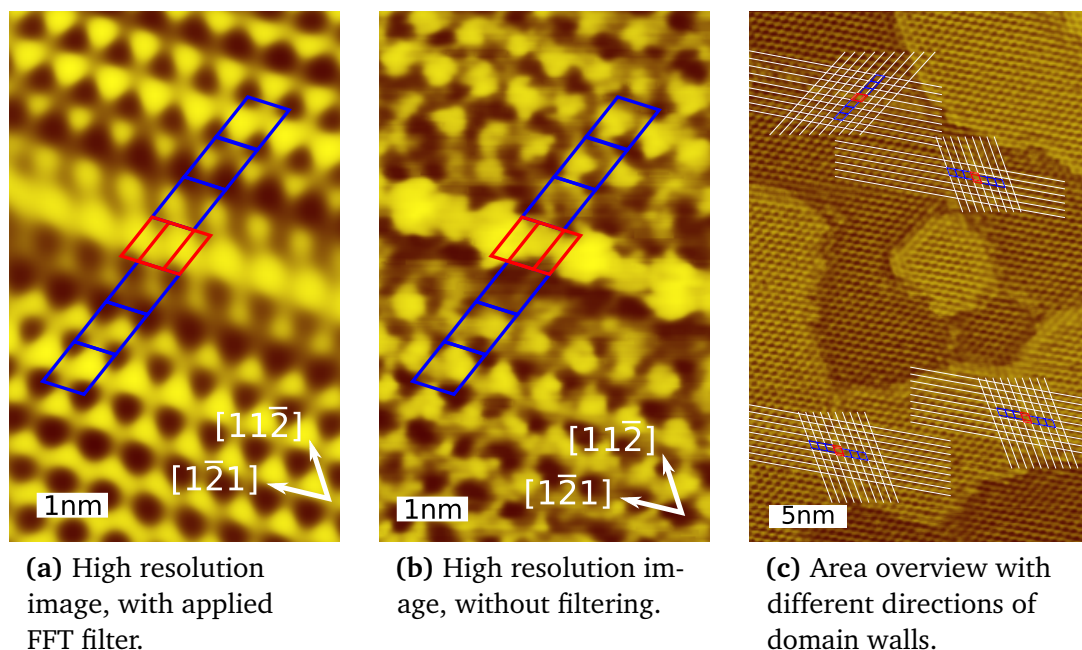
Figure 3.2: The main crystallographic directions have been emphasised in the images to allow the direct calculation of the misfit vector. Over the image Figure 3.2a the FFT filter was applied, to emphasise the periodicity of Ag $\sqrt{3} \times \sqrt{3}$. The blue and red boxes depict the Ag $\sqrt{3} \times \sqrt{3}$ unit cells.

As this model fulfils all experimental findings, it implies that the energetic differences between both types of domains must be very small. Indeed, the main difference concerns the Si-trimer structure relative to the third Si-layer, and this may be the reason why the energetic difference of these two configurations is small. The energetic equivalence of hcp and fcc sites in this case clearly demonstrates that only nearest neighbour interactions are decisive for this chemisorbed system. On the other hand, the energy of domain wall formation is dominant in this case, and any other type of domain wall seems to be energetically highly unfavourable, in particular those that involve domains on equivalent sub-lattices.

In particular, the domain wall model shown in Figure 3.3 is the only one compatible with the positions of the domain wall relative to the Si trimers appearing as dark spots in Figure 3.2. Only the atom density within the domain wall cannot be determined by STM since atomic details within the domain wall cannot be resolved. Furthermore, the
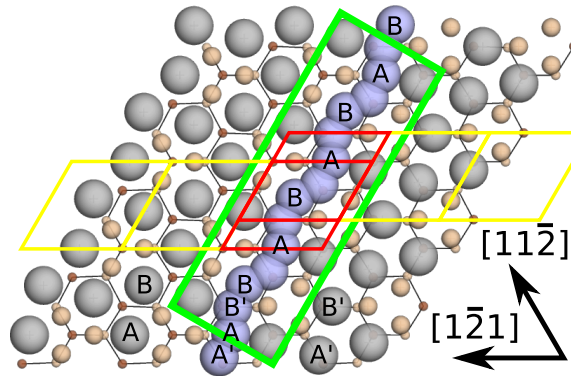
Figure 3.3: The model of the domain wall, aligned along the <112> direction and characterised by 1/3 misfit vector parallel to the the domain wall direction. The grey circles denote the Ag atoms of Ag $\sqrt{3} \times \sqrt{3}$, while the light brown circles depict the Si atoms in the first and second layer. The yellow and red boxes depict the Ag $\sqrt{3} \times \sqrt{3}$ HCT unit cells. The blue circles denote Ag atoms (labelled A,B,A',B') in domain wall chain, for further explanation see text.

atom density within the domain wall depends on the overall Ag excess concentration with respect to the perfect Ag $\sqrt{3} \times \sqrt{3}$ structure. Because of the shifting of the unit cells deduced from the STM images, the centre of the domain wall comprises a superposition of (AB...) and (A'B'...) chains as sketched schematically in Figure 3.3. In the case of the unrealistic scenario that all Ag atoms are present (AA'BB'A...), the unit cell along the domain wall would contain 5 Ag atoms in total. Thus, based on a simple band filling picture, the (A'B'A'...) and (ABA...) configurations are expected to be semi-metallic (containing 3 Ag atoms in unit cell), while the (AA'BA...) and (AA...) configurations should reveal metallic bands with filling factors close to one half. The latter configurations would correspond to heavy and light domain walls, containing 4 and 2 Ag atoms in unit cell, respectively.

3.1.3 Domain walls - Low temperature

Figure 3.4 presents a set of STM measurements of a domain wall at LT. The characteristic Ag $\sqrt{3} \times \sqrt{3}$ honeycomb structure with a low amount of defects is visible. Slightly off-plane Si wafer miscut can be observed by limited Si terrace size, which, as mentioned before, leads the growth of equally oriented domain walls and of similar length (according to the terrace size).

In the first series of measurements a single domain wall was chosen and measured

with different voltages while keeping the tunnelling current at 0.5 nA (Figure 3.4). Preparation procedure was conducted according to the basics described in subsection 2.2.2 and measurements were prepared at temperature 80 K.

(a) STM -1.0 V 0.5 nA

(b) STM +1.0 V 0.5 nA

(c) STM -1.5 V 0.5 nA

(d) STM +1.5 V 0.5 nA
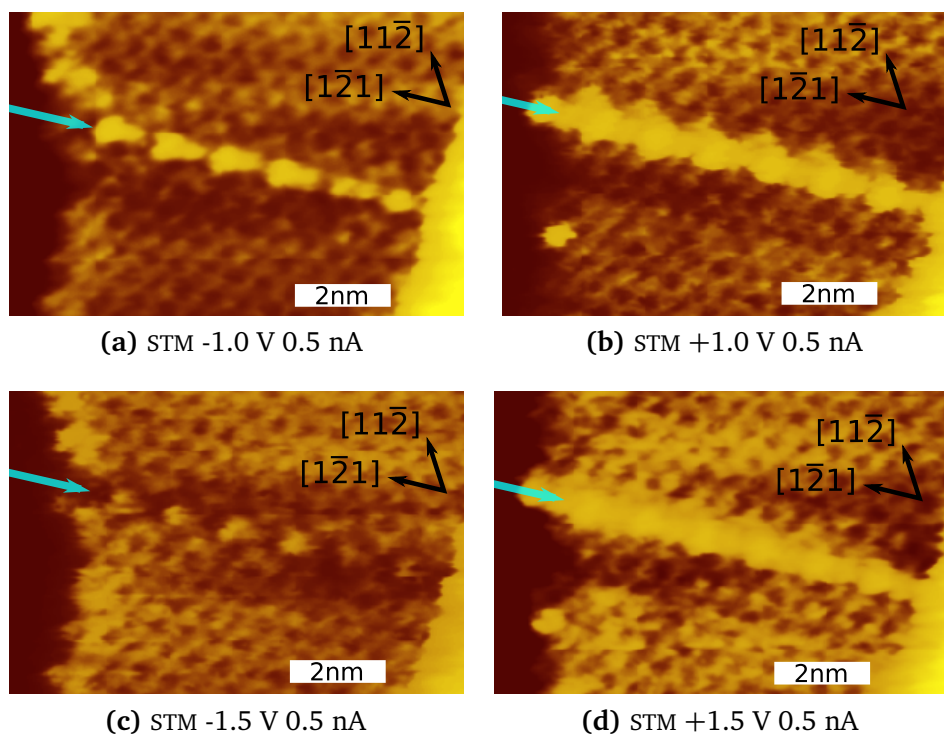
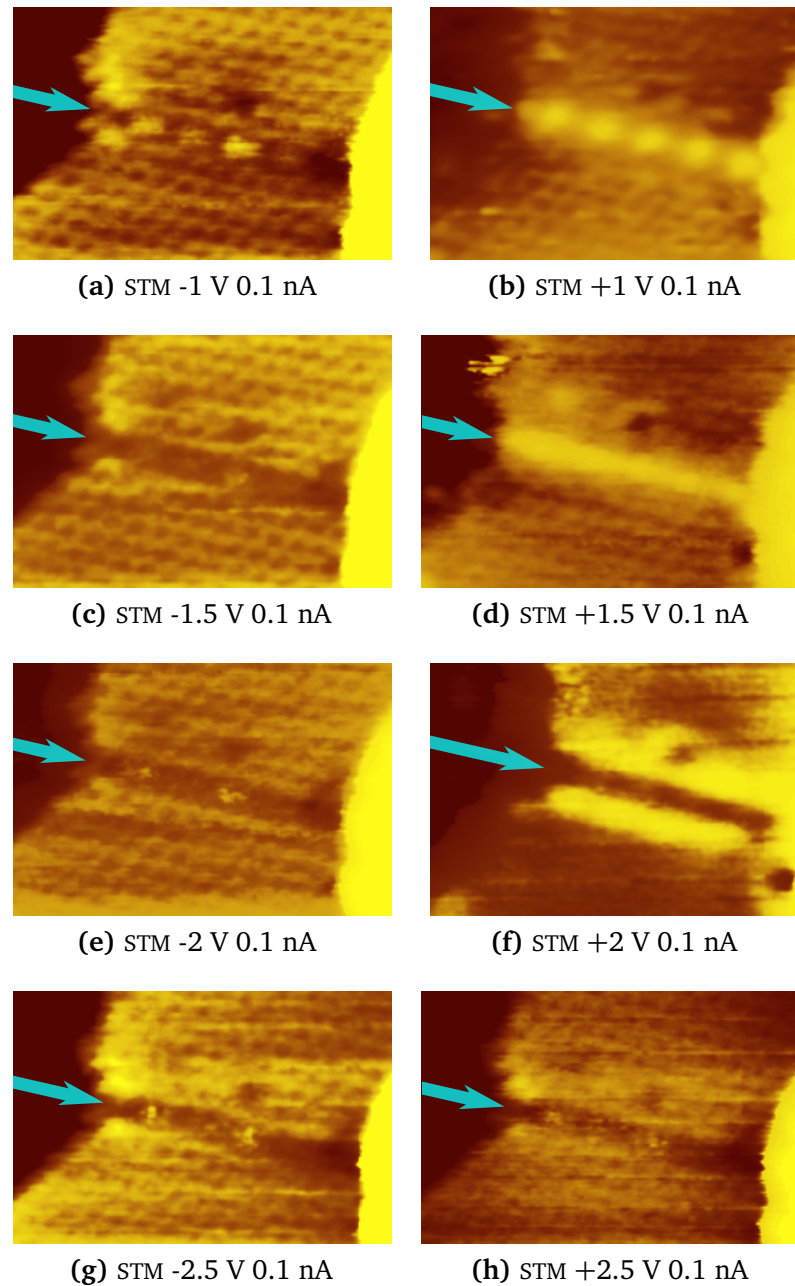**Figure 3.4:** STM measurements of domain wall. Each figure covers an area of 12 nm x 6 nm, allowing for direct comparison. In this measurement series the voltage varied, while the current was constant at 0.5 nA. Blue arrow indicates the direction of linescans shown in Figure 3.7.

The blue arrows in Figure 3.4 show the direction of linescans, which will be investigated and compared below. Each linescan has been taken along the domain wall chain in order to allow a direct comparison.

The Ag $\sqrt{3} \times \sqrt{3}$ reconstruction is not influenced by the voltage variation. In Figure 3.4a at -1 V and Figure 3.4b at +1 V the domain wall is pronounced and an elevation in the apparent height is clearly visible. The image with voltage setting of +1.5 V (Figure 3.4d) is similar to the previous pictures, but at the measurement conducted at -1.5 V (Figure 3.4d) the chain is significantly suppressed and the apparent height is lower than the surrounding surface level.

In order to investigate the influence of the current, further experiments on domain

walls were conducted with different current setting for each measurement set. Figure 3.5 shows set of STM pictures measured with 0.25 nA current setting. Similar to the previous experiment, only the bias voltage was varied.

(a) STM -1 V 0.25 nA

(b) STM +1 V 0.25 nA

(c) STM -1.5 V 0.25 nA

(d) STM +1.5 V 0.25 nA

(e) STM -2 V 0.25 nA

(f) STM +2 V 0.25 nA
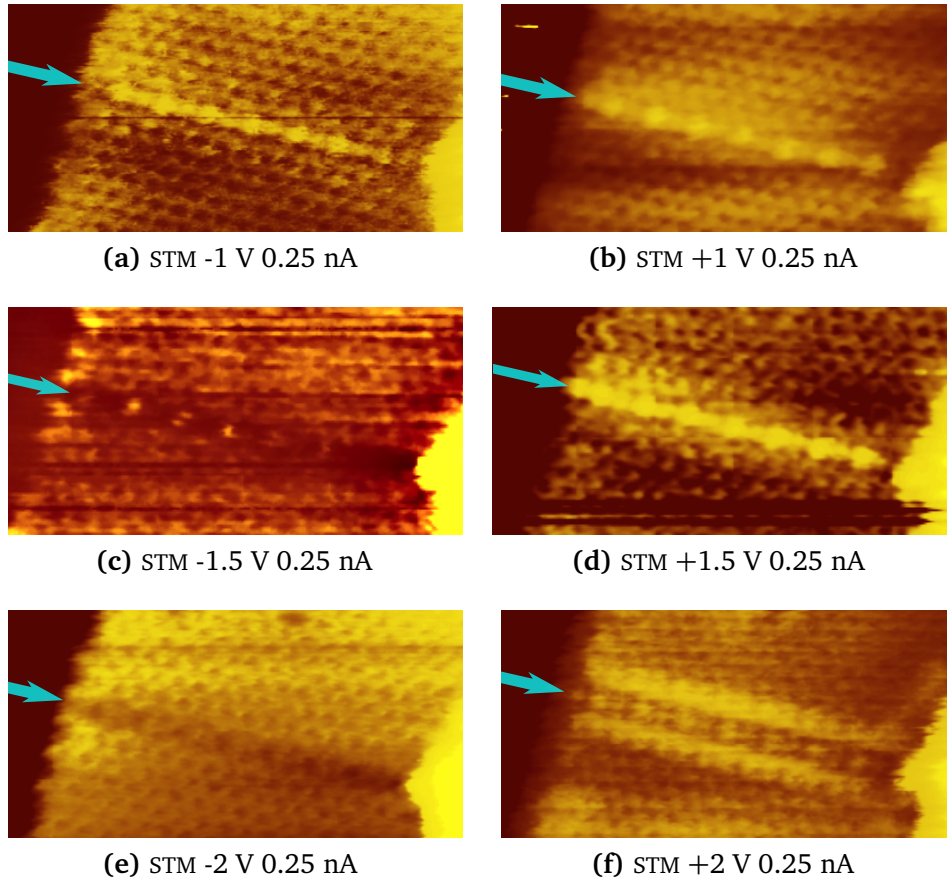
Figure 3.5: STM measurements of single domain wall. Each figure covers an area of 12 nm x 6 nm, allowing for direct comparison. In this measurement row the voltage varied, while the current was constant at 0.25 nA.

Comparing the measurements presented in Figure 3.4 and Figure 3.5, the similarity is clearly visible. Again, unlike the domain wall, the characteristic Ag $\sqrt{3} \times \sqrt{3}$ reconstruction does not change. In both experiments the -1.5 V setting (Figure 3.5c) results in a significant suppression of the domain wall intensity in comparison to the other applied voltages; +1 V (Figure 3.5b), -1 V (Figure 3.5a) and +1.5 V (Figure 3.5d), where the domain wall is pronounced and a elevation in apparent height is clearly visible. Bearing in mind that the increased current moves the tip closer to the sample, whereas the increased voltage moves it away, it seems that the change is not caused

by proximity (the character is similar in different current set points), but is clearly a voltage driven effect. The voltage dependence is supported by STM images taken also at 0.1 nA (see below).

An interesting effect becomes visible at at +2 V (Figure 3.5f). The suppression of the domain wall is accompanied by the appearance of significant embankment on both sides of the domain wall. In order to confirm this phenomenon, the extended measurement settings will be also included in next set and the discussion will be continued in next section.

Figure 3.6 shows set of STM images measured with 0.1 nA current setting. Similarly to the two previous series of measurements, the characteristic Ag $\sqrt{3} \times \sqrt{3}$ surface reconstruction changes not significantly in comparison to the domain wall with change of bias voltage. The domain wall is pronounced in the +1 V (Figure 3.6b) and +1.5 V (Figure 3.6d), whereas in -1.5 V (Figure 3.6c) the apparent height is suppressed, as in previous measurement sets.

The noteworthy domain wall character visible as a trench with embankment in Figure 3.5f with the bias setting of +2.0 V, is also visible in this measurement row in Figure 3.6f with the same bias voltage. In the remaining figures, domain wall remains suppressed, below the intensity level of the surrounding surface.

In the following the periodicity along the domain wall will be discussed. Linescans taken along the domain walls of each sub-figure in Figure 3.4 are shown in Figure 3.7. The relative changes of apparent form in relation with STM scan settings will be investigated.

The main hillocks (big black arrows) are equidistantly spaced from each other - every 1.3 nm, which is comparable to 2x0.665 nm - twice the corner hole distance of the Ag $\sqrt{3} \times \sqrt{3}$ reconstruction [TNO+88], [TN93]. Furthermore, small peaks (small grey arrows) are visible for negative bias setting, while for positive bias setting the peaks are significantly suppressed in comparison with large peak. A more detailed investigation of the peak separation shows that, although the separation of large peaks is 1.3 nm, the separation of small peaks is not equidistant. Each two neighbouring peaks create a pair, where the small peak is shifted towards a larger peak, thus changing the periodicity. Small peak is 0.55 nm away from its neighbouring large peak and 0.75 nm from another large peak, constituting together, as mentioned before, the period of 1.3 nm (double corner hole distance).

The peak-to-peak height of all domain walls was measured (according to dashed lines in Figure 3.7) and presented in Table 3.1.

(a) STM -1 V 0.1 nA

(b) STM +1 V 0.1 nA

(c) STM -1.5 V 0.1 nA

(d) STM +1.5 V 0.1 nA

(e) STM -2 V 0.1 nA

(f) STM +2 V 0.1 nA

(g) STM -2.5 V 0.1 nA

(h) STM +2.5 V 0.1 nA

Figure 3.6: STM measurements of single domain wall. Each figure covers an area of 12 nm x 6 nm, allowing for direct comparison. In the measurement row the voltage varied, while the current was constant at 0.1 nA.

The measurements with lower voltage show higher corrugation (average relative peak-to-peak height difference of domain wall chain, shown with dashed lines in
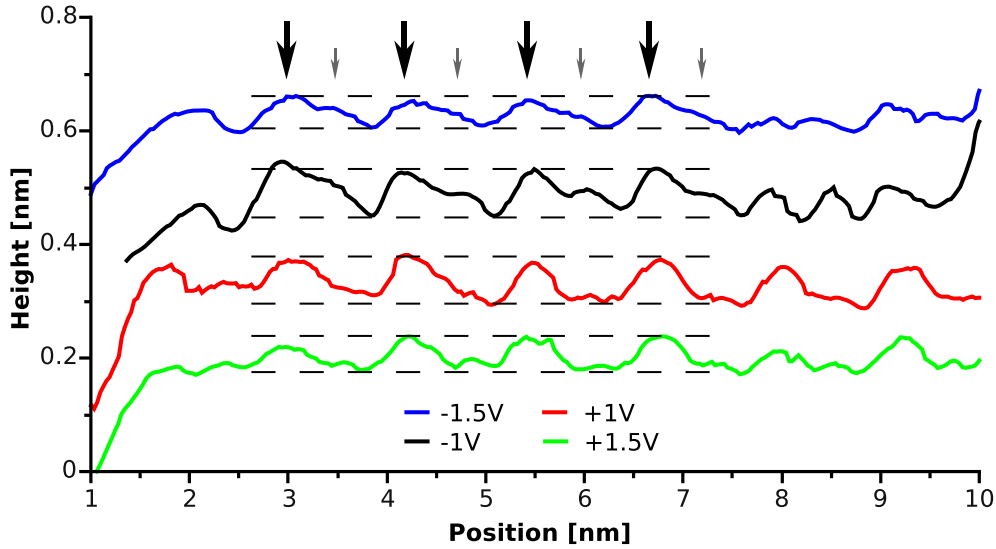
Figure 3.7: Linescans along domain wall in Figure 3.4. Each linescan represents relative height variation along the chain depending on bias voltage. The horizontal dashed lines show maxims and minims of each linescan, while black arrows are eye-guides for the peak positions.

Voltage	Corrugation
-1.5 V	0.046 nm
-1 V	0.078 nm
$+1$ V	0.076 nm
$+1.5$ V	0.054 nm

Table 3.1: Corrugation of domain walls from Figure 3.4, obtained from Figure 3.7. The corrugation is higher for lower bias voltages.

Figure 3.7). The data has been summarised in table Table 3.1.

From the model of the domain wall in Figure 3.3, a periodicity similar to the corner hole distance is expected, but the main peaks investigation determines the new periodicity, which is a doubled expected value and is a signature for a metallic 1D chain instability. The measurements were done at 80 K, so the system may show an instability of Peierls-type resulting in the doubling of periodicity for half-filled bands, while going from RT to LT. It is possible that the breaking of symmetry has similar character, as the temperature-driven transition from HCT to IET of Ag $\sqrt{3} \times \sqrt{3}$ structure. The following section deals with investigation of domain walls at RT and a direct comparison follows.

3.1.4 Domain walls - Room temperature

In this section the domain walls at RT will be investigated to allow a comparison with the LT measurements of the previous section. The priority is put on the measurement with the settings where the structure undergoes most significant change at LT.

(a) STM scan in RT at 1.75 V 0.25 nA

(b) STM scan in RT at 2 V 0.5 nA

(c) STM scan in RT at 3 V 0.25 nA
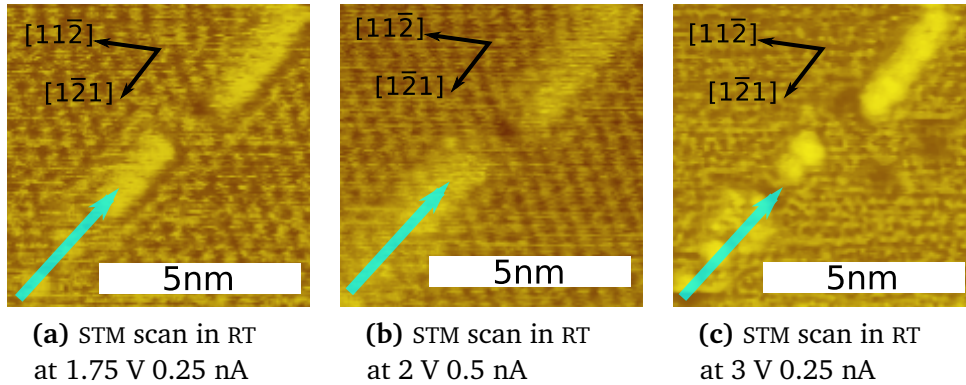
Figure 3.8: STM measurements of domain walls with different current and voltage setting at RT. No voltage- and current-induced change is noticed in this temperature range.

In Figure 3.8 a domain wall was measured with different voltage and current settings in order to compare it with the previous results obtained at LT. It is obvious that domain wall does not undergo any change in contrast to the LT experiment. Furthermore, the surrounding Ag $\sqrt{3} \times \sqrt{3}$ does not show any significant changes as well.

For detailed investigation, linescans along the domain wall were taken (in direction of blue arrow), as presented in Figure 3.9.

Equidistantly separated peaks of the similar height are visible. In Figure 3.9b the periodicity is observed to be 0.65 nm, which is close to Ag $\sqrt{3} \times \sqrt{3}$ corner hole distance. The observation corresponds with the model in Figure 3.3 in 3 Ag atoms within unit cell configuration, as the expected distance between peaks in the <112> direction is of corner hole distance range.

Concluding the experiment at RT and its comparison with results from LT, it is proven that the characteristic domain wall structure undergoes structural transition inducing a period change while cooling. Furthermore, no periodicity doubling or confinement effects are visible at the images taken in RT.

(a) STM scan in RT at 2 V 0.5 nA

(b) Linescan along the domain wall from the Figure 3.9a.
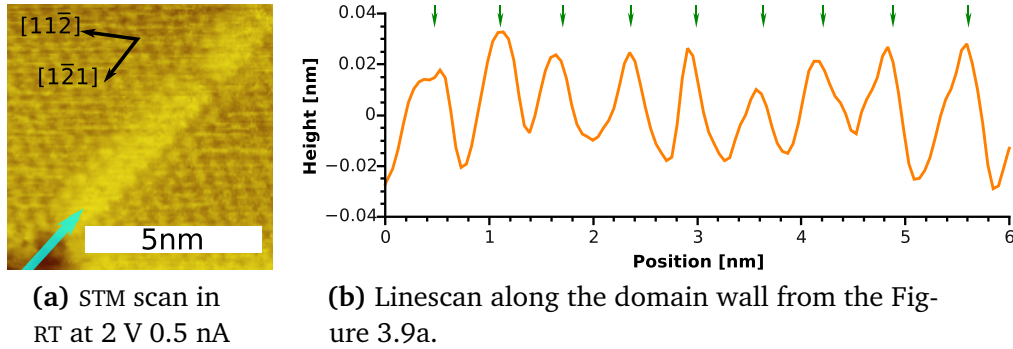
Figure 3.9: Line scans taken along domain wall presented in the Figure 3.9a. The average distance between peaks is 0.65 nm (single corner hole distance). The peaks positions are emphasized by blue arrows.

3.1.5 Peierls-like phase transition

Concluding the discussion of domain walls at RT and at LT it was found that the domain walls undergo a Peierls-like phase transition. Although a direct opening of a band gap within the already existing gap of Si cannot be measured by STM, the interpretation of the data is fully compatible with a Peierls-driven distortion, i.e. a metal–insulator transition due to an enhanced electron–phonon coupling along the chain, as sketched schematically in Figure 3.10 [Pei55]. Relying on this simple model, the doubling of the periodicity with respect to the Ag $\sqrt{3} \times \sqrt{3}$ reconstruction means that the surface bands are semi-filled, in qualitative agreement with the geometric model of the domain wall (see Figure 3.3). Assuming that the 1D system can be described also by a nearly free electron gas, similar to the 2D system [CGM+05], the doubling of the periodicity with respect to the Ag $\sqrt{3} \times \sqrt{3}$ reconstruction, corresponds to a Fermi vector $k_F = \pi/(2\sqrt{3}a) = 0.24$ for $a = 3.84$ Å, which implies an electron concentration of $n_{1D} = 2k_F/\pi = 1.5 \times 10^7 cm^{-1}$. The excess Ag atoms at the grain boundary should therefore be responsible for about 0.58 electrons per Si-site. It should be noted, however, that the perfect 1D scenario of the domain wall is only seen at low temperatures where the appearance of the signatures of the metallic 1D state is closely related to the confinement in the perpendicular direction. This more complicated situation invalidates the simple electron counting rules just applied, which require rigid bands. Therefore, quantitative deviations must be expected. On the other hand, confinement along the domain wall, as seen for instance for Cu wires of finite length

plays no role in our case [FHKP04].
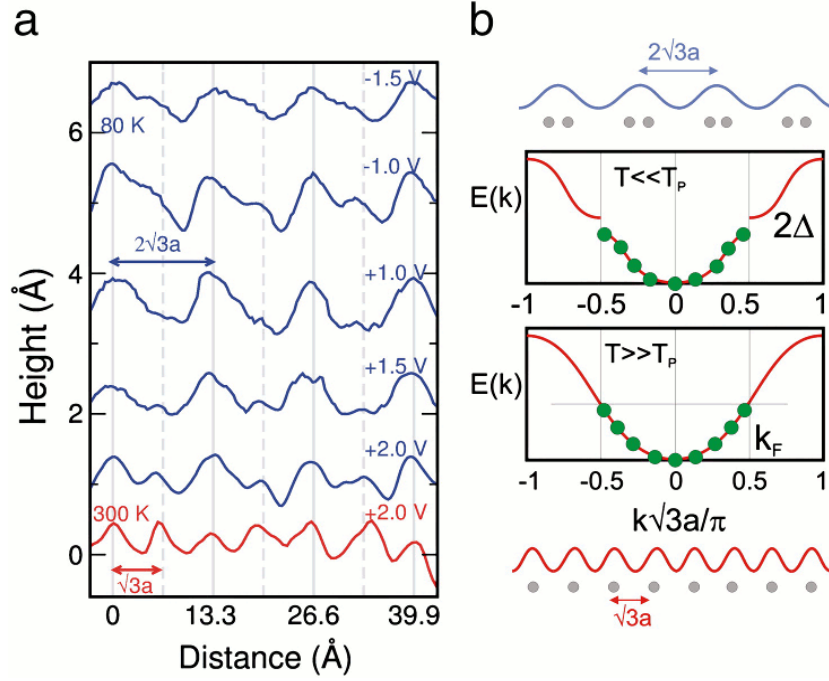
Figure 3.10: a) Line scans taken along the grain boundary. The scans are shifted for better visibility. In contrast to the measurement taken at 300 K, the line scans taken at 80 K reveal a twofold periodicity with respect to the Ag $\sqrt{3} \times \sqrt{3}$ reconstruction. This finding is not dependent on the bias voltage. b) Illustration of a Peierls-driven metal–insulator transition: Below transition temperature T_P the doubling within the chain is associated with a gap opening for half-filled bands. Above T_P the chain switches back into a metallic state [SPT11].

The intensity variation in STM as a function of bias voltage and temperature, mentioned above, occurs simultaneously in both directions. In contrast to the corrugation seen along the defect line, the corrugation is much larger in the direction across the domain wall, and depends sensitively on the bias voltages. As will be show in the following, this finding can be rationalised by a confinement of the 1D metallic chain structure in its perpendicular direction. A sequence of images of the domain wall for positive and negative bias conditions at a tunnelling current of 0.25 nA is shown in Figure 3.11a. Qualitatively, scans taken at 0.1 nA and at 0.5 nA tunnelling current show the same features, indicating that the spatial distribution of the intensity in the vicinity does not depend on the tip-sample distance. From line scans taken along the dashed lines shown in Figure 3.11a, which intersect a maximum in the chain structure, it is obvious that particularly for positive bias voltages the domain walls appear more

intense than the surrounding Ag $\sqrt{3} \times \sqrt{3}$ surface. The corrugation amplitude is more than 1 Å. While one maximum is seen at $+1$ V and $+1.5$ V, at $+2$ V even two maxima become apparent. At $+2.5$ V again the line defect is imaged as a trench. Generally, unoccupied states are spatially more extended. Therefore, effects of confinement can be observed more easily with these states.
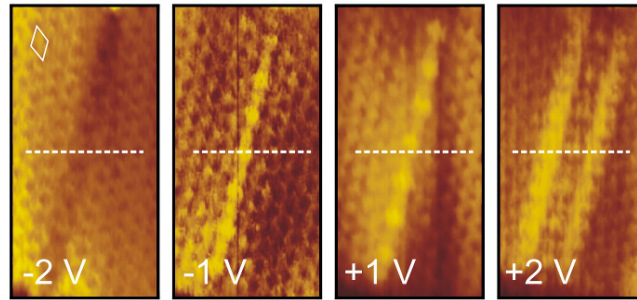
(a) Sequence of STM images (12x6 nm^2) for different bias voltages. STM images were taken at T=80 K, I=0.25 nA.
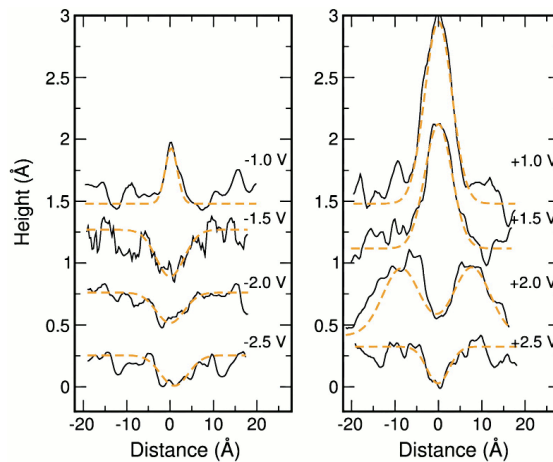
(b) The dashed lines are guides to the eye in order to elucidate the bias dependent intensity modulation with respect to the Ag $\sqrt{3} \times \sqrt{3}$ reconstruction.

Figure 3.11: A sequence of images of the domain wall for positive and negative bias conditions at a tunnelling current of 0.25 nA [SPT11].

The line scans were taken in constant current mode. Consequently, the intensity reflects only indirectly the density of states. Although dI/dV measurements with high bias resolution have not been performed, it turns out that the intensity variation can

be explained by the confinement of the electron gas and formation of electronic sub-bands, in analogy to Pt/Ge(100) [OHH+05] [HOPZ06], e.g. if we identify the large single peak at +1 V and the double peak structure at +2 V with resonances of the n=1 and n=2 states, we obtain within the model of a parabolic (infinitely high) potential well an effective width of the well to be around 1 nm. This matches qualitatively with the width of the trench. Of course this is only a rough estimate, but it rationalises the pronounced variation of the intensity distribution. For a quantitative treatment of the quantum well states (QWS) high resolution dI/dV mappings are necessary.

QWS of higher order have not been found. These states are obviously not any more confined by the potential of the domain wall. However, the energy of the n=2 state is, despite its comparatively high energy, still confined, although the unoccupied states of the domain boundary are in resonance with those of the Ag $\sqrt{3} \times \sqrt{3}$ structure. It is important to note that confinement with clear resonances takes place only in the low-temperature Peierls state, similarly to Pt chains on Ge(100) [OHH+05] [HOPZ06], whereas at room temperature no resonances are observed, but only an increased intensity at the domain wall, reflecting the higher DOS within the domain wall. This first of all implies that the rigid band model shown in Figure 3.10b is too simple, since localisation in the low-temperature phase can only be explained by a shift of bands and/or a change in symmetry of the wave functions involved. Apparently, only within the Peierls state of the chain, the confinement effect is enabled since the 1D bands cannot hybridise with the band structure of the Ag $\sqrt{3} \times \sqrt{3}$ reconstruction.

3.2 FDT molecule on Ag $\sqrt{3} \times \sqrt{3}$

In this section, results of the FDT deposition experiment will be discussed. The section is divided into two parts, concerning the two different adsorption places of the molecule found. In the paper by C.Tegenkamp, J.Schmeidel and H.Pfnür [TSP10], the FDT bonding to defects and surfaces is discussed. The following sections are widely based on this paper, entitled "Chemisorption of ferrocene on Si(111)-Ag $\sqrt{3} \times \sqrt{3}$: frustrated conformational flexibility".

In the first subsection of this section, the FDT molecules bond to the defects will be described. In next subsection the adsorption on flat and perfect Ag $\sqrt{3} \times \sqrt{3}$ will be discussed, followed by first results obtained by simulation. Molecules on domain walls will be investigated at the end.

(a) FDT deposited on Ag $\sqrt{3} \times \sqrt{3}$. domain walls and flat surface. STM 3 V 0.25 nA

(b) FDT deposited on Ag $\sqrt{3} \times \sqrt{3}$. Flat surface. STM 3 V 0.25 nA
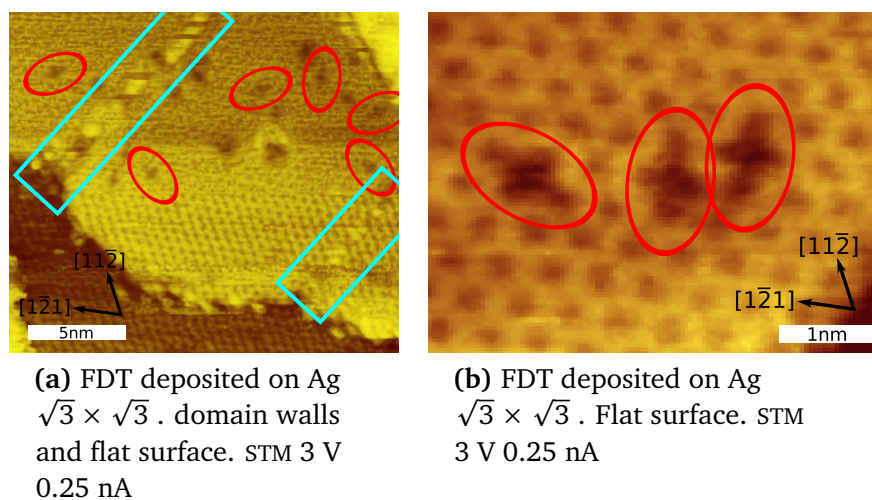
Figure 3.12: Due to deposition of FDT on Ag $\sqrt{3} \times \sqrt{3}$, two effects occur. On flat surface, a cross-shaped suppressions can be observed (emphasised by red rings), whereas the high intensity at the positions of the domain wall is suppressed (blue rectangles).

Details of Si(111) Ag $\sqrt{3} \times \sqrt{3}$ domain walls were presented in the previous parts. The experiment shown here were conducted at 300 K. The domain wall landscape was created according to the default procedure described in chapter 2. After preparation of the Ag $\sqrt{3} \times \sqrt{3}$, FDT molecules were evaporated on the surface using a Knudsen cell.

3.2.1 Ferrocene bonding to defects

In Figure 3.13 a STM image taken at $+2$ V bias is presented. STM imaging of the same area during evaporation, direct comparison and impact of adsorbed FDT on Ag $\sqrt{3} \times \sqrt{3}$ is possible. Figure 3.13 presents characteristic changes of the surface.

At the clean surface Figure 3.13a one can identify steps, chain defect structures - domain walls (marked by a rectangle) and a point defect (marked by a circle) in the centre of the upper terrace. As discussed in previous parts, the domain walls go along the <112> direction and at RT they are always brighter than the terraces at these tunnelling conditions. Here the apparent height of domain wall is ~120 pm. The point defects are also bright and undergo significant change during deposition of molecules. The change of the electronic contrast in the STM images directly shows the adsorption process. The adsorption is preferred on the defects positions, whereas

(a) Clean Ag $\sqrt{3} \times \sqrt{3}$ surface before deposition.

(b) Ag $\sqrt{3} \times \sqrt{3}$ surface after 15 min.

(c) Ag $\sqrt{3} \times \sqrt{3}$ surface after 30 min.
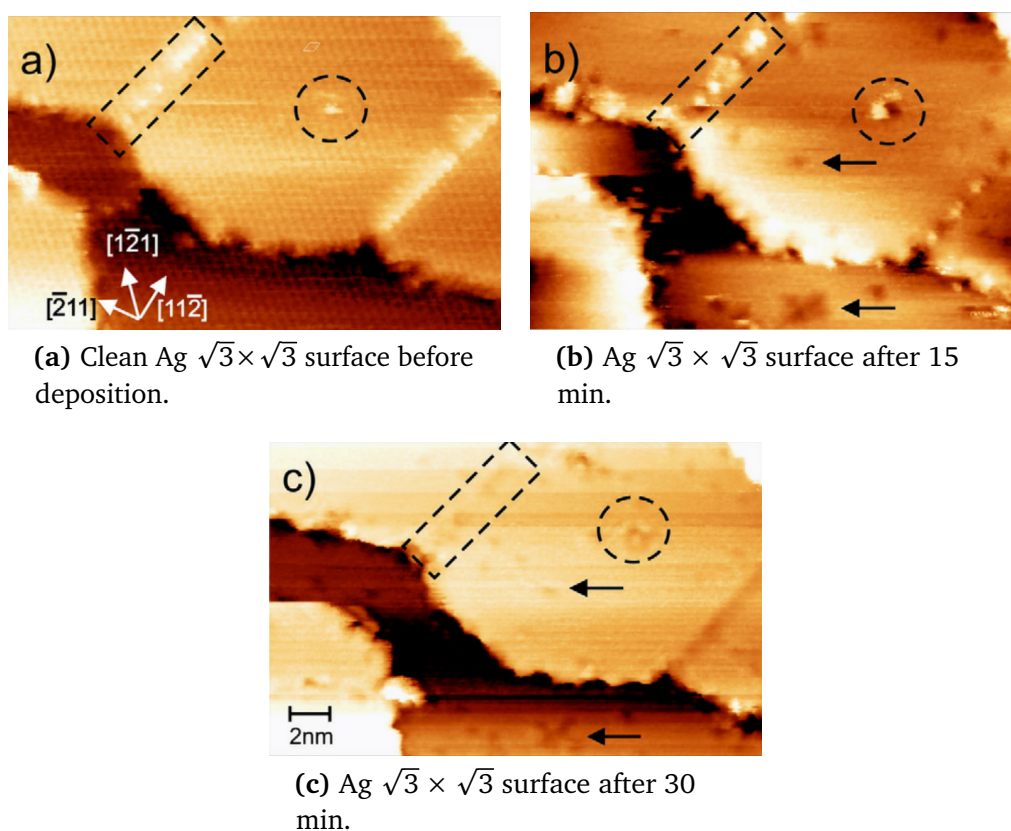
Figure 3.13: The STM images taken during evaporation of FDT at RT at $+2$ V and 0.25 nA of size 25x16 nm². The preferred adsorption positions, which changed contrast from bright to dark during deposition, were found at defects sites, that is at domain walls (emphasised by rectangle) and point defects (emphasised by circle). Adsorption of FDT on flat terraces (shown with arrows) will be discussed in following parts [TSP10].

adsorption of molecules on surface, at perfect terrace sites, was observed to occur less frequently.

The apparent height of defects change due to adsorption of FDT. The $\sim$120 pm high protrusions become depressions with a relative depth of $\sim$40 pm, what is visible on the Figure 3.13b and Figure 3.13c. Furthermore, the partial saturation of the domain wall in Figure 3.13b change to full saturation and darkening in Figure 3.13c. After full saturation of the line defect, also adsorption on flat Ag $\sqrt{3} \times \sqrt{3}$ terraces takes place. The arrows in Figure 3.13 mark the positions where this can be identified. All of this depressions have a very characteristic cross-shaped form, which will be discussed in more details in the next part.

As obtained by VASP (Vienna Ab-initio Simulation Package) calculations the Cp–Fe–Cp axis is oriented parallel to the surface due to the position and form of the Ag-S bonds [MBTP06] [Mey06] [BTP+08]. Stable imaging of these signatures at RT and high tunnelling currents suggests that the FDT creates, as expected, strong bonds to the surface. The preferential adsorption at defect sites is in qualitative agreement with calculations, which were done for different molecule configurations and orientations on the Ag(111) surface.

The binding energy is calculated to be 2.4 eV on the perfect and flat surface and the thiolate bonded FDT with a Cp–Fe–Cp axis parallel to the surface is energetically favoured, furthermore at step sites the binding energy is 0.6 eV higher. The bridge and hollow positions are favoured on (111) surface, the molecule is bound with both S-atoms and the molecules Cp-rings are slightly tilted against each other. Still, the defects, due to existence of unsaturated bonds, promote a stronger binding.

It turns out, that conclusion from calculations of FDT adsorption on Ag(111) crystal are qualitatively valid also for the adsorption on Ag $\sqrt{3} \times \sqrt{3}$ surface. Focusing on the adsorption on defects, depression in STM imaging is visible, that is, an relative reduction of tunnelling rate. In the constant current mode at high tunnelling voltages the depression is in the order of 40 pm. The tunnelling electrons flow directly into unoccupied Ag/Si surface states, because in the electronic structure of the molecule there are no molecule specific orbitals in used bias regime, as can be seen in Figure 3.12 obtained with bias +3 V and Figure 3.13 with bias +2 V. The molecule acts as dielectric medium, characterised by higher dielectric constant than vacuum. The suppressed electric field in the medium leads to a reduction of the tunnelling current, which in STM image is visible as a depression, that is, a decrease in the tunnelling distance. For the flat Ag $\sqrt{3} \times \sqrt{3}$ structure, the origin of the protrusions will be discussed in following section.

3.2.2 Ferrocene on flat terraces

The characteristic cross-shaped structure found on the terraces is presented in Figure 3.14. As mentioned in the previous section, these structures, with an inner fine structure can be related to the chemisorbed FDT molecule. Furthermore, this statement is supported by the calculations on bulk Ag(111) [MBTP06] [Mey06] [BTP+08].

In order to discuss the cross-shaped depressions on the flat terraces it is important to consider the perfect Ag $\sqrt{3} \times \sqrt{3}$ surface (see subsection 2.2.2). The "corner holes"

on the Ag $\sqrt{3} \times \sqrt{3}$ surface, which are the position of Si trimers, create a perfect hexagonal array. According to this hexagonal matrix, an exact adsorption position can be determined. It is obvious, that the influence of cross-shaped structures, visible as the protrusions in STM, is local, as the surrounding show the Ag $\sqrt{3} \times \sqrt{3}$ characteristic surface.
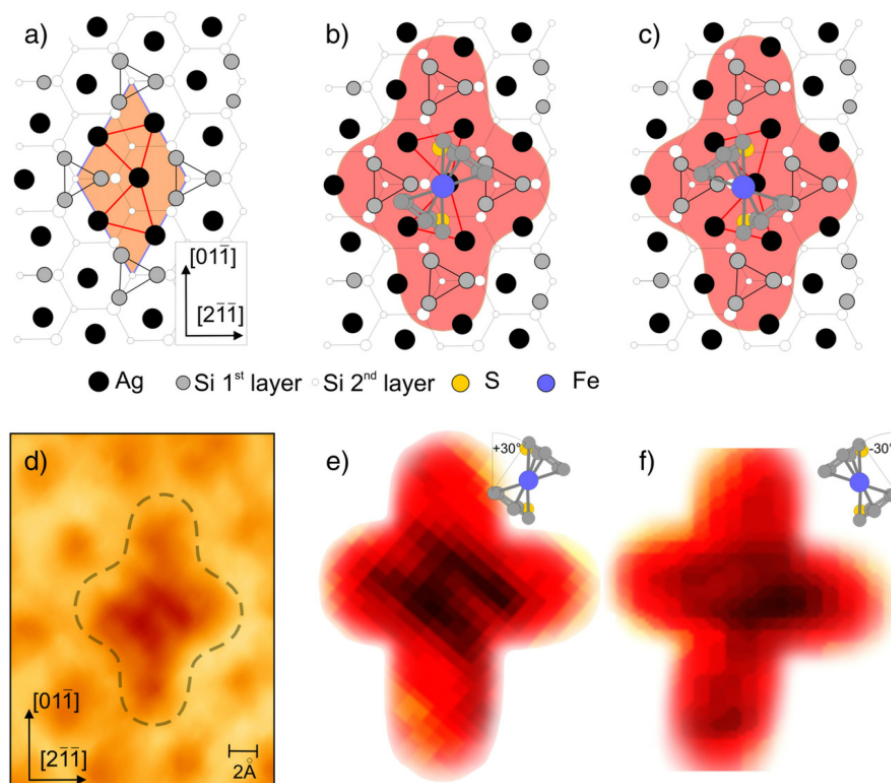
Figure 3.14: The figures (a-c) show the structural model. The figures (d–f) show STM images (+3 V, 0.25 nA, RT). Figure (a) is the clean Ag $\sqrt{3} \times \sqrt{3}$ surface, Figure (d) show a single cross structure. Figure (b) and (c) show the structural model of the deposited FDT molecule, according to the STM measurements shown in Figures (e) and (f). The Ag trimers in the HCT model are marked by red lines. The background subtraction reveals two different orientations of the ferrocene with respect to the unit cell (see Figures (e) and (f)) [TSP10].

The two arms of the investigated cross structure coincide with the unit cell of the Ag reconstruction (Figure 3.14d). The short axis of the cross structure (0.67 nm long) is aligned along the Ag $\sqrt{3} \times \sqrt{3}$ corner hole directions (<112> family), while the long arm (1.2 nm long) is rotated by 90°. The observed structure is much larger than the size of the FDT molecule and does not directly correspond to the form of

the molecule. It is calculated that the distance between the thiol groups in the FDT molecule is between 0.37-0.44 nm and as such does not correspond to the size of the cross structure, furthermore is even smaller than the Ag $\sqrt{3} \times \sqrt{3}$ unit cell (which is 0.665 nm [TNO+88]).

The adsorption of molecules reduces the tunnelling probability in between the corner holes of the clean Ag $\sqrt{3} \times \sqrt{3}$ structure. Therefore the model that the FDT molecule is located in the centre of Ag trimer is supported (as shown in Figure 3.14 (b) and (c)). This configuration further states that both thiolate bonds are located in the Ag trimer area. The adsorption configuration is almost the same as the one obtained from simulation of adsorption on Ag(111). The proposed adsorption model is highly probable due to the flexibility of the molecule and the ability to vary the distance between the thiol groups between 0.33-0.41 nm, by rotation and tilting of the Cp rings with respect to each other.

Careful subtraction of the background reveals a substructure in this region. The submolecular resolution gives access to the relative adsorption geometry of the FDT. Two dark parallel lines at a distance of about 0.3 nm and rotated by 30° with respect to the long axis are visible. Those lines can be identified as the Cp-rings of the ferrocene, even though this distance is smaller than the distance between the Cp-rings measured in the gas phase FDT of 0.37 nm. Nevertheless, it can be stated that the adsorption configuration with the Cp–Fe–Cp axis oriented parallel to the surface is supported.

Only two different configurations of the Cp-ring orientations were found in the FDT induced cross-shaped objects, aligned by +30° or -30° with respect to the long axis. From this it can be stated that, due to defined local bonding positions, the rotational flexibility is limited and two found configurations are energetically favoured. Finally, the depressions visible in STM images of unoccupied surface states must have a twofold origin: the polarisability of the molecule in energy ranges where no molecular electronic states exist and adsorption induced change of the unoccupied DOS at the surface [MBTP06] [Mey06]. The inner region of the structure corresponds to the central part of the molecule, while the outer region is caused by chemisorption and following reduction of electronic density of states surrounding the thiolate bond. These conclusions are supported by the simulation results presented in the next section.

3.2.3 Simulation of adsorption on flat Ag $\sqrt{3} \times \sqrt{3}$ surface

The model proposed in the previous section has been also simulated as described in section 2.5; structural relaxation simulation of FDT over Ag $\sqrt{3} \times \sqrt{3}$ surface was conducted. As substrate for this simulation the previously relaxed Si(111)/Ag $\sqrt{3} \times \sqrt{3}$ surface was used. As known from simulation of FDT on Ag(111) crystal, the fcc (between three neighbouring surface Ag atoms) is the most energetic favourable position for S-Ag bond [MBTP06]. This assumption was also considered while intro-

(a) The top view of FDT adsorbed on Ag $\sqrt{3} \times \sqrt{3}$ surface.

(b) The side view of FDT adsorbed on Ag $\sqrt{3} \times \sqrt{3}$ surface.

(c) The calculated STM image, based on the simulation of adsorption. The blue outline depicts the cross-shaped structure discussed in subsection 3.2.2.
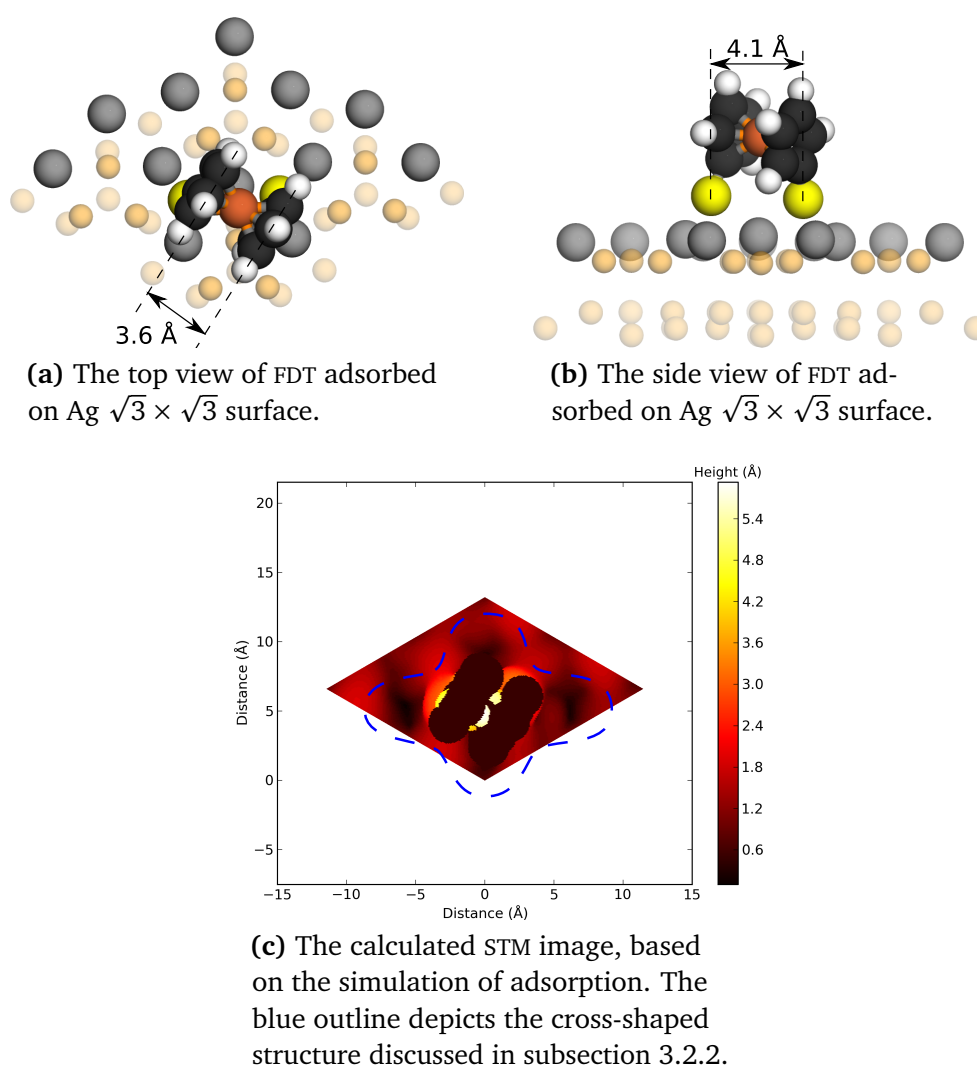
Figure 3.15: Simulation of structural relaxation of the FDT adsorbed on the Ag $\sqrt{3} \times \sqrt{3}$ surface. Four Ag $\sqrt{3} \times \sqrt{3}$ unit cells are visible in the Figures. **Model and simulation by Courtesy of Wei Chen.**

ducing the explanation for the appearance of cross-shaped objects. From simulation shown in Figure 3.15 it is clear that the most optimal position for adsorption is, as expected, in between four Ag corner holes, at the Ag trimers. Figure 3.15c shows the calculated STM picture of the adsorbed FDT molecule on the Ag $\sqrt{3} \times \sqrt{3}$ surface.

The distance between Cp-rings is 0.36 nm and the distance between S atoms is 0.41 nm, whereas the rings are tilted with respect to each other by only 0.7°. These values correspond with the values obtained for simulation of adsorption Ag(111) crystal and support the assumption, that the molecule is adsorbed in almost undisturbed configuration. Furthermore, the Cp-rings are rotated with respect to the S groups by around 48°, what is in agreement with simulation of the molecule in gas phase, predicting one of the molecules local energetic minimum for similar angles [Mey06].

According to the relaxation simulation, the fcc adsorption position for single Ag-S bond is found to have the lowest energy, thus the rotation of molecule and Cp rings leads to the fcc position of both thiolate bonds [MBTP06] [Mey06]. From simulation it was not observed that the molecules would adsorb in the Ag $\sqrt{3} \times \sqrt{3}$ corner hole.

Here, only one from two proposed molecular conformations were obtained. This orientation seems to be the energetically favourable, whereas the other one is metastable structure, but stable enough to be measured in RT.

3.2.4 Suppression of domain walls

Figure 3.16 shows the process of destruction of domain wall chain during evaporation of FDT molecules at RT. The overview in Figure 3.16a shows the area where the experiment was carried out. The Ag $\sqrt{3} \times \sqrt{3}$ surface is of high quality, with a few characteristic defects. The set of images shows a surface with increasing amount of adsorbed molecules. Sample surface was imaged and the changes were observed during deposition of molecules. In order to obtain stable and optimised image the source was switched off or the evaporator shutter was closed. Further evaporation of molecules, after the stage shown in Figure Figure 3.16d, leads to full saturation of the surface with molecules, thus no further investigation of adsorption positions is possible and the sample needs to be prepared again.

By STM it was observed that characteristic objects appear and that the domain walls undergo significant change on the Ag $\sqrt{3} \times \sqrt{3}$ surface. Both changes are related to the FDT molecules adsorption.

For a detailed investigation, linescans along the domain walls at different deposition

(a) Area overview. STM 2V 0.25 nA

(b) Before FDT evaporation. STM 2 V 0.5 nA, t=0 min

(c) During FDT evaporation. STM 3 V 0.25 nA, t=15 min

(d) After FDT evaporation. STM 3 V 0.25 nA, t=25 min
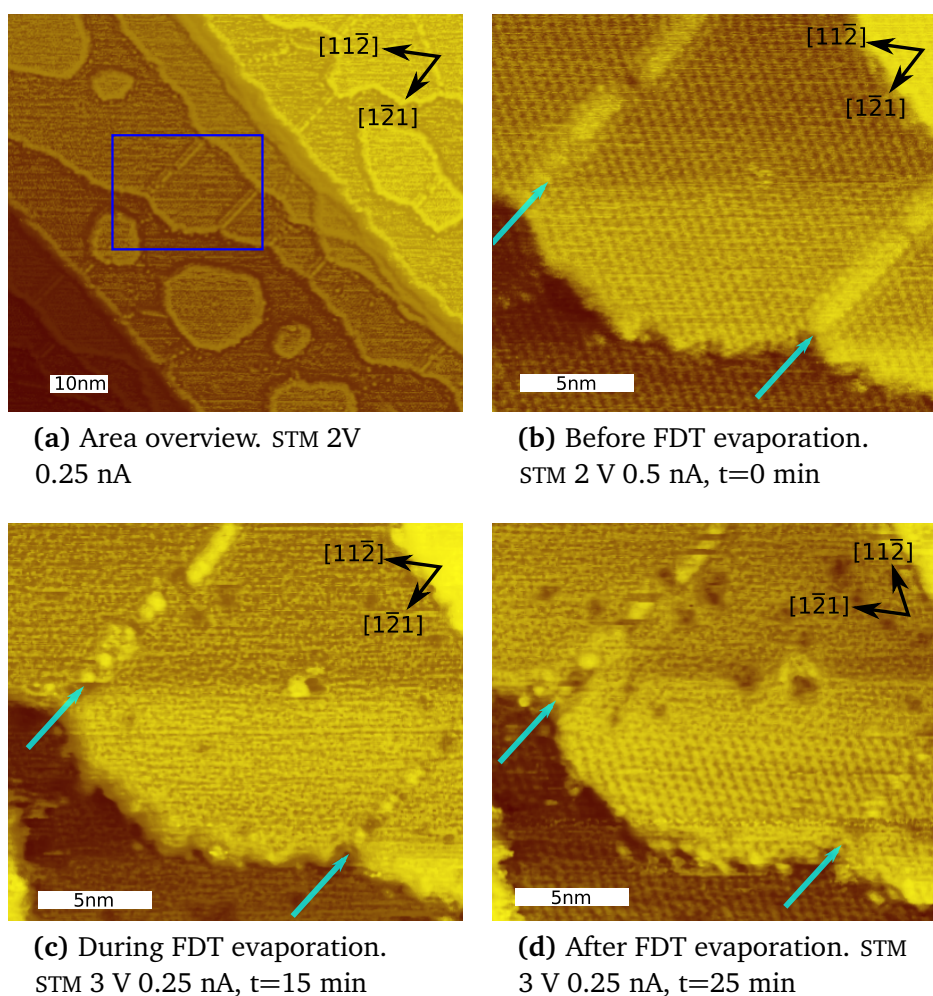
Figure 3.16: STM measurements of adsorption induced change in domain walls. Change in measurement settings was conditioned by measurement stability. Influence of this variation on the image was constantly observed and no change was noticed. Images a) and b) were taken before deposition. Image c) was taken after 15 min and image d) after 25 min of deposition.

stages were put on one figure, to emphasise the changes during adsorption. Linescans of domain wall on the left (3.17)and on the right (3.18) are presented separately. In both figures below, a change in domain wall chain is clearly visible. Even in low quality of the chain in Figure 3.17, a significant change is visible.

While investigating the structure it has been found that the chain on the left side of Figure 3.17 has a periodicity of 1.3 nm, whereas the chain on right side reveals a 0.65 nm spacing. The change is significant, but due to not optimal periodicity of
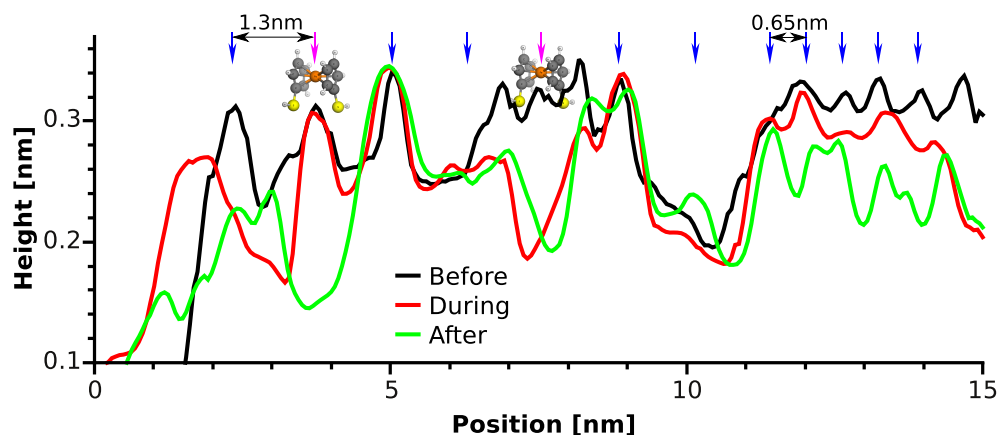
Figure 3.17: Line scans along domain wall on the left part of the image. The average distance between peaks on the left side of the Figure is 1.3 nm (doubled corner hole distance), whereas average distance on the right side is 0.65 nm. The peaks positions are marked by blue arrows (some arrows show expected peak positions). Pink arrows label the peaks which have undergone significant suppression. The quality of domain wall chain is not optimal.

chain, a further quantitative investigation is difficult.

The high quality domain wall chain on the right side of the investigated image is much more appropriate for a discussion. The corresponding linescans are presented in Figure 3.18.

The long chain has equal peak spacing and the height variation is relatively small. In Figure 3.18 the average periodicity is 0.65 nm and it is similar for all peaks. This corresponds directly with the exact value of corner hole distance on Ag $\sqrt{3} \times \sqrt{3}$.

In Figure 3.18 the three stages of molecules deposition are drawn with different colours. It can be directly observed, that during deposition, every two out of three peaks are suppressed. The average distance between peaks is 0.65 nm and the value is in the same order of magnitude as the FDT molecule size. The FDT molecule is very flexible due to its changeable configuration. Considering the relative small size of the molecule, it is more probable that the single Ag atom separation occurs due to electronic than to steric reason. Furthermore, such separation could be explained in terms of lowered chemical activity near to suppressed domain wall defect or by the repulsive charge of bounded molecule. Still, a detailed discussion should be supported by appropriate simulations.

On the one hand, just by changing the angle between cyclopentadienyl ring groups the distance between sulphur atoms varies between 0.37 nm and 0.44 nm [MBTP06]
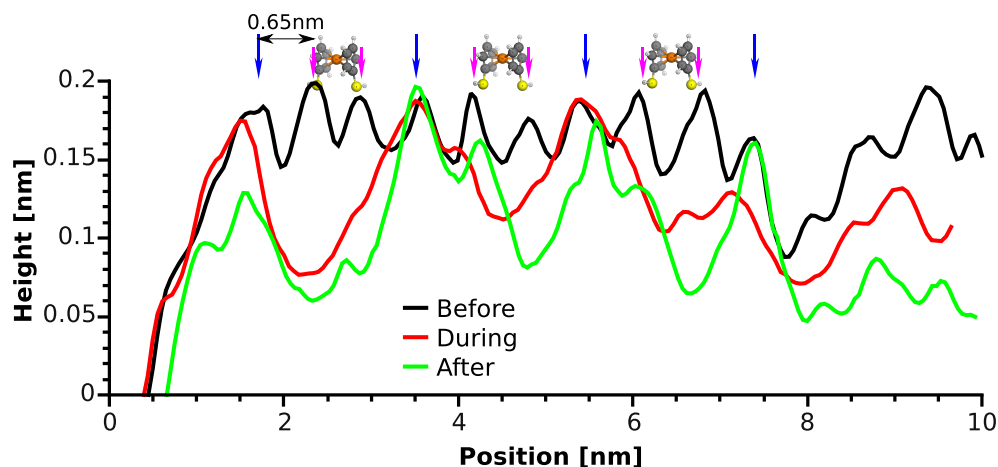
Figure 3.18: Line scans along domain wall on the right part of Figure 3.16. The average distance between peaks is 0.65 nm (single corner hole distance). The peak positions are marked by blue arrows (some arrows show expected peak positions). Pink arrows label the peaks which have been suppressed during deposition of molecules.

[Mey06] [BTP+08]. On the other hand, by rotation of the rings, the distance can be as long as 0.66 nm, which coincides nicely with the distance between domain wall peaks of 0.65 nm.

3.3 Mesoscopic effects in nano-sized silver islands

In order to investigate the influence of the wetting layer on electronic characteristics of nano-structures, the STS measurements were prepared. In particular, small Ag-clusters on Ag $\sqrt{3} \times \sqrt{3}$ interface have been used for this study, which is important for molecular electronics.

The electronic structure was measured by means of STM in STS mode [SPT09]. The amount of deposited material and the method of deposition is found to have a significant influence on electronic structure. The following sections are widely based on paper by J.Schmeidel, H.Pfnür and C.Tegenkamp, "Coulomb blockade in Ag/Si(111): The role of the wetting layer" [SPT09].

3.3.1 Si(111) and Ag $\sqrt{3} \times \sqrt{3}$ surface structures

The structures were prepared according to the recipes described in chapter 2. The clean Si(111) 7x7 reconstruction (shown in Figure 3.19a), reveals the characteristic
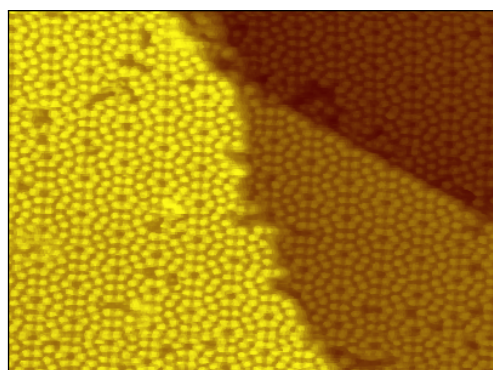
(a) Si(111) 7x7 clean surface.
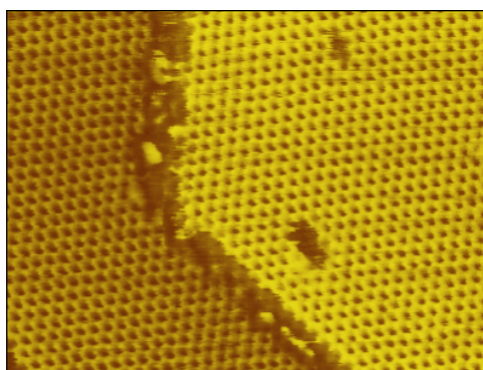
(b) Si(111) Ag $\sqrt{3} \times \sqrt{3}$ reconstructed surface.
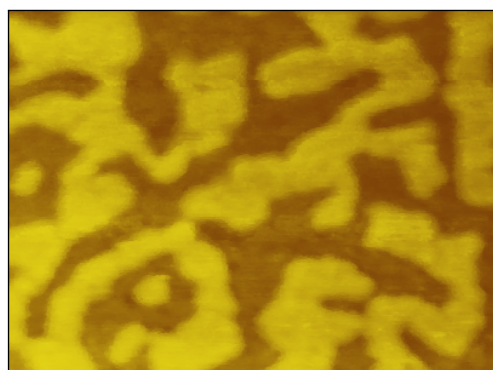
(c) Si(111) 7x7 with ∼1 ML Ag, not annealed.
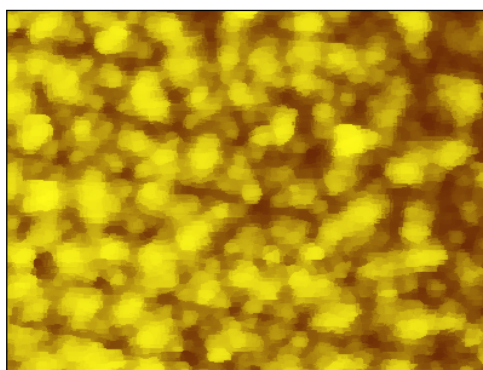
(d) Si(111) 7x7 with submonolayer amount of Ag, not annealed.
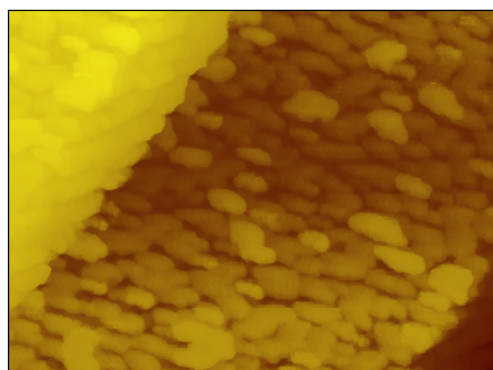
(e) Si(111) 7x7 with multilayer Ag clusters, not annealed.
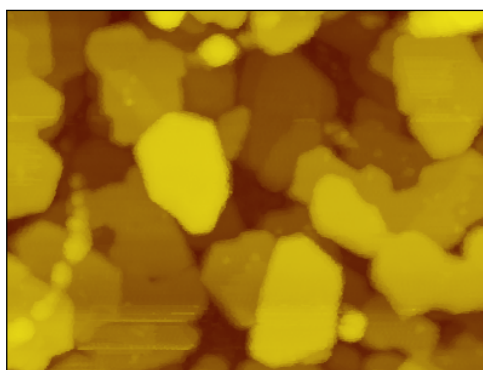
(f) Si(111) Ag $\sqrt{3} \times \sqrt{3}$ with multilayer Ag clusters, annealed.

Figure 3.19: Systems prepared for investigating the electrical behaviour. Different phenomena observed in STM/STS measurements will be discussed [SPT09].

gap in local spectroscopy as shown in Figure 3.21. The occupied S1 and S2 states within the gap at negative bias voltages are visible. These surface states occur due to different re-bonding configurations of adatoms and rest atoms.

The most significant is the unoccupied surface state around +0.7 V, the hallmark of Si(111) 7x7 reconstruction, which is in good agreement with other experiments [Nor86] [HTD86] [LHK+94] [CH80] [Ven94]. The chemical potential is different at the surface and in the n-type doped Si bulk, therefore band bending occurs. The Schottky barrier (SB) is found to be around 0.5 eV, as judged from the symmetry of the band structure with respect to zero bias.

(a) The energy diagram of the metal/semiconductor.

(b) An equivalent circuit of system of (a).
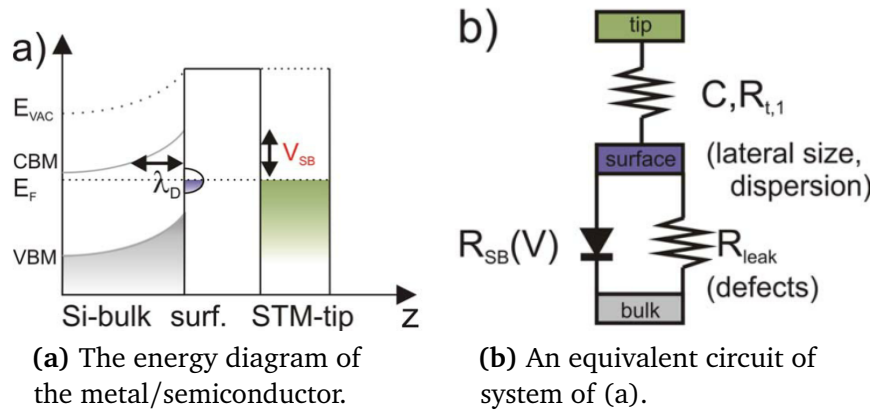
Figure 3.20: Electronic landscape of surface. The energy diagram of the metal/semiconductor heterojunction at zero bias including the Schottky barrier (SB) and the tunnelling barrier (TB) between STM tip and metal island [SPT09].

It will be shown that the Schottky barrier (SB) at the interface and the tunnelling barrier (TB) at the vacuum side represents single or double tunnelling barriers, respectively, which can be controlled by modifying the interface.

The Debye length in our low-doped samples is on the order of 100 nm, therefore electron transport on the surface normal is controlled by thermal excitation rather than by electron tunnelling. Normal to the surface transport can occur only via hopping along defect sites giving rise to a parasitic current pathway denoted by R_{leak} in Figure 3.20. As the ohmic contacts to the sample (surface) cannot be assured, R_{leak} is the standard pathway for electrons. From the dopant concentration a defect concentration of the order of 10^{12} cm^2, can be deduced, i.e., one defect state per 30^2 lattice constants.

The surface states have to provide a sufficiently high electron mobility within

the surface plane, in order to effectively transport charges to these channels. If the sufficient mobility is not provided, local charging occurs. Hence, for any (semi)metallic structure on semiconducting substrate, the lateral transport properties, that is the 2D dispersing bands are crucial for local spectroscopy as well.

(a) STM image of clean Si(111) 7x7 surface reconstruction (30x30 nm^2, +2 V, 0.5 nA).

(b) STM image of clean Ag $\sqrt{3} \times \sqrt{3}$ surface reconstruction (300x300 nm^2, +2 V, 0.5 nA).

(c) STS spectra taken on both surfaces. The dashed lines present the bandgap of Si(111) without surface states.
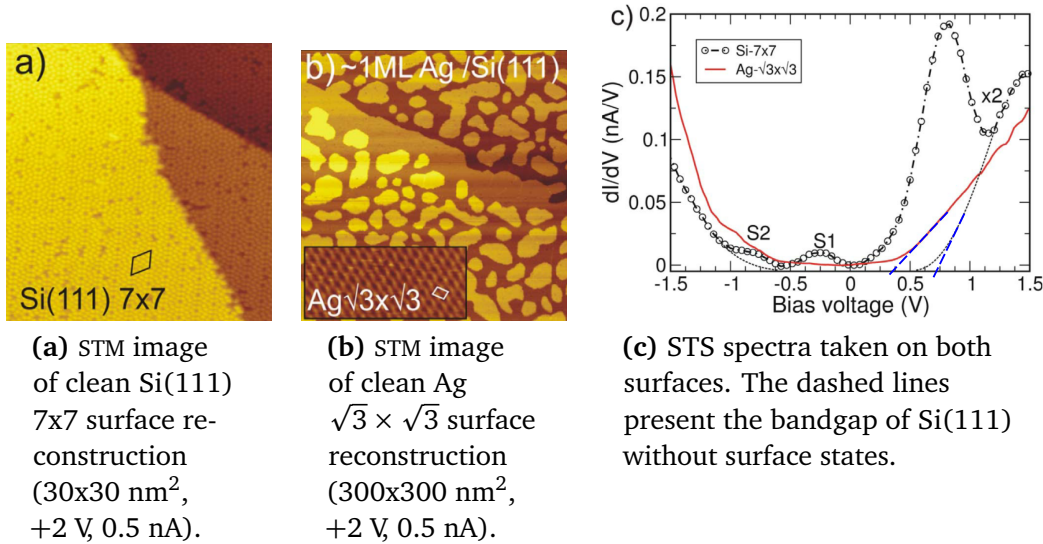
Figure 3.21: STM images of clean Si(111) and Ag $\sqrt{3} \times \sqrt{3}$ surfaces and respective STS measurement of both surfaces. Inset in (b): Ag islands (size 7.4x3.2 nm^2, +1 V, 0.4 nA) [SPT09].

The characteristic Ag $\sqrt{3} \times \sqrt{3}$ interface structure is created by deposition of 1 ML of Ag, followed by annealing to 800 K for several minutes (for details see chapter 2). Clean Si(111) and homogeneous Ag $\sqrt{3} \times \sqrt{3}$ surfaces are shown in Figure 3.21. Upon to Ag-Si bond formation, the exchange of Si atoms leads to the formation of a characteristic roughness on a formerly atomically flat Si(111) terraces as shown in Figure 3.21. The surface states of the clean Si surface are suppressed by Ag $\sqrt{3} \times \sqrt{3}$ reconstruction, as shown at the dI/dV curve in Figure 3.21. The overall conductance is increased slightly relative to the Si(111) surface and the well ordered Ag $\sqrt{3} \times \sqrt{3}$ surface consists of a low density of states around the Fermi level.

The 1 ML Ag adsorbed at the Si(111) surface, enlarges the SB by 0.3 eV, as seen by angle resolved photo emission spectroscopy measurement (ARPES) [CGM+05] and as demonstrated by the asymmetry of the dI/dV with respect to zero bias (see Figure 3.21c). The extrapolation of the bulk band edges at positive bias in Figure 3.21c (blue lines) shows that the band bending is increased for the Ag $\sqrt{3} \times \sqrt{3}$ phase

compared to the clean surface. The ARPES measurement reveals that the perfect wetting layer is only half-metallic, that is, there is no band gap and the occupied states barely touch the Fermi surface. The two-dimensional electron gas (2DEG) is first formed by electrons originating from excess Ag coverage that fill previously unoccupied electronic states, as shown in the Figure 3.22.
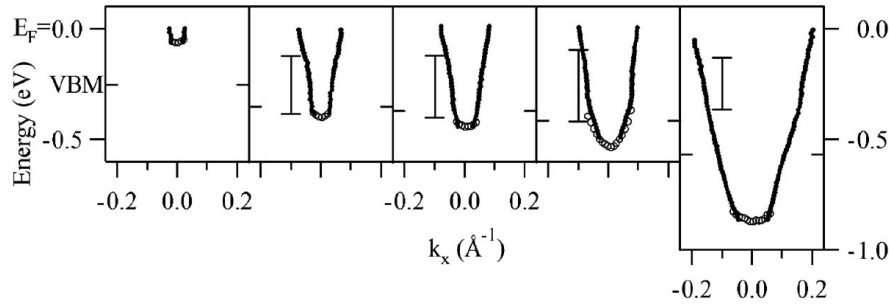
Figure 3.22: Dispersion curves for Ag $\sqrt{3} \times \sqrt{3}$ surfaces doped by various amounts of excess Ag; 0.0015, 0.012, 0.015, 0.022, and 0.086 extra electrons per Si(111) 1x1 unit cell. Band dispersions fitted from ARPES measurement. The energy scale is relative to the Fermi level, whereas the valence-band maxims are indicated by horizontal tick marks. Figures by Crain et al. [CGM+05].

Although the SB is slightly reduced by the additional Ag amount, the V_{SB} remains $\geqslant 0.5$ eV, that is the R_{SB} contribution of $R_{t,2}$ between the surface and the bulk remains unchanged or increases, as for the uncovered Si surface. However, the electronic structure within the plane has changed giving rise to higher lateral mobilities compared to the clean Si(111) surface and therefore, to an enlarged R_{leak} contribution.

However, the spectroscopy done with STM, is in fact a transport measurement. Thus, peaks in dI/dV curves originate from resonances induced by electronic states, e.g., surfaces states, in between the sample-tip configuration. Therefore, apart from the density of states two further aspects for the involved electronic states are of importance: First, the dispersion determines whether a resonant injection is possible. Since the tip is a point source (see Figure 2.5), the momentum distribution is a priori broad and depends in detail on the tunnelling distance and on the lateral extension of the structure. Consequently, resonant coupling is more effective for localised states or for band structures with small dispersion. Second, the lifetime of electrons in the electronic states has to be sufficiently large in order to enhance the tunnelling probability. Otherwise, the states of the nanostructure appear transparent in local spectroscopy, although the structure itself maybe highly metallic. This is how the

lateral size of the structure and the dispersion come into play, as these quantities control the R_{leak} contribution in the proposed model.

Summarising, the size of the structure and the dispersion are important here, as these quantities control the contribution of the R_{leak} channel. The occurrence of resonant peaks of the surface states in the dI/dV signal of the clean Si(111) surface and their absence in the Ag $\sqrt{3} \times \sqrt{3}$ structure can be explained in following terms: In contrast to Si(111) 7x7, the surface bands of the Ag $\sqrt{3} \times \sqrt{3}$ are strongly dispersing as seen by ARPES [CGM+05] [UHN+85]. The delocalised character is visible in a high electron mobility giving rise to a low sheet resistance in the order of magnitude of 1000 $\Omega/\square$ [PGSH00] [GKT+99] [HI92] [WW10]. A similar example are the Shockley surface states on noble metal surfaces, which are also barely resolvable.

3.3.2 Coulomb Blockade CB oscillations in isolated Ag structures

Adsorption of submonolayer amount of Ag at LT without annealing does not create a wetting layer, as presented in Figure 3.23. Layer of 0.2 ML Ag was evaporated on Si(111) surface at 80 K temperature. The Ag atoms occupy specific sites within the 7x7 Si surface cell, as the underlying structure remains visible. The dI/dV curves have been taken at the positions marked by the circle and the cross in Figure 3.23a. In Figure 3.23c, between the protrusions the characteristic unoccupied surface state of the Si(111) 7x7 reconstruction is still visible, that is, the Si surface remains intact under the array of Ag clusters, whereas the STS on the Ag clusters does not show this state.

This experimental finding will be now compared with larger Ag islands. Adsorption of 0.6 ML at LT, followed by annealing to 300 K leads to creation of larger but still not percolated Ag islands, as presented in Figure 3.24. It is expected that Ag $\sqrt{3} \times \sqrt{3}$ layer is not created, due to not high enough annealing temperature. The dI/dV curves obtained from STS measurement reveal completely different character than clean surfaces. In Figure 3.24b the curves A–C were taken on the separate Ag islands, whereas curve D was taken on large area percolated Ag structure. The equidistant peaks in curves A-C are easily visible in the bias range from -1 v to +1 V. Such resonances in this measurement system are the sign of a double tunnelling barrier. Therefore, these oscillations are expected to originate from a CB effect, where the electrons are tunnelling one by one through the Ag quantum dot structure.

The thickness of these islands is only one monolayer (see inset of Figure 3.24a),

(a) STM image of 0.2 ML Ag adsorbed on Si(111) at 80 K (10x10 nm², -2 V, 0.05 nA). The cluster matrix.

(b) STM image of clean Si(111) 7x7 surface reconstruction (10x10 nm², +2 V, 0.2 nA).

(c) STS dI/dV spectra taken on and in between the clusters. The positions are marked by a circle and cross in (a), respectively.
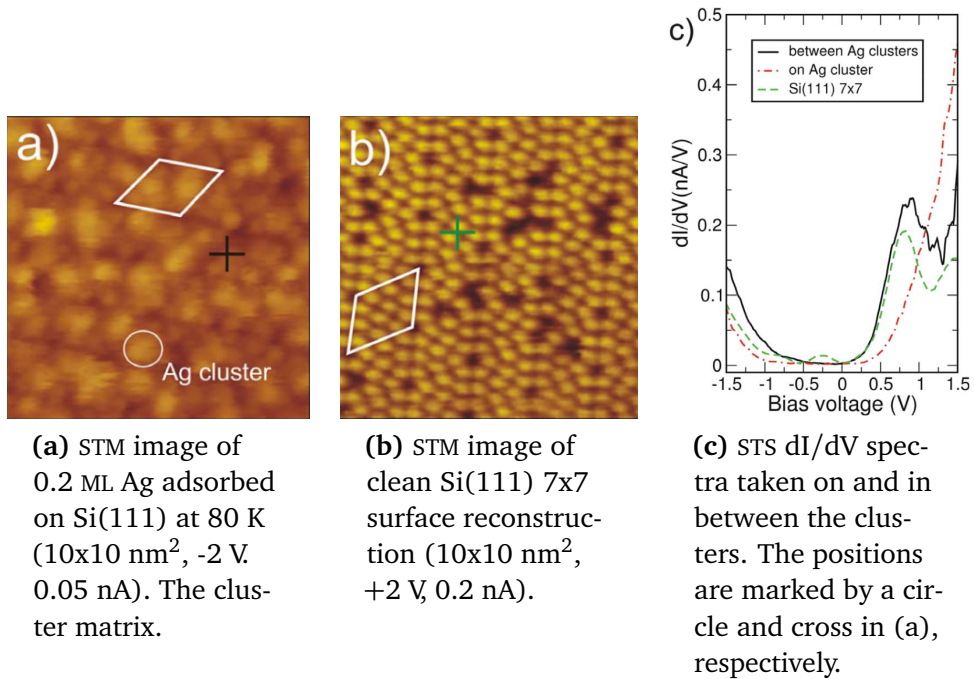
Figure 3.23: The comparison with the corner hole structure of the clean Si(111) surface (b) shows that the Ag clusters on (a) are aligned along the 7x7 reconstruction. The unoccupied Si-surface state is visible in between the Ag clusters. For comparison, the spectrum of the clean surface is shown as dashed green line [SPT09].

therefore resonances induced by quantum well states QWS, which have been observed by STS for similar but thicker metal/semiconductor systems, can be excluded [AMC97] [QYM+07]. The QWS energetic separation can be roughly calculated from the formula $\Delta = \pi \hbar v_F / D$, where $\hbar$ is Planck's constant, v_F is the Fermi velocity and D is the film thickness. Furthermore, for epitaxial Ag films on Si(111) a height of at least ten layers are needed to reveal splitting of around 1 eV for QWS (here $v_F = 1.4 \times 10^8 cm/s$), which is significantly more than the coverages investigated here [AMC97] [QYM+07].

The peak separation ΔE for the three investigated Ag islands (A–C in Figure 3.24a) is between 0.4 eV and 0.6 eV. As the capacitances can be determined from the voltage period of the oscillations, the capacitances of the tunnelling junction are between 0.26 aF and 0.4 aF, according to the formula $C = e/\Delta E$. These capacitances are small enough so that CB oscillations can be seen already at measurement temperature of 80 K.

Investigation of the Coulomb suppression in single tunnelling junction systems have

(a) Different Ag islands labelled A-D of monatomic height. Inset shows line scan through island B and reveals 1 ML height. (43x50 nm^2, +2 V, 0.5 nA)

(b) dI/dV measurements taken on four different Ag islands (+1.5 V, 0.5 nA, except C: +2 V, 0.5 nA)
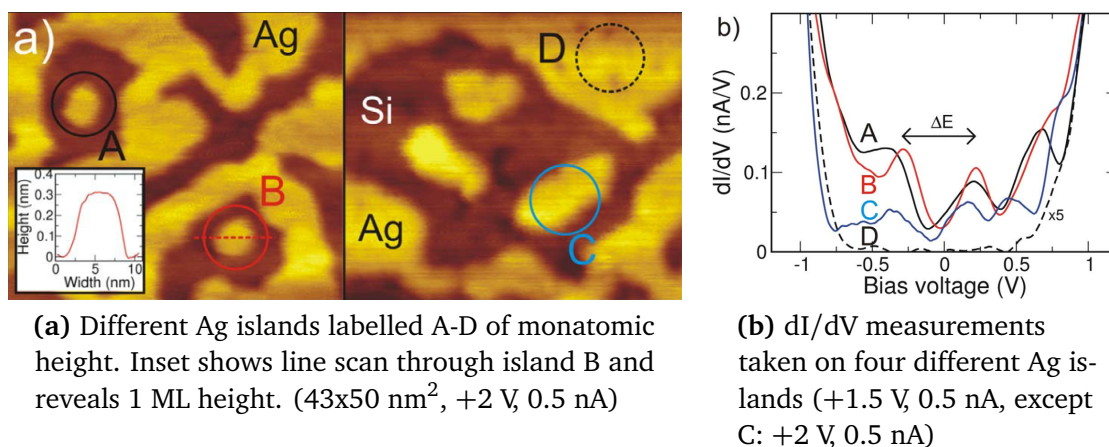
Figure 3.24: STM images of Si(111) surface after adsorption of 0.6 ML Ag at 80 K and annealing to 300 K. Pronounced CB oscillations are seen in the Si gap, only for not percolated Ag islands (A-C) [SPT09].

shown that the capacitance of the junction is inversely proportional to the sample-tip distance d [BLSK89], thus as a first-order approximation it can be described as a simple parallel capacitor with a capacitance of $C = \varepsilon\varepsilon_0 A/d$, where A is the effective area of capacitor. Taking into account the estimates of the capacitances of islands A–C (see in Figure 3.24a), it can be concluded that the islands shown in Figure 3.23 with an average diameter of 1 nm must have a capacitance below 0.01 aF. Therefore the peak separation ΔE of CB for such low capacitance is expected to be around 16 V and thus is not expected to be observed in standard STS measurement (Figure 3.23c). Summarising, for structures without wetting layer, within a double barrier junction, the CB is the dominating effect.

3.3.3 The role of the wetting layer in Ag multilayer systems

The aimed creation of nonpercolated Ag structures grown on Si(111) reveal a double barrier junction character, i.e., the CB oscillations were seen in STS. This finding from the previous section will be extended by the investigation of thicker structures. It will be shown that also in this situation, for up to 3 ML thick nonpercolated structures, deposited similarly in LT (80 K) without Ag $\sqrt{3} \times \sqrt{3}$ wetting layer and annealed to RT, the characteristic signatures remain.

Annealing of 3 ML Ag to RT leads to creation of a granular film, shown in Fig-

ure 3.26a. Again, this relatively low temperature, does not allow the formation of Ag $\sqrt{3} \times \sqrt{3}$ reconstruction. In STS conductivity measurements the oscillatory behaviour is clearly visible, as shown in Figure 3.26b. The asymmetry of the spectra might be induced by the inhomogeneity of the surrounding clusters. As the size of the grains is comparable with the structures A-C investigated in the previous section (see Figure 3.24), the period of oscillation is also of the same order of magnitude. However, in this case the film shows a metallic behaviour, i.e., the Si band gap is not visible in the I/V curve obtained from STS. A direct conclusion is, that the film is percolated on a macroscopic scale and that a direct connection to the bias sample contact is provided, thus turning the double barrier system into a single barrier structure. However, due to the granularity of the film, the life-time of the injected electron introduces the CB oscillations into the dI/dV measurement.
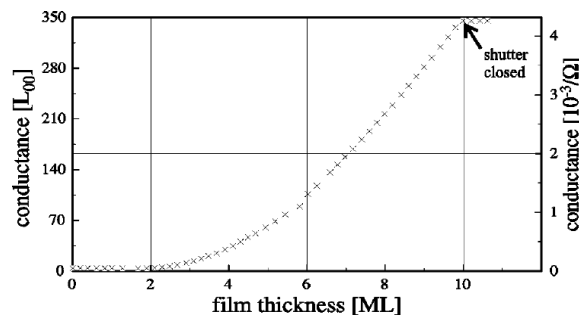
Figure 3.25: Conductance of a growing Ag film during deposition at about 15 K. Figures by Henzler et al. [HLB98].

It should be noted that this observation is in agreement with a previous investigation of Ag film conductance on a macroscopic scale [HLB98], where a macroscopic four-point probe technique (Van-der-Pauw geometry) was used (see Figure 3.25). Supporting our spectroscopic measurements, the CB limited tunnelling between the grains is suggested as a mechanism for the transport in this nonmetallic system.

For comparison also the Ag islands were evaporated onto the Ag $\sqrt{3} \times \sqrt{3}$ reconstruction, as shown in Figure 3.27a. Here, it is found that the former double barrier limited transport will change into a single barrier one. The hexagonal shape of the islands is a hallmark of a crystalline and well oriented growth of the islands on the reconstructed surface. The dI/dV curve obtained by STS measurements taken on the island, marked by a cross in Figure 3.27a, does not show any oscillations, even though the size of is similar to the previously investigated islands.
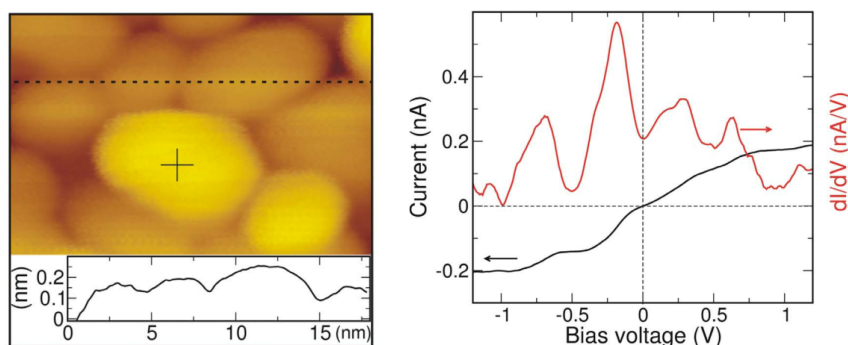
(a) STM image of granular film (18x13.5 nm^2: -1.5 V, 0.25 nA). The line scan taken along the dashed line shows the percolation of adjacent Ag clusters.

(b) I/V and dI/dV curves taken at the cluster in (a) at the cross-marked position showing CB oscillations.

Figure 3.26: 3 ML Ag film annealed to 300 K forming a granular film structure on Si(111) [SPT09].

Investigating the curves in details reveals that the current is depending nonlinearly on voltage in the low bias regime, whereas at high bias this dependence is linear. This behaviour is characteristic for a single tunnelling barrier setups, where a suppression of charge transfer is visible and oscillations are averaged out due to scattered capacitances within the system. Assuming an suppression of current due to CB effect low voltages, the separation of the asymptotic lines ($\Delta V = 0.4$ V) is related to the capacitance by $C = e/\Delta V = 0.4$ aF, which is of the same order of magnitude as in previously measured islands. To support this statement and to demonstrate the size dependence, three Ag islands of different sizes (40 nm^2, 90 nm^2, 900 nm^2) were measured by means of STS spectroscopy, shown in Figure 3.27b. This simple model for the capacitance of the tunnelling junction is in qualitative agreement and the separation between the extrapolated linear regimes become smaller with increasing size of island, as expected.

As the shape of the spectroscopic I/V curve depends only on R_t and C through the formula $I = (2C/\pi R_t e)V^2$ [AL86] [AL87], the values of the capacitance and of the tunnelling resistance can be obtained independently for the low voltage regime for zero temperature, as shown e.g. for the I/V curve in Figure 3.27a. This parameter-free curve thin drawn blue curve is in reasonable agreement with the experiment. The deviation in the low bias regime is not likely due to the parasitic leakage currents.
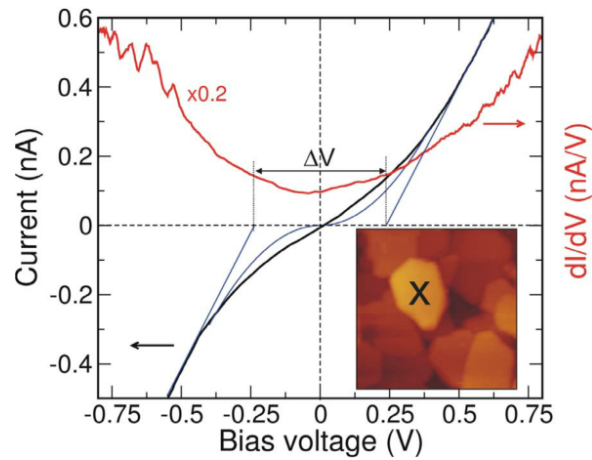
(a) I/V (black) and dI/dV curves (red) taken on the island (inset: 40x40 nm^2). STS set point: +0.5 V, 0.3 nA.
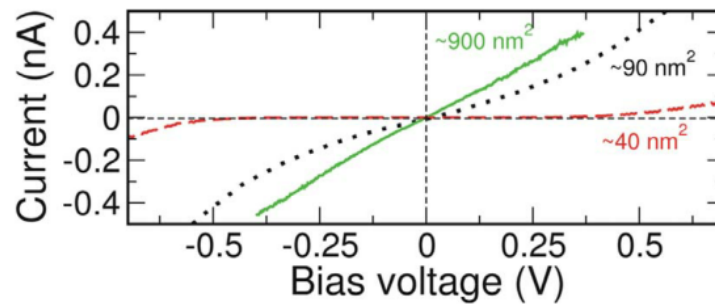
(b) STS measurement of differently sized Ag islands.

Figure 3.27: STM and STS measurement of the crystalline well ordered Ag islands grown on an Ag wetting layer. The voltage gap ΔV in (a) in between the intersections is intimately related to the capacitance C of the tunnel junction through $\Delta V = e/C$. The blue lines represent asymptotes at high biases and a quadratic fit in the low bias regime using $R_t = 1$ GΩ and $C = 0.4$ aF. (b) [SPT09].

Besides the suppression due to CB of the current in the low bias regime, the average conductivity is significantly higher compared to the bare Ag $\sqrt{3} \times \sqrt{3}$ phase. The electronic behaviour of the investigated system can be explained by taking into account additionally adsorbed Ag material, which nucleates at step sites and connects Ag $\sqrt{3} \times \sqrt{3}$ reconstructed terraces, lowering the planar resistivity. The Schottky Barrier SB remains at the surface, as Crain et al. [CGM+05] have shown by photoemission experiments. Therefore, the lateral properties of the Ag $\sqrt{3} \times \sqrt{3}$ reconstruction are important for the transition from the double to an effective single tunnelling barrier.

Applying the observations to the equivalent circuit diagram of the heterostructure presented in Figure 3.20, it seems that R_{leak} must be significantly decreased. On one hand, it can be decreased by increasing the concentration of defects within the whole depletion layer of the Si interface. The generation of the well ordered Ag $\sqrt{3} \times \sqrt{3}$ wetting layer is unlikely that to be the source of such effect. Taking into account the defect concentration for the clean Si(111) surface, it would be required that nearly every lattice site would have to be coupled through defect states to the bulk material in order to decrease R_{leak} by three orders of magnitude. Although, it is visible that Ag $\sqrt{3} \times \sqrt{3}$ structure consists of many domain boundaries, but their concentration is still insufficient [HSS+00]. Alternatively, the mobility of the electrons within the wetting layer must be orders of magnitude higher than on the Si surface without the wetting layer and the coupling between the Ag islands and the wetting layer must be strong. The resistivity value for Si in this case in range of 20000 $\Omega/\square$, thus previous assumptions are consistent with the known resistivity of the Ag wetting layer, which is in range of 1000 $\Omega/\square$ [PGSH00] [GKT+99] [HI92] [JB88]. This is expected behaviour for Ag islands on an Ag wetting layer. This leads to disappearance of the resonances within an individual island. High electron mobility and the absence of resonances in STS due to a significantly dispersing band structure within the wetting layer has already been concluded from the results of the perfect Ag $\sqrt{3} \times \sqrt{3}$ structure. Furthermore, the diffusion of the electrons in the plane is increased, i.e., without significant change in the initial defect concentration, the spread of the electrons is responsible for a sufficiently low R_{leak} resistance, which overcompensates the "local" Schottky Barrier resistance R_{SB}. The lateral transport measurements using a four point-probe technique on the micrometer scale are in qualitative agreement with the this experiment [MLH+07]. The relative resistance is lowered by three orders of magnitude for the Ag $\sqrt{3} \times \sqrt{3}$ at low temperatures (100 K) compared to the Si(111) 7x7 reconstruction.

CHAPTER 4

Summary and outlook

Concluding, the Si(111) / Ag $\sqrt{3} \times \sqrt{3}$ system have been thoroughly investigated to build the basis for advanced experiments of adsorption of molecules on this system. As mentioned before, following the path of the bottom-up approach, the full understanding of substrate systems is critical: on one hand, for the proper interpretation and evaluation of more complex measurement data, and on the other hand, for the aimed engineering of the devices.

The domain walls on Ag $\sqrt{3} \times \sqrt{3}$ were investigated and structural and electronic model have been introduced and discussed. The influence on the structure and electronic characteristic should not be neglected, as together with the miniaturisation this imperfection may play much more significant role in functioning of the micro- and nano-electronic devices. Furthermore, the temperature dependence was investigated, showing the Peierls-type transition.

Temperature and bias voltage dependent STM measurements have revealed that localised 1D electronic properties can be obtained at domain boundaries in the monolayer of silver forming a Ag $\sqrt{3} \times \sqrt{3}$ structure. The peculiar properties found here may be related to the special kind of broken symmetry of the domain walls under investigation, which involve also the substrate-overlayer-symmetry coupled with the change of positions of Si trimers around T_4 to H_3 positions.

The high resolution STM data of the local adsorption geometry of FDT on Ag $\sqrt{3} \times \sqrt{3}$ were presented. The stress-less adsorption of the molecule within the unit cell of the Ag reconstruction is provided by rotational flexibility of the FDT molecule. The comparison of theoretical results obtained for the molecule, on Ag(111) and Ag $\sqrt{3} \times \sqrt{3}$ surfaces, with STM measurement at RT, support the chemisorption with

thiolate bonds to the Ag trimers on the HCT surface. The molecule is aligned with the Cp–Fe-Cp axis parallel to the surface, while the rotational freedom of the molecule is limited due to chemisorption. The presented adsorption model was supported by experiment and simulation.

The perfect Ag $\sqrt{3} \times \sqrt{3}$ was prepared and investigated by means of STM, focusing on structural and electronic characteristics. The different reconstructions and amounts of Ag on Si were investigated; the submonolayer amounts, Ag $\sqrt{3} \times \sqrt{3}$ wetting layers, perfect epitaxial layers and multilayer systems. The influence of wetting layer on electronic character of deposited Ag nanostructures was studied. The occurrence of effective single and double barriers in tunnelling microscopy and spectroscopy for the Ag $\sqrt{3} \times \sqrt{3}$ system was investigated in the monolayer regime by varying the measurement and preparation conditions. The results obtained with local probe STM and STS can be correlated with mesoscopic transport and provide a more detailed insight into the underlying mechanisms.

Two-dimensional localisation is visible in lateral conductance measured on mesoscopic and even macroscopic scales. Here the efficient localisation at time scales relevant in tunnelling experiments and formation of double barriers was found in all situations where Ag islands were grown directly on the Si(111) surface, i.e., without the Ag $\sqrt{3} \times \sqrt{3}$ reconstruction. The Coulomb Blockade oscillations were found for granular multilayer Ag films, whereas similar structures with existence of Ag $\sqrt{3} \times \sqrt{3}$ show only a single barrier characteristic. The vertical transport properties in this metal/semiconductor system depend on the structure and bonding on the atomic scale and on the lateral two-dimensional properties of the interface.
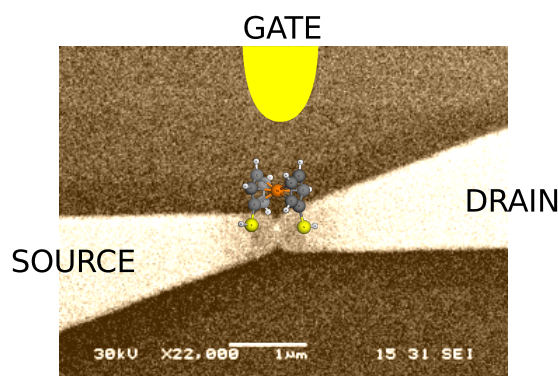
Figure 4.1: Example scheme of possible realisation of planar molecular switch (Image not to scale).

Summarising, the choice of Si/Ag system was dictated by the interesting S-Ag thiolate bonds introduced by the FDT molecule. The investigations of the Ag structures on Si, build a basis for further experiments on this system. Furthermore, this project have extended the earlier investigations of molecular nanocontacts, also focused on work with FDT [Sch06] [GSP+06]. Having a extended knowledge about Si/Ag system, application of the bottom-up approach for the Si/Ag/FDT based, a simple moletronics device may follow.

Bibliography

[AL86]   AVERIN, DV ; LIKHAREV, KK: Coulomb blockade of single-electron tunneling, and coherent oscillations in small tunnel junctions. In: *Journal of low temperature physics* 62 (1986), Nr. 3, S. 345–373 (Page 74)

[AL87]   AVERIN, D. ; LIKHAREV, K.: New results of the theory of SET and Bloch oscillations in small tunnel junctions. In: *Magnetics, IEEE Transactions on* 23 (1987), Nr. 2, S. 1138–1141 (Page 74)

[AMC97] ALTFEDER, IB ; MATVEEV, KA ; CHEN, DM: Electron fringes on a quantum wedge. In: *Physical review letters* 78 (1997), Nr. 14, S. 2815–2818 (Page 71)

[AR74]   AVIRAM, A. ; RATNER, M.A.: Molecular rectifiers. In: *Chemical Physics Letters* 29 (1974), S. 277–283 (Page 5, 6, 7, 8, and 96)

[ATSH99] AIZAWA, H. ; TSUKADA, M. ; SATO, N. ; HASEGAWA, S.: Asymmetric structure of the Si $(111)(\sqrt{3}x\sqrt{3})$ Ag surface. In: *Surface Science* 429 (1999), Nr. 1-3, S. L509–L514 (Page 28)

[Bar47] BARDEEN, J.: Surface states and rectification at a metal semi-conductor contact. In: *Physical Review* 71 (1947), Nr. 10, S. 717 (Page 34)

[Bar61] BARDEEN, J.: Tunnelling from a many-particle point of view. In: *Physical Review Letters* 6 (1961), Nr. 2, S. 57–59. – ISSN 1079–7114 (Page 16)

[BB10]   BAUMGARDT, I. ; BUTENSCHÖN, H.: 1,1'-Diaryl-Substituted Ferrocenes: Up to Three Hinges in Oligophenyleneethynylene-Type Molecular Wires. In: *European Journal of Organic Chemistry* 2010 (2010), Nr. 6, S. 1076–1087 (Page 31)

[BBB+90]   BURROUGHES, JH ; BRADLEY, DDC ; BROWN, AR ; MARKS, RN ; MACKAY, K. ; FRIEND, RH ; BURNS, PL ; HOLMES, AB: Light-emitting diodes based on conjugated polymers. In: *nature* 347 (1990), Nr. 6293, S. 539–541. – ISSN 0028–0836 (Page 5)

[Ber55]   BERNANOSE, A.: Electroluminescence of organic compounds. In: *British Journal of Applied Physics* 6 (1955), S. S54 (Page 5)

[BFK+83]   BENNETT, P. A. ; FELDMAN, L. C. ; KUK, Y. ; MCRAE, E.G. ; ROWE, J.E.: Stacking-fault model for the Si(111) - (7x7) surface. In: *Physical Review B* 28 (1983), S. 3656–3659 (Page 21)

[BHY+90]   BULLOCK, EL ; HERMAN, GS ; YAMADA, M. ; FRIEDMAN, DJ ; FADLEY, CS u. a.: Structure of $(\sqrt{3}x\sqrt{3})$R30° Ag on Si (111). In: *Physical Review B* 41 (1990), Nr. 3, S. 1703–1706. – ISSN 1550–235X (Page 25)

[Blö94]   BLÖCHL, P.E.: Projector augmented-wave method. In: *Physical Review B* 50 (1994), Nr. 24, S. 17953 (Page 33)

[BLSK89]   BENTUM, PJM van ; LEEMPUT, LEC ; SMOKERS, RTM ; KEMPEN, H. van: Single Electron Effects in Low Capacitance Point-Contact Tunnel Junctions. In: *Physica Scripta* 1989 (1989), S. 122 (Page 72)

[BP72]   BAUER, E. ; POPPA, H.: Recent advances in epitaxy. In: *Thin Solid Films* 12 (1972), Nr. 1, S. 167–185 (Page 27)

[BRGW82a]   BINNIG, G. ; ROHRER, H. ; GERBER, C. ; WEIBEL, E.: Surface studies by scanning tunneling microscopy. In: *Physical Review Letters* 49 (1982), Nr. 1, S. 57–61. – ISSN 1079–7114 (Page 12)

[BRGW82b]   BINNIG, G. ; ROHRER, H. ; GERBER, C. ; WEIBEL, E.: Tunneling through a controllable vacuum gap. In: *Applied Physics Letters* 40 (1982), Nr. 2, S. 178–180. – ISSN 0003–6951 (Page 12)

[BRGW83]   BINNIG, G. ; ROHRER, H. ; GERBER, C. ; WEIBEL, E.: 7x7 Reconstruction on Si(111) Resolved in Real Space. In: *Phys. Rev. Lett.* 50 (1983), Nr. 2, S. 120–123. http://dx.doi.org/10.1103/PhysRevLett.50.120. – DOI 10.1103/PhysRevLett.50.120 (Page 22)

[BTP+08] BREDOW, T. ; TEGENKAMP, C. ; PFNÜR, H. ; MEYER, J. ; MASLYUK, VV ; MERTIG, I.: Ferrocene-1, 1-dithiol as molecular wire between Ag electrodes: The role of surface defects. In: *The Journal of chemical physics* 128 (2008), S. 064704 (Page 58 and 65)

[BÜL+10] BELIANINOV, A. ; ÜNAL, B. ; LU, N. ; JI, M. ; HO, K.M. ; WANG, C.Z. ; TRINGIDES, MC ; THIEL, PA: Islands and holes as measures of mass balance in growth of the (sqrt [3]× sqrt [3]) R30° phase of Ag on Si (111). In: *Physical Review B* 82 (2010), Nr. 24, S. 245413 (Page 40)

[CC74] CHELIKOWSKY, J. ; COHEN, M.L.: Electronic structure of silicon. In: *Physical Review B* 10 (1974), Nr. 12, S. 5095 (Page 21)

[CDG+11] CHENG, Z. ; DU, S. ; GUO, W. ; GAO, L. ; DENG, Z. ; JIANG, N. ; GUO, H. ; TANG, H. ; GAO, H.J.: Direct imaging of molecular orbitals of metal phthalocyanines on metal surfaces with an O 2-functionalized tip of a scanning tunneling microscope. In: *Nano Research* (2011), S. 1–8 (Page 20)

[CGM+05] CRAIN, JN ; GALLAGHER, MC ; McCHESNEY, JL ; BISSEN, M. ; HIMPSEL, FJ: Doping of a surface band on Si (111) $\sqrt{3}x\sqrt{3}$-Ag. In: *Physical Review B* 72 (2005), Nr. 4, S. 045312 (Page 25, 52, 68, 69, 70, 75, and 99)

[CH80] CLABES, J. ; HENZLER, M.: Determination of surface states on Si (111) by surface photovoltage spectroscopy. In: *Physical Review B* 21 (1980), Nr. 2, S. 625 (Page 22 and 67)

[Che02] CHELIKOWSKY, J.: Silicon in all its forms. In: *MRS bulletin* 27 (2002), Nr. 12, S. 951–960 (Page 21)

[CMZ+04] CRAIN, JN ; McCHESNEY, JL ; ZHENG, F. ; GALLAGHER, MC ; SNIJDERS, PC ; BISSEN, M. ; GUNDELACH, C. ; ERWIN, SC ; HIMPSEL, FJ: Chains of gold atoms with tailored electronic states. In: *Physical Review B* 69 (2004), Nr. 12, S. 125401 (Page 40)

[CNS+10] CHAIKA, AN ; NAZIN, SS ; SEMENOV, VN ; BOZHKO, SI ; LÜBBEN, O. ; KRASNIKOV, SA ; RADICAN, K. ; SHVETS, IV: Selecting the tip electron orbital for scanning tunneling microscopy imaging with sub-ångström

lateral resolution. In: *EPL (Europhysics Letters)* 92 (2010), S. 46003 (Page 20)

[CP05] CRAIN, J.N. ; PIERCE, D.T.: End states in one-dimensional atom chains. In: *Science* 307 (2005), Nr. 5710, S. 703 (Page 40)

[CPT09] CZUBANOWSKI, M. ; PFNUR, H. ; TEGENKAMP, C.: Atomic chain ordering with ultra-long periods: Pb/Si(557). In: *Surface Science* 603 (2009), Nr. 19, S. L121–L124 (Page 40)

[CS65] COWLEY, AM ; SZE, SM: Surface States and Barrier Height of Metal-Semiconductor Systems. In: *Journal of Applied Physics* 36 (1965), Nr. 10, S. 3212–3220 (Page 34 and 36)

[Czo18] CZOCHRALSKI, J.: Ein neues Verfahren zur Messung des Kristallisationsgeschwindigkeit der Metalle. In: *Z. Phys. Chem.* 92 (1918), S. 219–221 (Page 20)

[DCH91] DING, Y. G. ; CHAN, C. T. ; HO, K. M.: Structure of the $(\sqrt{3}x\sqrt{3})R30°$ Ag/Si(111) surface from first-principles calculations. In: *Phys. Rev. Lett.* 67 (1991), Sep, Nr. 11, S. 1454–1457. `http://dx.doi.org/10.1103/PhysRevLett.67.1454`. – DOI 10.1103/PhysRevLett.67.1454 (Page 25 and 27)

[DTH+97] DATTA, S. ; TIAN, W. ; HONG, S. ; REIFENBERGER, R. ; HENDERSON, J.I. ; KUBIAK, C.P.: Current-voltage characteristics of self-assembled monolayers by scanning tunneling microscopy. In: *Physical review letters* 79 (1997), Nr. 13, S. 2530–2533 (Page 9)

[EF05] ESEN, G. ; FUHRER, MS: Temperature control of electromigration to form gold nanogap junctions. In: *Applied Physics Letters* 87 (2005), S. 263101 (Page 9)

[EOK+05] ELBING, M. ; OCHS, R. ; KOENTOPP, M. ; FISCHER, M. ; HÄNISCH, C. V. ; WEIGEND, F. ; EVERS, F. ; WEBER, H.B. ; MAYOR, M.: A single-molecule diode. In: *Proceedings of the National Academy of Sciences of the United States of America* 102 (2005), Nr. 25, S. 8815 (Page 9)

[FHKP04] FÖLSCH, S. ; HYLDGAARD, P. ; KOCH, R. ; PLOOG, KH: Quantum confinement in monatomic Cu chains on Cu (111). In: *Physical review letters* 92 (2004), Nr. 5, S. 56803 (Page 53)

[FIHT89] FAN, WC ; IGNATIEV, A. ; HUANG, H. ; TONG, SY: Observation and structural determination of ($\sqrt{3}x\sqrt{3}$) R30° reconstruction of the Si (111) surface. In: *Physical review letters* 62 (1989), Nr. 13, S. 1516–1519 (Page 27)

[GEW+05] GETTY, S.A. ; ENGTRAKUL, C. ; WANG, L. ; LIU, R. ; KE, S.H. ; BARANGER, H.U. ; YANG, W. ; FUHRER, M.S. ; SITA, L.R.: Near-perfect conduction through a ferrocene-based molecular wire. In: *Physical Review B* 71 (2005), Nr. 24, S. 241401 (Page 10 and 30)

[GI83] GOTOH, Y. ; INO, S.: Epitaxial growth of silver on an Si(111) 7x7 surface at room temperature. In: *Thin Solid Films* 109 (1983), Nr. 3, S. 255–261. – ISSN 0040–6090 (Page 29)

[GKT+99] GAVIOLI, L. ; KIMBERLIN, K.R. ; TRINGIDES, M.C. ; WENDELKEN, J.F. ; ZHANG, Z.: Novel growth of Ag islands on Si (111): Plateaus with a singular height. In: *Physical review letters* 82 (1999), Nr. 1, S. 129–132 (Page 40, 70, and 76)

[GLa] GLADOS: *Portal, Aperture Science Enrichment Center* (Page 2)

[Gre10] GREEN500: *Ranking of the most energy-efficient supercomputers in the world.* http://www.green500.org. Version: 2010 (Page 2)

[GSP+06] GARDINOWSKI, G. ; SCHMEIDEL, J. ; PFNÜR, H. ; BLOCK, T. ; TEGENKAMP, C.: Switchable nanometer contacts: Ultrathin Ag nanostructures on Si (100). In: *Applied physics letters* 89 (2006), S. 063120 (Page 9 and 79)

[GW06] GOTTLIEB, A.D. ; WESOLOSKI, L.: Bardeen's tunnelling theory as applied to scanning tunnelling microscopy: a technical guide to the traditional interpretation. In: *Nanotechnology* 17 (2006), S. R57 (Page 17)

[HAB+01] HIMPSEL, FJ ; ALTMANN, KN ; BENNEWITZ, R. ; CRAIN, JN ; KIRAKOSIAN, A. ; LIN, JL ; MCCHESNEY, JL: One-dimensional electronic states at surfaces. In: *Journal of Physics: Condensed Matter* 13 (2001), S. 11097 (Page 40)

[HF82]   HUSE, D.A. ; FISHER, M.E.: Domain walls and the melting of commensurate surface phases. In: *Physical Review Letters* 49 (1982), Nr. 11, S. 793–796 (Page 32 and 39)

[HI92]   HASEGAWA, S. ; INO, S.: Surface structures and conductance at epitaxial growths of Ag and Au on the Si (111) surface. In: *Physical review letters* 68 (1992), Nr. 8, S. 1192–1195 (Page 70 and 76)

[HKC+01]   HIMPSEL, FJ ; KIRAKOSIAN, A. ; CRAIN, JN ; LIN, J.L. ; PETROVYKH, DY: Self-assembly of one-dimensional nanostructures at silicon surfaces. In: *Solid state communications* 117 (2001), Nr. 3, S. 149–157 (Page 40)

[HLB98]   HENZLER, M. ; LÜER, T. ; BURDACH, A.: Nonmetallic conductivity of epitaxial monolayers of Ag at low temperatures. In: *Physical Review B* 58 (1998), Nr. 15, S. 10046 (Page 73 and 100)

[HOPZ06]   HOUSELT, A. van ; ONCEL, N. ; POELSEMA, B. ; ZANDVLIET, H.J.W.: Spatial mapping of the electronic states of a one-dimensional system. In: *Nano letters* 6 (2006), Nr. 7, S. 1439–1442 (Page 55)

[HSS+00]   HASEGAWA, S. ; SATO, N. ; SHIRAKI, I. ; PETERSEN, C.L. ; BØGGILD, P. ; HANSEN, T.M. ; NAGAO, T. ; GREY, F.: Surface-State Bands on Silicon—Si (111)-($\sqrt{3}x\sqrt{3}$) Surface Superstructure. In: *Jpn. J. Appl. Phys* 39 (2000), S. 3815–3822 (Page 76)

[HTD86]   HAMERS, RJ ; TROMP, RM ; DEMUTH, JE: Surface electronic structure of Si (111)-(7x7) resolved in real space. In: *Physical Review Letters* 56 (1986), S. 1972–1975 (Page 22 and 67)

[ITR09]   ITRS: *International Technology Roadmap for Semiconductors*. `http://www.itrs.net/Links/2009ITRS/Home2009.htm`. Version: 2009 (Page 2)

[JB88]   JAŁUCHOWSKI, M. ; BAUER, E.: Quantum size and surface effects in the electrical resistivity and high-energy electron reflectivity of ultrathin lead films. In: *Physical Review B* 38 (1988), Nr. 8, S. 5272 (Page 76)

[Kel91]   KELLER, D.: Reconstruction of STM and AFM images distorted by finite-size tips. In: *Surface Science* 253 (1991), Nr. 1-3, S. 353–364 (Page 19)

[KH93]   KRESSE, G. ; HAFNER, J.: Ab initio molecular dynamics for open-shell transition metals. In: *Physical Review B* 48 (1993), Nr. 17, S. 13115 (Page 33)

[KJ10]   KWAPINSKI, T. ; JALOCHOWSKI, M.: Signature of tip electronic states on tunneling spectra. In: *Surface Science* 604 (2010), Nr. 19-20, S. 1752–1756 (Page 20)

[KP51]   KEALY, TJ ; PAUSON, PL: A new type of organo-iron compound. In: *Nature* 168 (1951), S. 1039–1040 (Page 30)

[KS+65] KOHN, W. ; SHAM, LJ u. a.: Self-consistent equations including exchange and correlation effects. In: *Physical Review* 140 (1965), Nr. 4A, S. 1133–1138 (Page 33)

[KS86]   KUK, Y. ; SILVERMAN, PJ: Role of tip structure in scanning tunneling microscopy. In: *Applied physics letters* 48 (1986), Nr. 23, S. 1597–1599 (Page 19)

[KWTT07] KUBOTA, Y. ; WATANABE, K. ; TSUDA, O. ; TANIGUCHI, T.: Deep ultraviolet light-emitting hexagonal boron nitride synthesized at atmospheric pressure. In: *Science* 317 (2007), Nr. 5840, S. 932 (Page 3)

[LDE+11] LORUSSO, G.F. ; DAVYDOVA, N. ; EURLINGS, M. ; KAYA, C. ; PENG, Y. ; FEENSTRA, K. ; FEDYNYSHYN, T.H. ; NATT, O. ; HUBER, P. ; ZACZEK, C. u. a.: Deep ultraviolet out-of-band contribution in extreme ultraviolet lithography: predictions and experiments. In: *Proceedings of SPIE* Bd. 7969, 2011, S. 79692O (Page 3)

[LDTH87] LOENEN, E.J. V. ; DEMUTH, J.E. ; TROMP, R.M. ; HAMERS, R.J.: Local electron states and surface geometry of Si (111)-$\sqrt{3}x\sqrt{3}$ Ag. In: *Physical review letters* 58 (1987), Nr. 4, S. 373–376 (Page 27)

[LHK+94] LUO, EZ ; HEUN, S. ; KENNEDY, M. ; WOLLSCHLÄGER, J. ; HENZLER, M.: Surface roughness and conductivity of thin Ag films. In: *Physical Review B* 49 (1994), Nr. 7, S. 4858 (Page 22 and 67)

[LITV84] LOENEN, E.J. V. ; IWAMI, M. ; TROMP, R.M. ; VEEN, J.F. Van D.: The adsorption of Ag on the Si(111) 7x7 surface at room temperature studied

by medium energy ion scattering, LEED and AES. In: *Surface science* 137 (1984), Nr. 1, S. 1–22. – ISSN 0039–6028 (Page 29)

[LSZ94]   LIFSHITS, VG ; SARANIN, AA ; ZOTOV, AV: *Surface phases on silicon: Preparation, Structures, and Properties*. Wiley, 1994 (Page 20)

[MBTP06] MEYER, J. ; BREDOW, T. ; TEGENKAMP, C. ; PFNÜR, H.: Thiol and thiolate bond formation of ferrocene-1, 1-dithiol to a Ag (111) surface. In: *The Journal of chemical physics* 125 (2006), S. 194705 (Page 30, 58, 60, 61, 62, and 64)

[McR83a] MCRAE, E.G.: Structure of Si(111) - 7x7. In: *Surface Science* 124 (1983), Nr. 1, S. 106– 128 (Page 21)

[McR83b] MCRAE, E.G.: Surface stacking sequence and (7x7) reconstruction at Si(111) surfaces. In: *Physical Review B* 28 (1983), Nr. 4, S. 2305–2307 (Page 21)

[Mey06]   MEYER, J.: *Simulation des Adsorptionsverhaltens von Ferrocen-basierten Molekülen auf Ag(111)*, Leibniz Universität Hannover, Diplomarbeit, März 2006 (Page 30, 58, 60, 62, and 65)

[MH08]   MIYAZAKI, M. ; HIRAYAMA, H.: Thickness and deposition temperature-dependent morphological change in electronic growth of ultra-thin Ag films on Si(111) substrates. In: *Surface Science* 602 (2008), Nr. 1, S. 276–282. – ISSN 0039–6028 (Page 29)

[MLH+07] MATSUDA, I. ; LIU, C. ; HIRAHARA, T. ; UENO, M. ; TANIKAWA, T. ; KANAGAWA, T. ; HOBARA, R. ; YAMAZAKI, S. ; HASEGAWA, S. ; KOBAYASHI, K.: Electron-phonon interaction and localization of surface-state carriers in a metallic monolayer. In: *Physical review letters* 99 (2007), Nr. 14, S. 146805 (Page 76)

[Moo65]   MOORE, G: Cramming more components onto integrated circuits. In: *Electronics* 38 (1965), Nr. 8. `ftp://download.intel.com/research/silicon/moorespaper.pdf` (Page 2)

[MP76]   MONKHORST, H.J. ; PACK, J.D.: Special points for Brillouin-zone integrations. In: *Physical Review B* 13 (1976), Nr. 12, S. 5188–5192 (Page 33)

[MVM+08] MA, J. ; VOLLMANN, M. ; MENZEL, H. ; POHLE, S. ; BUTENSCHÖN, H.: New Molecular Wires with Two Ferrocene Hinges. In: *Journal of Inorganic and Organometallic Polymers and Materials* 18 (2008), Nr. 1, S. 41–50 (Page 31)

[MVR+96] MULLER, CJ ; VLEEMING, BJ ; REED, MA ; LAMBA, JJS ; HARA, R. ; II, L.J. ; TOUR, JM: Atomic probes: a search for conduction through a single molecule. In: *Nanotechnology* 7 (1996), S. 409 (Page 9)

[MWP79] MCKINLEY, A. ; WILLIAMS, RH ; PARKE, AW: An investigation of thin silver films on cleaved silicon surfaces. In: *Journal of Physics C: Solid State Physics* 12 (1979), S. 2447 (Page 29)

[NMY96] NATORI, A. ; MURAYAMA, M. ; YASUNAGA, H.: Atomic structures of Ag on and on 7x7 Si (111). In: *Surface Science* 357 (1996), S. 47–50 (Page 29)

[Nor86] NORTHRUP, J.E.: Origin of surface states on Si (111)(7x7). In: *Phys. Rev. Lett.* 57 (1986), Nr. 1, S. 154–154. `http://dx.doi.org/ 10.1103/PhysRevLett.57.154`. – DOI 10.1103/PhysRevLett.57.154 (Page 22 and 67)

[OGA89] OLESINSKI, RW ; GOKHALE, AB ; ABBASCHIAN, GJ: The Ag-Si (Silver-Silicon) system. In: *Journal of Phase Equilibria* 10 (1989), Nr. 6, S. 635–640 (Page 29)

[OHH+05] ONCEL, N. ; HOUSELT, A. van ; HUIJBEN, J. ; HALLBÄCK, A.S. ; GURLU, O. ; ZANDVLIET, H.J.W. ; POELSEMA, B.: Quantum confinement between self-organized Pt nanowires on Ge (001). In: *Physical review letters* 95 (2005), Nr. 11, S. 116801 (Page 55)

[OKMS03] OŠŤÁDAL, I. ; KOCÁN, P. ; MYSLIVEČEK, J. ; SOBOTÍK, P.: Ag/Si(111)-(7x7) Heteroepitaxy - STM Experiment and KMC Simulations. In: *Czechoslovak Journal of Physics* 53 (2003), Nr. 1, S. 41–48. – ISSN 0011–4626 (Page 29)

[PBE96] PERDEW, J.P. ; BURKE, K. ; ERNZERHOF, M.: Generalized gradient approximation made simple. In: *Physical Review Letters* 77 (1996), Nr. 18, S. 3865–3868 (Page 33)

[PBGRS05] PAZ, Ó. ; BRIHUEGA, I. ; GÓMEZ-RODRÍGUEZ, J.M. ; SOLER, J.M.: Tip and surface determination from experiments and simulations of scanning tunneling microscopy and spectroscopy. In: *Physical review letters* 94 (2005), Nr. 5, S. 56103 (Page 20)

[Pei55] PEIERLS, R.E.: *Quantum theory of solids*. Oxford University Press, USA, 1955 (Page 36 and 52)

[PGSH00] PETERSEN, C.L. ; GREY, F. ; SHIRAKI, I. ; HASEGAWA, S.: Microfour-point probe for studying electronic transport through surface states. In: *Applied Physics Letters* 77 (2000), S. 3782 (Page 70 and 76)

[PHM+98] PARGA, AL V. ; HERNAN, OS ; MIRANDA, R. ; YEYATI, A. L. ; MINGO, N. ; MARTIN-RODERO, A. ; FLORES, F.: Electron resonances in sharp tips and their role in tunneling spectroscopy. In: *Physical Review Letters* 80 (1998), Nr. 2, S. 357–360 (Page 20)

[PLA+99] PARK, H. ; LIM, A.K.L. ; ALIVISATOS, A.P. ; PARK, J. ; MCEUEN, P.L.: Fabrication of metallic electrodes with nanometer separation by electromigration. In: *Applied Physics Letters* 75 (1999), S. 301 (Page 9)

[Pri73] PRIZE, Nobel: *The Nobel Prize in Chemistry 1973*. http://nobelprize.org/nobel_prizes/chemistry/laureates/1973. Version: 1973 (Page 30)

[QYM+07] QI, Y. ; YANG, W. ; MA, X. ; JI, S. ; FU, Y. ; ZHANG, Y. ; JIA, J.F. ; XUE, Q.K.: A study of the surface structure of deposited Au on Pb film. In: *Journal of Physics: Condensed Matter* 19 (2007), S. 136005 (Page 71)

[RAP+96] RUITENBEEK, JM V. ; ALVAREZ, A. ; PINEYRO, I. ; GRAHMANN, C. ; JOYEZ, P. ; DEVORET, MH ; ESTEVE, D. ; URBINA, C.: Adjustable nanofabricated atomic size contacts. In: *Review of scientific instruments* 67 (1996), Nr. 1, S. 108–111 (Page 9)

[RDV92] RAYNERD, G. ; DOUST, TN ; VENABLES, JA: Competing processes and controlling energies at the Ag/Si (111) interface. In: *Surface science* 261 (1992), Nr. 1-3, S. 251–266 (Page 27)

[RMS+05] REPP, J. ; MEYER, G. ; STOJKOVIĆ, S.M. ; GOURDON, A. ; JOACHIM, C.: Molecules on insulating films: Scanning-tunneling microscopy imaging of individual molecular orbitals. In: *Physical review letters* 94 (2005), Nr. 2, S. 26803 (Page 20)

[ROB+02] REICHERT, J. ; OCHS, R. ; BECKMANN, D. ; WEBER, HB ; MAYOR, M. ; LÖHNEYSEN, H.: Driving current through single organic molecules. In: *Physical Review Letters* 88 (2002), Nr. 17, S. 176804 (Page 9)

[RS50] READ, WT ; SHOCKLEY, W.: Dislocation models of crystal grain boundaries. In: *Physical Review* 78 (1950), Nr. 3, S. 275 (Page 32)

[RZM+97] REED, MA ; ZHOU, C. ; MULLER, CJ ; BURGIN, TP ; TOUR, JM: Conductance of a molecular junction. In: *Science* 278 (1997), Nr. 5336, S. 252 (Page 9)

[Sch39] SCHOTTKY, W.: Zur Halbleitertheorie der Sperrschicht-und Spitzengleichrichter. In: *Zeitschrift für Physik A Hadrons and Nuclei* 113 (1939), Nr. 5, S. 367–414 (Page 34)

[Sch42] SCHOTTKY, W.: Vereinfachte und erweiterte Theorie der Randschichtgleichrichter. In: *Zeitschrift für Physik A Hadrons and Nuclei* 118 (1942), Nr. 9, S. 539–592 (Page 34)

[Sch06] SCHMEIDEL, J.: *Elektromigrationsinduzierte Ag Nanokontakte für Molekulare Elektronik*, Leibniz Universität Hannover, Diplomarbeit, 2006 (Page 9 and 79)

[SNH99] SATO, N. ; NAGAO, T. ; HASEGAWA, S.: Si(111)-($\sqrt{3}x\sqrt{3}$)-Ag surface at low temperatures: symmetry breaking and surface twin boundaries. In: *Surf. Sci.* 442 (1999), Nr. 1, S. 65–73. http://dx.doi.org/10.1016/S0039-6028(99)00856-0. – DOI 10.1016/S0039–6028(99)00856–0 (Page 28 and 40)

[SNMB11] SUOMINEN, I. ; NIEMINEN, J. ; MARKIEWICZ, RS ; BANSIL, A.: Effect of orbital symmetry of the tip on Scanning Tunneling Spectra of $Bi_2Sr_2CaCu_2O_8+\delta$. In: *Arxiv preprint arXiv:1106.3302* (2011) (Page 20)

[Spi67]   SPIEGEL, K.: Untersuchungen zum schichtwachstum von silber auf der silizium (111)-oberfläche durch beugung langsamer elektronen. In: *Surface Science* 7 (1967), Nr. 2, S. 125–142 (Page 27)

[SPT09]   SCHMEIDEL, J. ; PFNÜR, H. ; TEGENKAMP, C.: Coulomb blockade effects in Ag/Si (111): The role of the wetting layer. In: *Physical Review B* 80 (2009), Nr. 11, S. 115304 (Page 25, 29, 65, 66, 67, 68, 71, 72, 74, 75, 97, 99, and 100)

[SPT11]   SCHMEIDEL, J. ; PFNÜR, H. ; TEGENKAMP, C.: Peierls-like phase transitions in domain walls. In: *Surface Science* (2011) (Page 41, 53, 54, and 98)

[SSM+06] SAKAMOTO, K. ; SUZUKI, T. ; MAWATARI, K. ; KOBAYASHI, K. ; OKABAYASHI, J. ; ONO, K. ; UENO, N. ; OSHIMA, M.: Phase transition of the Ag/ Si (111)-(sqrt [3]× sqrt [3]) surface studied by photoelectron diffraction. In: *Physical Review B* 73 (2006), Nr. 19, S. 193303 (Page 28)

[ST93]   SHIBATA, A. ; TAKAYANAGI, K.: Restructuring of the reconstructed Si (111) 7Ũ7 surface by metal (Au, Ag) deposition. In: *Japanese journal of applied physics* 32 (1993), Nr. 3B, S. 1385–1388 (Page 40)

[SUB+91] SCHEINFEIN, MR ; UNGURIS, J. ; BLUE, JL ; COAKLEY, KJ ; PIERCE, DT ; CELOTTA, RJ ; RYAN, PJ: Micromagnetics of domain walls at surfaces. In: *Physical Review B* 43 (1991), Nr. 4, S. 3395 (Page 39)

[Ter90]   TERSOFF, J.: Role of tip electronic structure in scanning tunneling microscope images. In: *Physical Review B* 41 (1990), Nr. 2, S. 1235 (Page 19)

[TH85]   TERSOFF, J. ; HAMANN, DR: Theory of the scanning tunneling microscope. In: *Physical Review B* 31 (1985), Nr. 2, S. 805 (Page 16 and 17)

[THI97]   TONG, X. ; HASEGAWA, S. ; INO, S.: Structures and electrical conductance of the Si (111)-$\sqrt{3} \times \sqrt{3}$-Ag surface with additional Ag adsorption at low temperatures. In: *Physical Review B* 55 (1997), Nr. 3, S. 1310 (Page 25)

[TN88]   TOSCH, St. ; NEDDERMEYER, H.: Initial Stage of Ag Condensation on Si(111)7x7. In: *Phys. Rev. Lett.* 61 (1988), Jul, Nr. 3, S. 349–352. http://dx.doi.org/10.1103/PhysRevLett.61.349. – DOI 10.1103/PhysRevLett.61.349 (Page 26)

[TN93] TAKAHASHI, T. ; NAKATANI, S.: Refinement of the-Ag structure by surface X-ray diffraction. In: *Surface Science* 282 (1993), Nr. 1-2, S. 17–32. – ISSN 0039–6028 (Page 48)

[TNO+88] TAKAHASHI, T. ; NAKATANI, S. ; OKAMOTO, N. ; ISHIKAWA, T. ; KIKUTA, S.: Study on the Si (111)$\sqrt{3}x\sqrt{3}$-Ag Surface Structure by X-Ray Diffraction. In: *Japanese Journal of Applied Physics* 27 (1988), S. L753–L755. – ISSN 0021–4922 (Page 25, 27, 48, and 60)

[TSN+03] TAJIRI, H. ; SUMITANI, K. ; NAKATANI, S. ; NOJIMA, A. ; TAKAHASHI, T. ; AKIMOTO, K. ; SUGIYAMA, H. ; ZHANG, X. ; KAWATA, H.: X-ray diffraction study of the Si (111)-sqrt [3]× sqrt [3]-Ag surface structure. In: *Physical Review B* 68 (2003), Nr. 3, S. 035330 (Page 28)

[TSP10] TEGENKAMP, C. ; SCHMEIDEL, J. ; PFNÜR, H.: Chemisorption of ferrocene on Si (111)-Ag Chemisorption of ferrocene on Si(111)–$\sqrt{3}x\sqrt{3}$: Frustrated conformational flexibility. In: *Surface Science* 605 (2010), S. 267–271 (Page 55, 57, and 59)

[TTTT85a] TAKAYANAGI, K. ; TANISHIRO, Y. ; TAKAHASHI, M. ; TAKAHASHI, S.: Structural analysis of Si (111)-7x7 by UHV-transmission electron diffraction and microscopy. In: *Journal of Vacuum Science & Technology A: Vacuum, Surfaces, and Films* 3 (1985), Nr. 3, S. 1502–1506 (Page 22 and 96)

[TTTT85b] TAKAYANAGI, K. ; TANISHIRO, Y. ; TAKAHASHI, S. ; TAKAHASHI, M.: Structure analysis of Si (111)-7x7 reconstructed surface by transmission electron diffraction. In: *Surface science* 164 (1985), Nr. 2-3, S. 367–392. – ISSN 0039–6028 (Page 22 and 96)

[TV87] TANG, CW ; VANSLYKE, SA: Organic electroluminescent diodes. In: *Applied Physics Letters* 51 (1987), Nr. 12, S. 913–915. – ISSN 0003–6951 (Page 5)

[UHN+85] UHRBERG, RIG ; HANSSON, GV ; NICHOLLS, JM ; PERSSON, PES ; FLODSTRÖM, SA: Photoemission study of the surface and bulk electronic structures of Si (111) 7×7 and Si (111) $\sqrt{3}\times\sqrt{3}$: Al. In: *Physical Review B* 31 (1985), Nr. 6, S. 3805 (Page 70)

[VAB+00] VLASOV, Y.A. ; ASTRATOV, VN ; BARYSHEV, AV ; KAPLYANSKII, AA ; KARIMOV, OZ ; LIMONOV, MF: Manifestation of intrinsic defects in optical properties

of self-organized opal photonic crystals. In: *Physical Review E* 61 (2000), Nr. 5, S. 5784 (Page 39)

[VDJ80] VENABLES, JA ; DERRIEN, J. ; JANSSEN, AP: Direct observation of the nucleation and growth modes of Ag/Si(111). In: *Surface Science* 95 (1980), Nr. 2-3, S. 411–430. – ISSN 0039–6028 (Page 29)

[Ven94] VENABLES, J.A.: Atomic processes in crystal growth. In: *Surface science* 299 (1994), S. 798–817 (Page 22 and 67)

[VGV+89] VLIEG, E. ; GON, A.W. Van D. ; VEEN, J.F. Van D. ; MACDONALD, JE ; NORRIS, C.: The structure of Si (111)-($\sqrt{3}x\sqrt{3}$)R30°-Ag determined by surface X-ray diffraction. In: *Surface Science* 209 (1989), Nr. 1-2, S. 100–114 (Page 27)

[WC87] WILSON, R.J. ; CHIANG, S.: Structure of the Ag/Si(111) surface by scanning tunneling microscopy. In: *Phys. Rev. Lett.* 58 (1987), Nr. 4, S. 369–372. `http://dx.doi.org/10.1103/PhysRevLett.58.369`. – DOI 10.1103/PhysRevLett.58.369 (Page 24 and 27)

[Wik11] WIKIPEDIA: *Transistor count — Wikipedia, The Free Encyclopedia*. `http://en.wikipedia.org/w/index.php?title=Transistor_count`. Version: 2011 (Page 3 and 96)

[WLN93] WAN, K. J. ; LIN, X. F. ; NOGAMI, J.: Surface reconstructions in the Ag/Si(111) system. In: *Phys. Rev. B* 47 (1993), May, Nr. 20, S. 13700–13712. `http://dx.doi.org/10.1103/PhysRevB.47.13700`. – DOI 10.1103/PhysRevB.47.13700 (Page 26, 27, 40, and 97)

[WR96] WEISS, PS ; REED, MA: Papers based on the Engineering Foundation Conference on Ordered Molecular and Nanoscale Electronics: Introduction. In: *Nanotechnology* 7 (1996), S. 345 (Page 9)

[WW10] WON, H. ; WILLIS, R.F.: A STM point-probe method for measuring sheet resistance of ultrathin metallic films on semiconducting silicon. In: *Surface Science* 604 (2010), Nr. 5-6, S. 491–495 (Page 70)

[You71] YOUNG, R.: Surface microtopography. In: *Physics Today* 24 (1971), S. 42 (Page 12)

[YTKT82] YASUSHI, T. ; TOHRU, Y. ; KENJIRO, O. ; TERUO, H.: A structure analysis of Ag-adsorbed Si (111) surface by LEED/CMTA. In: *Surface Science* 114 (1982), Nr. 1, S. 65–84 (Page 27)

[YWS72] YOUNG, R. ; WARD, J. ; SCIRE, F.: The topografiner: an instrument for measuring surface topography. In: *Rev. Sci. Instrum* 43 (1972), S. 999–1011 (Page 12)

[ZGJ06] ZHANG, HM ; GUSTAFSSON, JB ; JOHANSSON, LSO: Surface atomic structure of Ag/Si (111)-$\sqrt{3}x\sqrt{3}$. In: *Physical Review B* 74 (2006), Nr. 20, S. 201304 (Page 28)

[ZKDC88] ZEPPENFELD, P. ; KERN, K. ; DAVID, R. ; COMSA, G.: Diffraction from domain-wall systems. In: *Physical Review B* 38 (1988), Nr. 6, S. 3918 (Page 39)

List of Figures

Acknowledgements

I would like to thank my advisor Prof. Dr. H. Pfnür for giving me the possibility of doing this PhD research. His support, knowledge and experience were very helpful, starting from experimental basics and ending at complex theories and models. His readiness to help and to invest the time in discussion was very supporting.

Furthermore, I would like to thank PD Dr. C. Tegenkamp for being the direct partner for discussions and a rich source of ideas. His cooperation and hard work allowed the publications to appear in the highest quality. He introduced me to the vacuum technology and patiently and in details explained the complexities of experimental work. His help can be hardly overestimated.

The atmosphere in work, thank to all coworkers, was always happy and friendly. I'm grateful for their positive attitude, helpfulness and fruitful discussions. They allowed the work to be always uncomplicated even in stressing moments. The technical problems during this work were usually solved by the workshop, therefore I am very thankful for the high quality work and time spent on discussions, which allowed the experiment to run without delays.

I want to show my gratitude to my family. My parents always supported and helped me during my study, master work and PhD work. Without this help, this all would be hardly possible. Last but not least, I thank my wife, for support, patience and understanding.